



N° d'ordre NNT : 2017LYSEI112

THESE de DOCTORAT DE L'UNIVERSITE DE LYON
opérée au sein de
l'Institut National des Sciences Appliquées de Lyon

Ecole Doctorale N° ED162
MEGA

Spécialité/ discipline de doctorat :

Génie Mécanique

Soutenue publiquement le 28/11/2017, par :
Romain Bugnicourt

**Simulation of the contact between a
rough surface and a viscoelastic
material with friction.**

Devant le jury composé de :

Chateauminois, Antoine
Müser, Martin
Molinari, Jean-François
Gauthier, Catherine
Lubrecht, Ton
Sainsot, Philippe

Directeur de recherche
Professor Doktor
Professeur
Docteur
Professeur
Maître de conférences

ESPCI
Univ. des Saalandes
EPFL
Michelin
INSA Lyon
INSA Lyon

Président
Rapporteur
Rapporteur
Examinatrice
Directeur de thèse
Examineur

Département FEDORA – INSA Lyon - Ecoles Doctorales – Quinquennal 2016-2020

SIGLE	ECOLE DOCTORALE	NOM ET COORDONNEES DU RESPONSABLE
CHIMIE	<p>CHIMIE DE LYON http://www.edchimie-lyon.fr</p> <p>Sec : Renée EL MELHEM Bat Blaise Pascal 3^e étage secretariat@edchimie-lyon.fr Insa : R. GOURDON</p>	<p>M. Stéphane DANIELE Institut de Recherches sur la Catalyse et l'Environnement de Lyon IRCELYON-UMR 5256 Equipe CDFA 2 avenue Albert Einstein 69626 Villeurbanne cedex directeur@edchimie-lyon.fr</p>
E.E.A.	<p>ELECTRONIQUE, ELECTROTECHNIQUE, AUTOMATIQUE http://edeea.ec-lyon.fr</p> <p>Sec : M.C. HAVGOUDOUKIAN Ecole-Doctorale.eea@ec-lyon.fr</p>	<p>M. Gérard SCORLETTI Ecole Centrale de Lyon 36 avenue Guy de Collongue 69134 ECULLY Tél : 04.72.18 60.97 Fax : 04 78 43 37 17 Gerard.scorletti@ec-lyon.fr</p>
E2M2	<p>EVOLUTION, ECOSYSTEME, MICROBIOLOGIE, MODELISATION http://e2m2.universite-lyon.fr</p> <p>Sec : Sylvie ROBERJOT Bât Atrium - UCB Lyon 1 04.72.44.83.62 Insa : H. CHARLES secretariat.e2m2@univ-lyon1.fr</p>	<p>M. Fabrice CORDEY CNRS UMR 5276 Lab. de géologie de Lyon Université Claude Bernard Lyon 1 Bât Géode 2 rue Raphaël Dubois 69622 VILLEURBANNE Cédex Tél : 06.07.53.89.13 cordev@univ-lyon1.fr</p>
EDISS	<p>INTERDISCIPLINAIRE SCIENCES- SANTE http://www.ediss-lyon.fr</p> <p>Sec : Sylvie ROBERJOT Bât Atrium - UCB Lyon 1 04.72.44.83.62 Insa : M. LAGARDE secretariat.ediss@univ-lyon1.fr</p>	<p>Mme Emmanuelle CANET-SOULAS INSERM U1060, CarMeN lab, Univ. Lyon 1 Bâtiment IMBL 11 avenue Jean Capelle INSA de Lyon 696621 Villeurbanne Tél : 04.72.68.49.09 Fax : 04 72 68 49 16 Emmanuelle.canet@univ-lyon1.fr</p>
INFOMATHS	<p>INFORMATIQUE ET MATHEMATIQUES http://edinfomaths.universite-lyon.fr</p> <p>Sec : Renée EL MELHEM Bat Blaise Pascal, 3^e étage Tél : 04.72. 43. 80. 46 Fax : 04.72.43.16.87 infomaths@univ-lyon1.fr</p>	<p>M. Luca ZAMBONI Bâtiment Braconnier 43 Boulevard du 11 novembre 1918 69622 VILLEURBANNE Cedex Tél : 04 26 23 45 52 zamboni@maths.univ-lyon1.fr</p>
Matériaux	<p>MATERIAUX DE LYON http://ed34.universite-lyon.fr</p> <p>Sec : Marion COMBE Tél: 04-72-43-71-70 -Fax : 87.12 Bat. Direction ed.materiaux@insa-lyon.fr</p>	<p>M. Jean-Yves BUFFIERE INSA de Lyon MATEIS Bâtiment Saint Exupéry 7 avenue Jean Capelle 69621 VILLEURBANNE Cedex Tél : 04.72.43 71.70 Fax 04 72 43 85 28 Ed.materiaux@insa-lyon.fr</p>
MEGA	<p>MECANIQUE, ENERGETIQUE, GENIE CIVIL, ACOUSTIQUE http://edmega.universite-lyon.fr/</p> <p>Sec : Marion COMBE Tél: 04-72-43-71-70 -Fax : 87.12 Bat. Direction mega@insa-lyon.fr</p>	<p>M. Philippe BOISSE INSA de Lyon Laboratoire LAMCOS Bâtiment Jacquard 25 bis avenue Jean Capelle 69621 VILLEURBANNE Cedex Tél : 04.72 .43.71.70 Fax : 04 72 43 72 37 Philippe.boisse@insa-lyon.fr</p>
ScSo	<p>ScSo* http://ed483.univ-lyon2.fr/</p> <p>Sec : Viviane POLSINELLI Brigitte DUBOIS Insa : J.Y. TOUSSAINT Tél : 04 78 69 72 76 viviane.polsinelli@univ-lyon2.fr</p>	<p>M. Christian MONTES Université Lyon 2 86 rue Pasteur 69365 LYON Cedex 07 Christian.montes@univ-lyon2.fr</p>

*ScSo : Histoire, Géographie, Aménagement, Urbanisme, Archéologie, Science politique, Sociologie, Anthropologie

Remerciements

Résumé

Les pneus sont un organe déterminant dans la tenue de route des véhicules. Cette thèse porte sur la modélisation du contact entre la bande de roulement d'un pneumatique et une route sèche, afin de comprendre les différents phénomènes physiques mis en jeu ainsi que leurs rôles relatifs dans le frottement.

La rugosité multi échelle des sols routiers les rendent difficiles à modéliser avec une simulation par éléments finis standard. En utilisant l'hypothèse que la gomme de la bande de roulement est très grande devant la taille des rugosités, elle peut être considérée comme un massif semi-infini. Il est alors possible de résoudre efficacement le problème de contact en ne discrétisant que la surface du massif de gomme. Cette résolution est faite à l'aide d'un algorithme de Gradient Conjugué, au cours duquel les calculs matriciels sont effectués par Transformée de Fourier Rapide (FFT). La viscoélasticité de la gomme est prise en compte en régime transitoire. Les interactions à l'interface entre la gomme et le sol sont modélisés par une loi de frottement ainsi que par une énergie d'adhésion.

Les résultats montrent le rôle primordial de la viscoélasticité qui, couplée à la rugosité multi-échelle du sol, modifie la surface du contact au cours des différents étapes de mise en glissement d'un pneumatique, faisant ainsi varier le frottement.

MOTS CLÉS : Contact, Viscoélasticité, Elements de Frontière, Frottement, Adhésion

Abstract

Tires are a key component for the handling and safety of personal vehicles. In this thesis a model of the contact between the tire tread and a dry road is described. It aims at understanding the different physical phenomena taking place in such a contact and their relative role in tire friction.

Modeling the multiple scales of road roughness is difficult using a standard Finite Element Method. The hypothesis that the rubber of the tire tread is very large compared to the largest scale of surface roughness is made, so that it can be considered as a semi-infinite half-space. This way, the contact problem can be solved by discretizing the rubber surface only. The solver is a specific Conjugate Gradient iterative method, in which the matrix-vector products are performed with Fast Fourier Transforms. Transient viscoelasticity is accounted for with a step-by-step approach. The algorithm is able to model surface interactions such as Coulomb friction and adhesion.

Results show the crucial role played by viscoelasticity. Coupled with the road roughness, it changes the contact surface during the different steps of tire sliding, which in turns impacts friction.

KEYWORDS Contact, Viscoelasticity, Boundary Element method, Friction, Adhesion

Résumé étendu en langue française

Introduction

Les pneumatiques sont des composants essentiels des véhicules routiers. Le rôle d'un pneumatique est double : d'une part, il doit supporter la masse du véhicule, et d'autre part, il doit transmettre l'ensemble des efforts qu'un véhicule exerce sur la route (freinage, accélération, virages...). Ses performances jouent un rôle majeur dans la tenue de route d'un véhicule, mais aussi pour le confort des passagers et la consommation de carburant. Ce qui a amené les pneumatiques à devenir hautement technologiques est la nécessité d'obtenir un bon niveau de performance sous des conditions extrêmement diverses de températures et d'humidité, tout en restant abordables et d'une longue durée de vie.

Cette thèse porte sur la modélisation numérique des phénomènes physiques ayant lieu dans la zone de contact du pneu sur la route, aux échelles inférieures au millimètre. Lorsqu'un effort est appliqué au véhicule (un freinage par exemple), la gomme qui constitue la bande de roulement se déforme. Quand elle entre dans la zone de contact, elle s'enfonce d'abord dans les aspérités de la route, puis se cisaille sous l'effet du freinage. Lorsque les forces de cisaillement dépassent les forces de frottement, à l'arrière de la zone de contact, la gomme se met à glisser sur la route. Ces étapes sont illustrées en Figure 1.

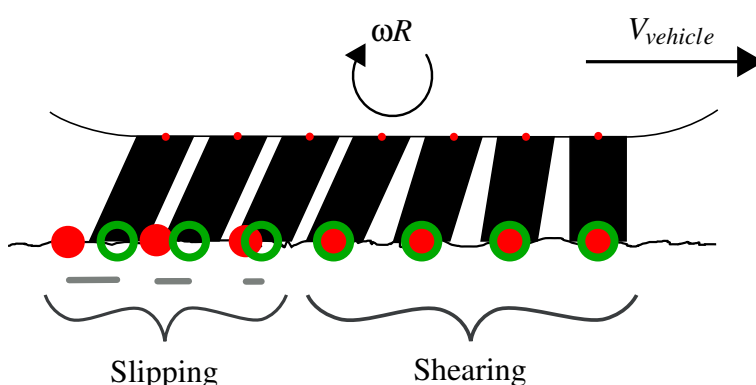


FIGURE 1 : Cinématique de la bande de roulement lors d'un freinage.

Lorsque la zone de glissement s'étend sur toute la zone de contact, le pneu se met à glisser de manière macroscopique, et il y a un risque fort de perte de contrôle, puisque le pneu perd alors son pouvoir directionnel. C'est pourquoi les manufacturiers pneumatiques

tendent de maximiser les forces de frottement et l'énergie dissipée lors du processus de cisaillement/glisement. L'expérience montre que des gomme plus tendres permettent en général d'augmenter les forces de frottement, mais cela se fait au détriment de la longévité et de la résistance au roulement. Pour trouver des compromis acceptables, les essais expérimentaux sont indispensables. Cependant, ceux-ci sont très coûteux, ce qui rend nécessaire l'utilisation de modèles analytiques et numériques. Ces derniers sont aussi un moyen de compréhension de la physique du problème.

Du contact de Hertz au sol routier

Le contact pneu/route est un problème de contact entre les aspérités d'un sol routier et le pain de gomme, très grand devant ces aspérités. L'idéalisation la plus simple de ce problème est le contact d'une sphère sur un massif élastique semi-infini, c'est-à-dire très grand dans toutes les directions par rapport à la taille de la zone de contact. Sous l'hypothèse que la zone de contact est également très petite devant la taille de la sphère, ce problème a été résolu analytiquement par Hertz en 1880, ce qui permet de déduire, entre autres, l'enfoncement en fonction de la force normale ou encore la forme du champ de pression dans la zone de contact, ainsi que la taille de cette zone de contact.

Pour modéliser un sol routier, une première idée est de considérer que chaque aspérité de la route se comporte comme un contact de Hertz. C'est l'approche initiée par Greenwood et Williamson [1]. En considérant que la route est une somme de sphère dont la hauteur suit une distribution donnée, il est possible de résoudre le problème de contact. Une modification majeure de ce modèle a été faite par Bush, Gibson and Thomas [2] pour considérer que le rayon des sphères suit lui aussi une distribution donnée, chacune des distributions pouvant être déduites de la mesure du sol considéré. Une critique majeure de ce type de modèles est son incapacité à prendre en compte les interactions des aspérités les unes avec les autres, ce qui rend les prédictions de ces modèles imprécises lorsque la surface de contact augmente et que ces interactions ne sont plus négligeables.

Pour pallier à ce défaut, un autre type d'approche a été initié par Persson [3][4]. Elle se base sur le fait que la route est une surface rugueuse à plusieurs échelles, depuis le nanomètre jusqu'au millimètre. Une mesure précise d'un sol routier permet d'en déduire sa Densité Spectrale de Puissance, qui représente l'amplitude des différentes échelles de rugosités. L'idée de cette approche est de considérer que la déformée de la gomme suit la même densité spectrale de puissance que le sol - ce qui n'est à priori valable que lorsque le contact est complet. Son modèle a été néanmoins validé dans de nombreux cas, même si certains paramètres (notamment la valeur de la plus petite longueur d'onde à prendre en compte) restent incertains pour une utilisation sur un cas réel.

L'origine du frottement

Connaître la surface de contact où l'enfoncement est important, mais n'explique pas en soit les frottement observés lorsque deux surfaces glissent l'une sur l'autre. Ces frottements sont pourtant un phénomène de notre vie de tous les jours. Léonard de Vinci les a

étudiés en utilisant un dispositif expérimental simple décrit et reproduit dans [5]. Selon ses observations, la force de frottement était proportionnelle à la force normale avec un coefficient de frottement $\mu = \text{Force tangentielle} / \text{Force normale} = 0.25$, ce quelque soit l'état des surfaces. En utilisant un dispositif similaire montré sur la Figure 2, Coulomb fit une campagne de test de grande échelle, utilisant plusieurs matériaux, plusieurs géométries et plusieurs états de surfaces. Ses conclusions sont que le coefficient μ est bien indépendant de la force normale, de la vitesse et de la surface de contact. Par contre, il dépend des matériaux et de l'état de surface. Ces conclusions sont la base de ce qui est connu aujourd'hui sous le nom de loi de frottement d'Amontons-Coulomb. Cette loi est encore utilisée dans de nombreuses applications car malgré sa simplicité, elle reste une bonne approximation de la réalité.

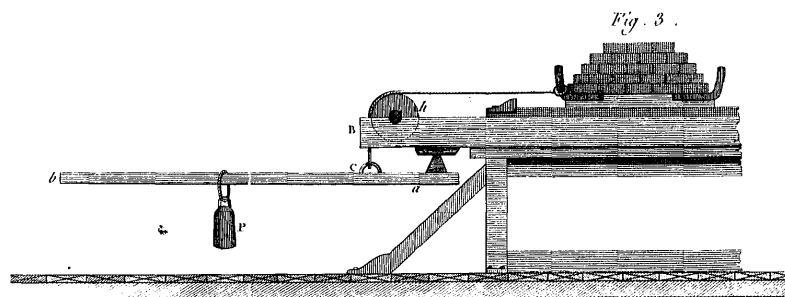


FIGURE 2 : Tribomètre de Coulomb. Gravure tirée de [6] disponible à la Bibliothèque Nationale de France.

Cependant, elle s'applique assez mal au cas du frottement pneu/route, puisque le frottement pneumatique est fortement dépendant de la vitesse de glissement et de la pression, ainsi que de la température. Il est important de comprendre et de prédire ces dépendances pour concevoir un pneumatique performant. Cela se révèle difficile en raison des nombreux phénomènes physiques qui ont lieu à différentes échelles et qui causent ce frottement.

Aux plus petites échelles (quelques nanomètres), les molécules constituant la gomme, qui sont de longues chaînes de polymères, interagissent avec la route par l'intermédiaire de liaisons faibles (forces de van der Waals). Ces forces ont pour effet d'attirer les deux surfaces l'une vers l'autre, ce qui va augmenter la surface de contact. Sur une surface complètement lisse, cela pourrait amener à un contact complet, car plus la surface de contact est grande, plus la résultante des forces d'adhésion est grande. Ce phénomène est en pratique limité par la rugosité. Il faut une certaine énergie élastique pour déformer la gomme, et pour qu'elle épouse complètement les rugosités du sol il en faudrait énormément : bien plus que l'énergie potentielle des forces adhésives. Les liaisons de van der Waals sont aussi, indirectement, la sources de forces de frottement : les chaînes de polymères forment des liaisons faibles avec le sol, mais lorsque celui-ci glisse, ces liaisons vont finir par se casser, pour se refaire un peu plus loin. Ce phénomène dissipe de l'énergie, ce qui explique une partie du frottement.

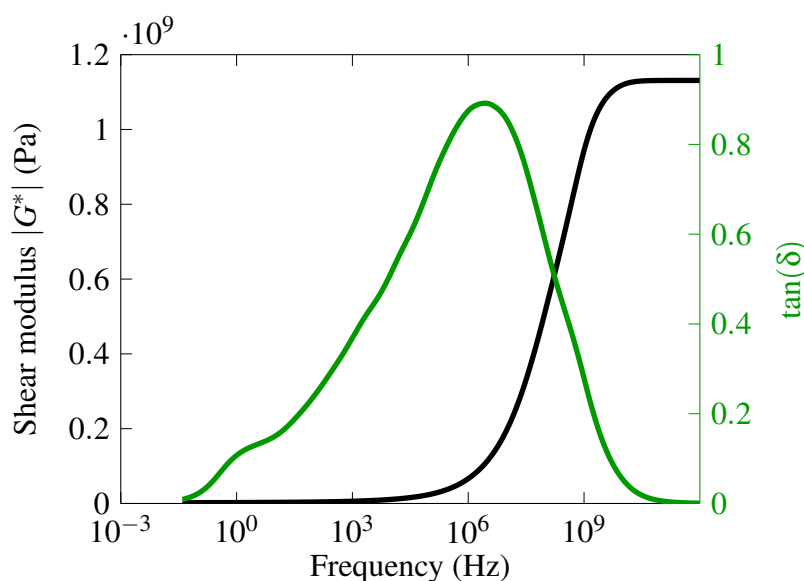


FIGURE 3 : Balayage fréquentiel de l'amplitude du module de cisaillement G^* et du module de perte $\tan(\delta)$ pour un matériau pneumatique.

Ce n'est pas la seule explication. Aux échelles plus grandes (de la centaine de nanomètres jusqu'au millimètre), la gomme peut être considérée comme un matériau continu et homogène. Elle possède la propriété d'être viscoélastique, ce qui signifie qu'elle dissipe de l'énergie lorsqu'elle se déforme. Un solide parfaitement élastique, lorsqu'un effort lui est imposé, se déforme immédiatement. Sa déformation varie pas dans le temps et il retrouve sa forme initiale une fois l'effort retiré. Un solide viscoélastique, lui, va se déformer assez peu initialement, mais sa déformation va augmenter avec le temps. Lorsque l'effort est retiré, il ne retrouve sa forme initiale qu'après un certain temps : dans ce cas de l'énergie a été perdue au cours du cycle de chargement/déchargement. Ces caractéristiques peuvent être illustrées par la réponse du matériau à une sollicitation périodique, ce qui permet de déterminer un module de cisaillement apparent en fonction de la fréquence ainsi qu'un module de perte $\tan(\delta)$, comme montré en Figure 3.

Lorsque la gomme glisse sur un sol rugueux, elle subit de nombreux cycles de chargement/déchargement lorsqu'elle se déforme pour épouser les aspérités de la route, et des déformations se font sur toutes les échelles de rugosité de la route. Elle dissipe donc de l'énergie, ce qui crée aussi du frottement. Ces deux phénomènes sont illustrés en Figure 4.

Modèles numériques du contact

La première difficulté à surmonter pour la modélisation numérique du frottement pneu/route est la diversité des phénomènes physiques à considérer.

A première vue, cette difficulté peut se surmonter grâce à l'utilisation de la méthode des Eléments Finis. C'est une méthode qui consiste à discrétiser l'espace en un grand

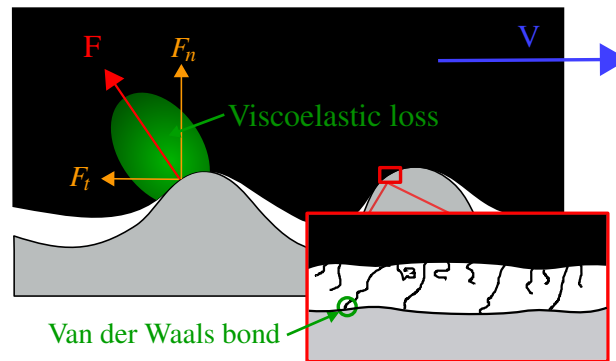


FIGURE 4 : Illustration des différents phénomènes physiques intervenant dans le frottement pneu/route.

nombre de mailles, ce qui permet la linéarisation puis la résolution des équations de la mécanique. Cette méthode est développée depuis des dizaines d'années, elle est fiable et utilisée régulièrement dans l'industrie. Certains logiciels commerciaux (tels que Abaqus ou COMSOL Multiphysic) permettent une mise en application simple de cette méthode en prenant en compte un grand nombre de phénomènes : viscoélasticité, thermique, dynamique, adhésion, contact, grandes déformations... Elle a été utilisée pour le contact par quelques auteurs pour ces raisons ([7, 8]) mais présente un défaut majeur pour la modélisation d'un contact rugueux. Cette méthode implique en effet de discrétiser tout le volume modélisé en 3 dimensions. Ce n'est pas problématique pour un contact lisse au vu des performances de calcul des ordinateurs actuels. Cependant, pour un contact rugueux sur plusieurs échelles un maillage très fin est nécessaire, plus fin que la plus petite rugosité prise en compte, ce qui impose un grand nombre de mailles et un temps de calcul rédhibitoire.

Utilisons plutôt l'hypothèse de massif semi-infini, ce qui suppose que les rugosités étudiées sont petites devant la taille de la bande de roulement. Dans ce cas, il existe une relation analytique entre les forces qui s'exercent à la surface et son déplacement (si on reste dans le cadre de l'élasticité en petites déformations). Pour discrétiser un tel problème, il faut alors uniquement discrétiser la surface du massif de gomme, c'est donc un maillage à 2 dimensions plutôt que 3. Le nombre de mailles est ainsi considérablement réduit ce qui permet des calculs rapides mêmes pour un pas très fin. Cette méthode est celle des éléments de frontière, dite aussi méthode semi-analytique, c'est la méthode choisie dans cette thèse. Elle s'est développée depuis les années 80, elle est décrite par exemple dans le livre de Kalker [9]. Ses performances ont grandement été améliorées, notamment par l'utilisation de transformées de Fourier rapides ([10, 11]) et d'algorithmes de résolution de contact adaptés ([12]).

De nombreuses études ont permis d'intégrer à cette méthode la viscoélasticité ([13, 14, 15, 16, 17, 18]) ainsi que les forces de frottement ([9, 19, 20, 21, 22]) et d'adhésion ([23]). La présente étude décrit un modèle d'éléments de frontière couplant viscoélasticité en régime transitoire, adhésion et frottement.

Description du modèle

Résolution d'un contact élastique

Le problème de contact a des conditions aux limites mixtes : dans la surface de contact S_c , la distance séparant la gomme et le sol doit être nulle : $U_z - H = 0$, où U_z est le déplacement de la gomme et H la hauteur du sol. En dehors de la surface de contact, la pression P doit être nulle. Finalement, soit la force normale totale, soit le déplacement normal moyen est imposé.

Grâce à l'hypothèse de massif semi infini, il existe une relation simple entre le champ de déplacement de la surface de la gomme et le champ de pression imposé sur cette surface (Equation 2.2) si le matériau est élastique :

$$U_z(X) = \frac{1-\nu}{2\pi G} \iint_{\Omega} \frac{P(X')}{\|X - X'\|} dX' \quad (1)$$

G est le module de cisaillement du matériau, ν son coefficient de Poisson. Discrétisons maintenant la surface avec un maillage régulier. On peut, au choix, choisir que le champ de pression est périodique, ou que la pression est nulle en dehors du domaine discrétisé. Le calcul des déplacements en fonction de la pression s'écrit alors :

$$U_z = \frac{1-\nu}{2\pi G} A_{zz} \cdot P \quad (2)$$

A_{zz} est une matrice qui dépend du maillage et des conditions aux limites (périodiques ou non-périodiques) choisies. Dans les deux cas, c'est une matrice de convolution, ce qui permet au produit matriciel $A_{zz} \cdot P$ d'être effectué efficacement dans le domaine de Fourier via une transformée de Fourier rapide (FFT).

Calculer les déplacements depuis le champ de pression ne suffit pas. Il faut désormais résoudre le problème de contact, c'est à dire déterminer le champ de pression et la surface de contact qui satisfont les conditions aux limites citées plus haut. Cette résolution est faite par un algorithme de gradient conjugué similaire à ceux présentés dans [12, 24]. Il s'agit d'un algorithme itératif qui, partant d'un champ de pression initial, donne avec les itérations des champs de pression qui minimisent de plus en plus l'erreur commise sur la distance entre les surfaces. Lorsque l'erreur est jugée assez faible, la boucle s'arrête et le problème est résolu.

Adhésion

L'algorithme est adapté pour pouvoir prendre en compte des forces d'adhésions. Ces forces sont des forces d'attraction qui dépendent de la distance entre les deux surfaces. Le potentiel utilisé ici est exponentiel, la force d'adhésion est déterminée pour chaque point (i, j) par l'Equation 3

$$P_{adh}(i, j) = -\frac{\gamma_0}{z_0} \exp\left(-\frac{U_z(i, j) - H(i, j)}{z_0}\right) \quad (3)$$

γ_0 est l'énergie d'adhésion par unité de surface, z_0 est la portée de ces forces. Plus l'énergie est grande, plus l'effet des forces d'adhésion sera grande. La portée des forces d'adhésion modifie, localement, la forme du champ de pression. Pour un contact de Hertz, l'adhésion provoque des pics de pression négative sur les bords du contact. Avec des forces de courte portée, ces pics sont de grande amplitude et étroit, alors que des forces de plus longue portée provoquent des pics de moindre amplitude mais plus larges.

La formulation du problème de contact est légèrement modifiée. Dans la surface du contact il doit toujours y avoir une distance nulle entre les surfaces, et en dehors de celle-ci la pression est imposée en fonction de la distance par le potentiel d'adhésion. L'algorithme de gradient conjugué présenté pour le contact élastique doit donc être adapté car l'adhésion ajoute une non-linéarité. La façon la plus simple d'adapter l'algorithme est, à chaque itération, d'ajouter manuellement un champ d'adhésion calculé selon les déplacements du pas précédent. Cette solution est rapide à mettre en uvre et fonctionne efficacement lorsque les forces d'adhésion sont faibles et ne sont pas de trop courte portée. Elle ne converge pas si ce n'est pas le cas, ce qui est problématique.

Un autre type d'approche est de résoudre le problème dual. Il s'agit de trouver le champ de déplacement qui satisfait les conditions aux limites du contact, et qui induit un champ de pression qui respecte le potentiel d'adhésion. L'algorithme correspondant permet de plus facilement prendre en compte les forces d'adhésion et est beaucoup plus stable, même pour des forces d'adhésion de courte portée.

Viscoélasticité

Une formulation différentielle de la viscoélasticité est utilisée (voir [25]). Elle permet de prendre en compte la viscoélasticité en régime transitoire. La gomme est modélisée comme un solide de Zener, illustré en Figure 5.

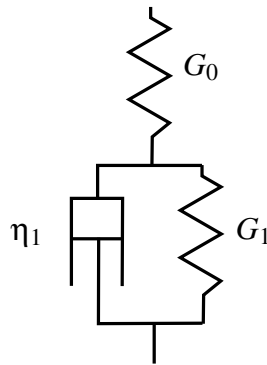


FIGURE 5 : Représentation d'un solide de Zener. G_0 et G_1 sont les rigidités des deux ressorts et η_1 la viscosité de l'amortisseur.

Cette illustration simplifiée permet de comprendre l'équation différentielle qui relie les efforts aux déplacements pour un tel solide, donnée par l'Equation 4 pour un matériau incompressible.

$$\left(1 + \frac{G_1}{G_0}\right)s + \frac{\eta_1}{G_0}\dot{s} = 2G_1e + 2\eta_1\dot{e} \quad (4)$$

Ici G_0 et G_1 sont des modules de cisaillement, η_1 un coefficient d'amortissement, s la partie déviatorique du tenseur de contraintes et e la partie déviatorique du tenseur de déformations. En utilisant la méthode d'équations fonctionnelles de Radok [26], on peut transposer cette équation en une équation différentielle sur la pression et les déplacements de la surface. En utilisant la même discrétisation de l'espace que pour le problème élastique, on obtient l'équation différentielle 5.

$$A_{zz}.P \left(1 + \frac{G_1}{G_0}\right) + \frac{\eta_1}{G_0}A_{zz}.\dot{P} = G_1U + \eta_1\dot{U} \quad (5)$$

Pour résoudre cette équation différentielle, le temps est discrétisé, et l'équation 5 est linéarisée entre chaque pas de temps. L'algorithme de contact élastique peut alors être directement utilisé pour résoudre le problème viscoélastique. Pour chaque maille, une variable interne est nécessaire. Elle rend compte du déplacement résiduel du point en question causé par la viscoélasticité. Pour avoir une précision correcte, la taille des pas de temps doit être faible par rapport au temps caractéristique du matériau.

La Figure 6 montre l'évolution d'un contact sphère/plan viscoélastique avec une force normale constante calculée avec le modèle numérique : la surface de contact augmente alors que la sphère s'enfonce dans la gomme. La viscoélasticité provoque aussi de légers pics de pression sur les bords du contact pendant le régime transitoire, qui disparaissent pour les temps longs ou les temps très courts.

Forces de frottement et effet de pente

L'algorithme présenté jusqu'ici ne prend en compte que la direction normale. Il permet de calculer une partie des pertes viscoélastiques lors du glissement de la gomme sur une surface rugueuse, mais ne prend pas en compte les forces de frottement à l'interface. L'avantage de l'hypothèse de massif semi-infini et de matériau incompressible est que les deux directions sont indépendantes : les déplacements normaux n'engendrent aucun déplacements tangentiels et vice-versa, ce qui pourrait laisser penser que modéliser le frottement n'est pas indispensable pour quantifier les pertes viscoélastiques.

Si cela est vrai en régime établi, ça l'est beaucoup moins en régime transitoire. En effet, le frottement va modifier considérablement la cinématique de glissement. Pour un contact sphère/plan par exemple, les bords du contact commencent à glisser alors que le centre reste collé. Le glissement se propage au fur et à mesure jusqu'à atteindre le centre. La gomme est alors en glissement total. Cette cinématique particulière de mise en glissement peut modifier grandement les pertes viscoélastiques pendant le régime transitoire. La viscoélasticité cause donc un couplage indirect entre les deux directions.

Prendre en compte ce couplage directement, dans la même boucle de gradient conjugué est relativement compliqué. C'est pourquoi une approche pas à pas est utilisée, comme pour la viscoélasticité. Pour que l'algorithme reste précis, il faut que le glissement lors

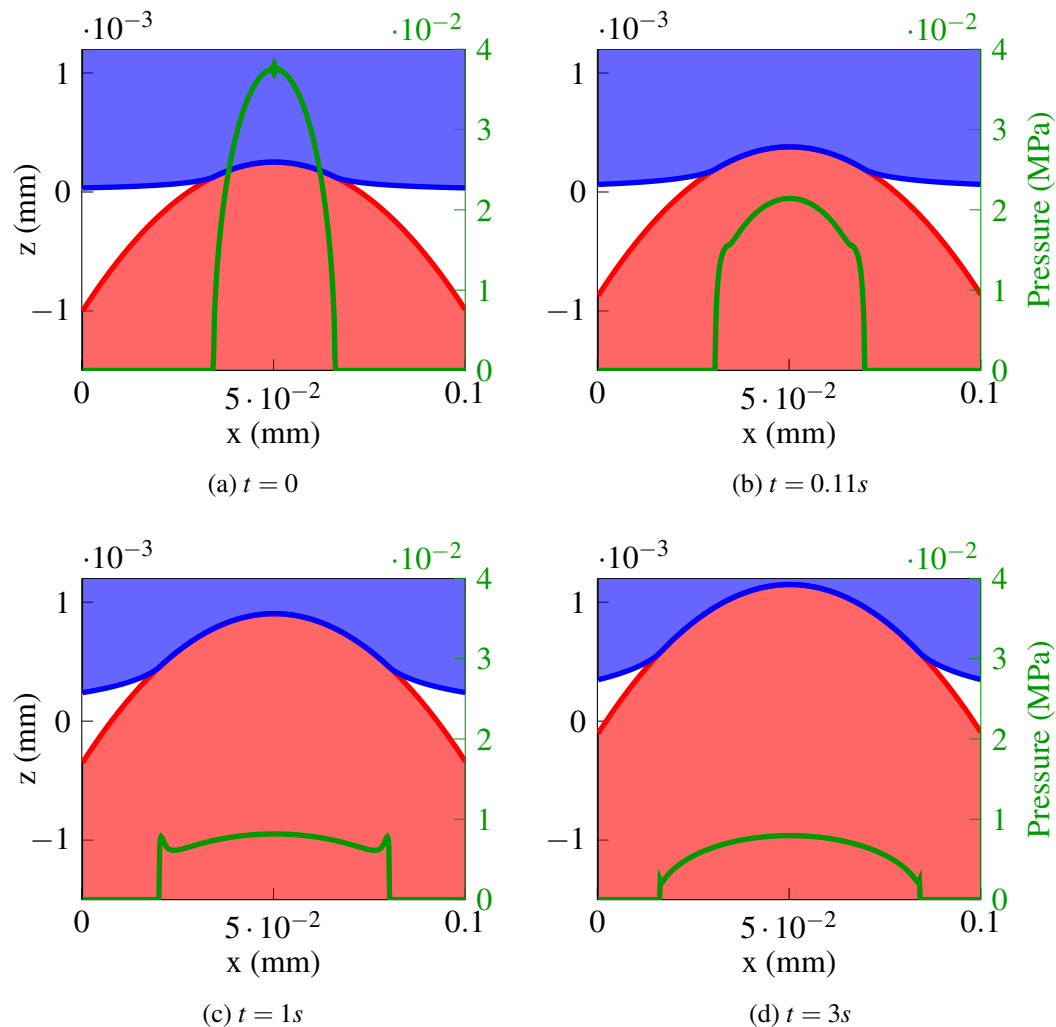


FIGURE 6 : Profils de pression et de déplacement pour un contact sphère/plan viscoélastique à différents instants.

d'un pas de temps soit petit comparé à la taille caractéristique du problème. L'algorithme normal/tangential peut se schématiser de la façon suivante :

Initialisation

- Calcul des pressions et des déplacements normaux

Début de la boucle temporelle

- Calcul des déplacements tangentiels
- Interpolation de la gomme selon les glissement locaux
- Calcul des pressions et déplacements normaux

Fin de la boucle

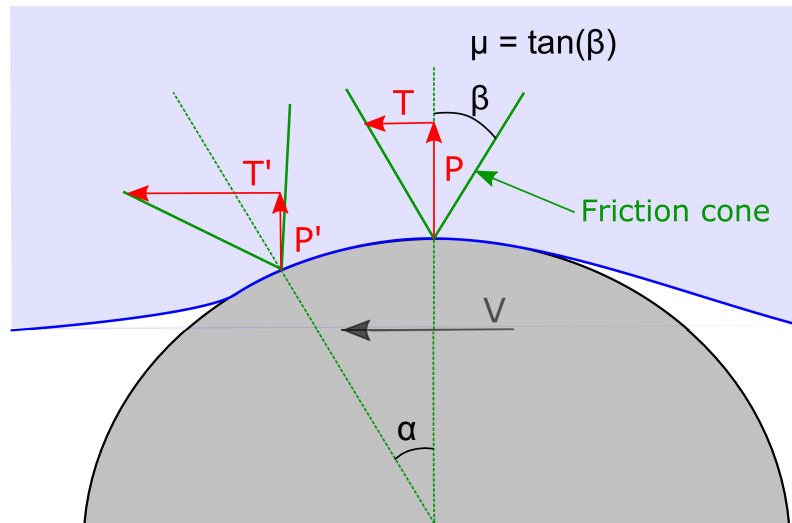


FIGURE 7 : Illustration de l'effet de la pente locale dans un contact sphère/plan. La sphère glisse vers la gauche dans un matériau viscoélastique. Le cône de frottement est penché à l'avant du contact, ce qui augmente le frottement local par rapport à l'arrière du contact.

A chaque pas de temps, un incrément de déplacement uniforme est appliqué à la surface routière, qui est considérée comme rigide. A partir de ce déplacement, la réponse de la gomme est calculée en fonction du frottement. La surface de contact peut se diviser en deux. Dans la surface collée S_{stick} , le déplacement tangentiel (U_x, U_y) de la gomme doit être le même que celui de la route, et la norme des efforts tangentiels $\|(T_x, T_y)\|$ doit être inférieure à une certaine valeur T_{max} qui dépend de la loi de frottement. Pour une loi de Coulomb avec un coefficient de frottement μ , $T_{max} = \mu P$. Dans la surface glissante S_{slip} , la norme des efforts tangentiels $\|(T_x, T_y)\|$ est égale T_{max} et la direction des efforts doit être la même que la direction du glissement local.

Pour modéliser précisément les forces de frottement, il faut prendre en compte, en chaque point, la pente locale de la surface rugueuse. En effet, en projetant la loi de Coulomb dans le repère local de la surface, et en laissant les efforts tangentiels dans le repère globale, T_{max} dépend alors de la direction de glissement, ce qui va augmenter le frottement local à l'avant du contact et le réduire à l'arrière, comme illustré en Figure 7. Si le contact est symétrique, l'impact de la pente sur la force totale de frottement est négligeable puisque les deux phénomènes se compensent. Mais la viscoélasticité rend le contact dissymétrique, le barycentre de la zone de contact est située à l'avant de la sphère pour un contact/sphère plan. Cela augmente donc le frottement total.

Un algorithme de gradient conjugué permet de résoudre itérativement le problème de frottement. Chaque itération de la boucle donne un nouveau champ de contrainte tangentiel (T_x, T_y) . Si, en un point, la norme de la contrainte dépasse la limite T_{max} , elle est rectifiée afin de respecter cette limite. En d'autres termes, le champ de contrainte est à chaque itération projeté dans le champ des contraintes admissibles. L'algorithme est adapté pour prendre en compte cette modification, et permet, au fur et à mesure des itérations, de

résoudre le problème de plus en plus précisément.

La viscoélasticité est implémentée avec une procédure pas à pas similaire à celle utilisée pour la direction normale.

Une fois les déplacements tangentiels calculés, il reste l'étape d'interpolation dans la surface glissante puisque la position relative des deux surfaces y a changé. La première façon de faire est Eulérienne, il s'agit d'interpoler la gomme par rapport à la surface rigide en fonction des glissements locaux. En petite déformation et en élasticité cela ne paraît pas nécessaire puisque le matériau est homogène, mais la viscoélasticité rend cette étape incontournable. En effet les variables internes viscoélastiques (les déplacements résiduels) dépendent de la position. L'approche Eulérienne fonctionne, mais a un coût de calcul non négligeable, puisqu'il y a au moins trois variables internes par point (une par direction). L'approche Lagrangienne consiste à laisser la gomme non déformée et à interpoler le sol par rapport à elle. Cela peut paraître contre-intuitif puisque le sol est considéré comme rigide, mais dans le cadre des petites déformations cela n'a théoriquement pas d'impact. C'est aussi une façon de faire plus rapide, puisque le sol n'a par définition qu'une seule variable par maille. Il faut toutefois garder en mémoire le sol original non interpolé, car des interpolations successives risqueraient de le lisser.

Résultats sur un sol rugueux

Le modèle a été utilisé pour répondre au *Contact Mechanics Challenge* initié par M. Müser. Le but de ce challenge était de modéliser un contact rugueux multi-échelles avec des forces d'adhésion de courte portée, pour un matériau élastique. Une solution de référence avait été calculée avec un modèle numérique sur un super-cluster mais les résultats n'avaient pas été divulgués. Notre contribution au challenge a nécessité un calcul sur une grille de 32768×32768 mailles et s'est avérée être en total accord avec le résultat de référence. Les résultats du challenge ont été publiés [27].

Une étude comparative avec le modèle analytique de Persson [28] a été menée, pour un contact entre un matériau viscoélastique et une surface rugueuse (sans frottement à l'interface ni adhésion). La surface est représentée en Figure 8. La cinématique est la suivante : d'abord la gomme glisse à une vitesse faible V_0 constante jusqu'à $t = 0$, où la vitesse d'entraînement est augmentée brutalement jusque V_1 . Les courbes de frottement apparent μ du modèle numérique et du modèles analytique de Persson sont présentés en Figure 9. Le frottement apparent μ est calculé comme la force tangentielle totale (causée par les pertes viscoélastiques) divisée par la force normale. Cette courbe montre que la force tangentielle passe par un maximum juste après le saut de vitesse pour ensuite atteindre un nouveau régime stationnaire. Comme la vitesse augmente, la fréquence de sollicitation augmente et le matériau paraît plus dur du fait de sa viscoélasticité (voir Figure 3), c'est pour cela que l'aire de contact diminue.

Pour comprendre l'origine du maximum dans la courbe de frottement, il est utile de tracer le travail des forces normales et tangentielles et les pertes viscoélastique entre chaque pas de temps (Figure 10). Cette figure montre que le maximum est causé en

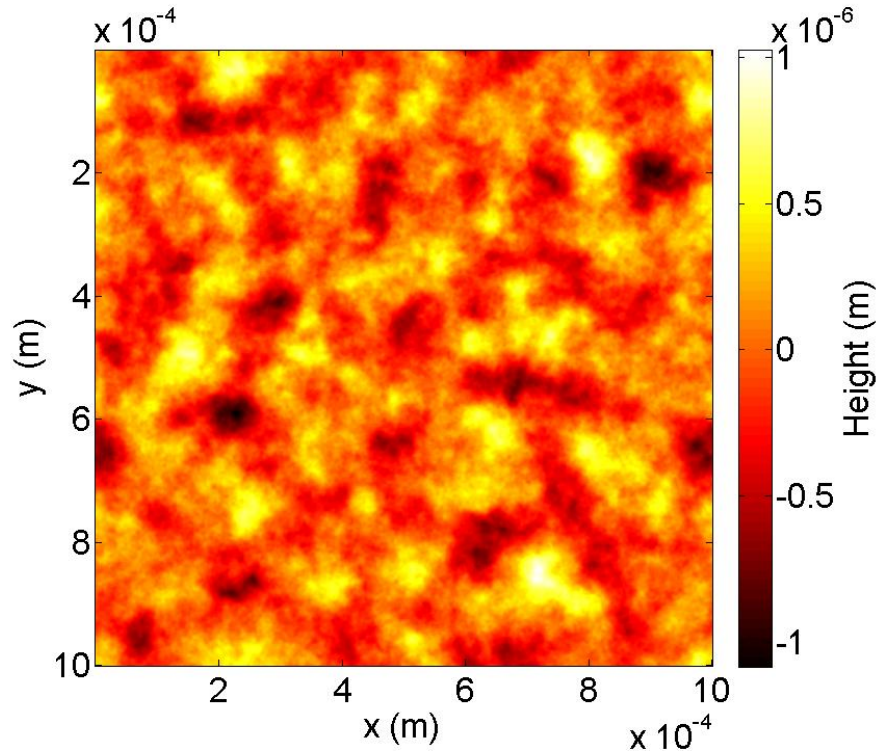


FIGURE 8 : Représentation de la surface rugueuse utilisée pour la comparaison avec le modèle de Persson.

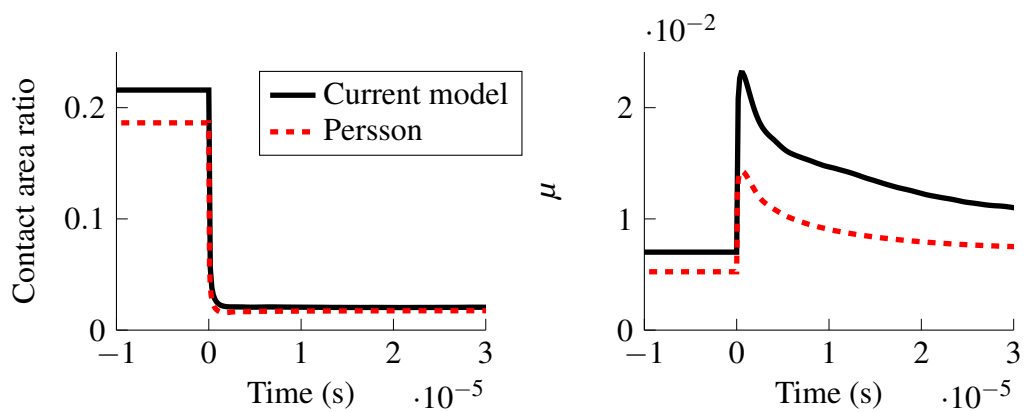


FIGURE 9 : Aire de contact et frottement apparent en fonction du temps pour le modèle numérique et le modèle de Persson. $V_0 = 0.01 \text{ m s}^{-1}$, $V_1 = 3 \text{ m s}^{-1}$

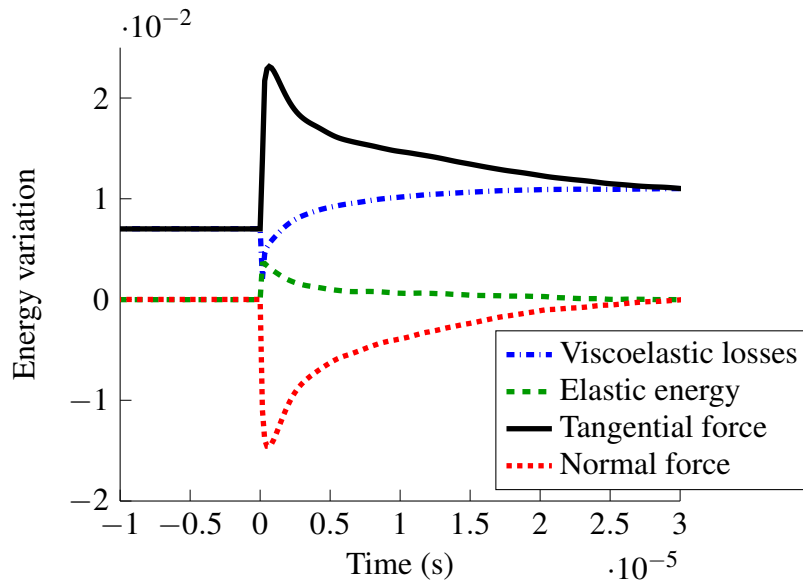


FIGURE 10 : Travail des forces et pertes adimensionnés pendant un saut de vitesse. $V_0 = 0.01 \text{ ms}^{-1}$, $V_1 = 3 \text{ ms}^{-1}$

majeure partie par une augmentation de l'énergie potentielle de la force normale : lorsque la vitesse augmente, le matériau devient en apparence plus dur et se soulève au dessus des aspérités, ce qui augmente l'énergie potentielle de la force normale. Cette énergie provient nécessairement de la force tangentielle qui doit augmenter en conséquence.

Une série d'essais a été effectuée couplant viscoélasticité et frottement. Le sol utilisé est un sol idéalisé : c'est un sol ayant seulement deux longueurs d'onde. Il est assez représentatif d'un sol rugueux et permet de bien comprendre les rôles respectifs de chaque longueur d'onde. Le cinématique utilisée ici est différente : d'abord, la force normale est appliquée pendant un temps LT (à vitesse nulle), ensuite une vitesse d'entraînement constante est appliquée, en gardant la force normale constante.

La Figure 11 montre l'évolution de l'aire de contact et de frottement apparent avec le temps. Pendant la première milliseconde, l'aire de contact augmente régulièrement. Après cette première milliseconde de chargement, la vitesse est appliquée, et le frottement augmente régulièrement car le pain de gomme se cisaille. La surface de contact diminue, le frottement par un maximum, puis continu d'osciller en raison de la périodicité du sol. Ces oscillations ont deux longueurs d'ondes, qui correspondent aux deux longueurs d'ondes du sol. Ce sont les grandes longueurs d'ondes du sol, qui ont aussi une plus grande amplitude, qui provoquent un maximum marqué et large dans la courbe de frottement alors que les petites longueurs d'ondes provoquent des oscillations marquées mais très fines. Le frottement apparent est causé d'une part par le frottement Coulombien à l'interface et d'autre part par les pertes viscoélastiques. Le maximum et les oscillations ne sont pas très marqués, ce qui indique que dans le cas présent les pertes viscoélastiques sont faible devant le frottement Coulombien (qui est constant une fois que l'intégralité de la surface est en glissement, voir la courbe verte).

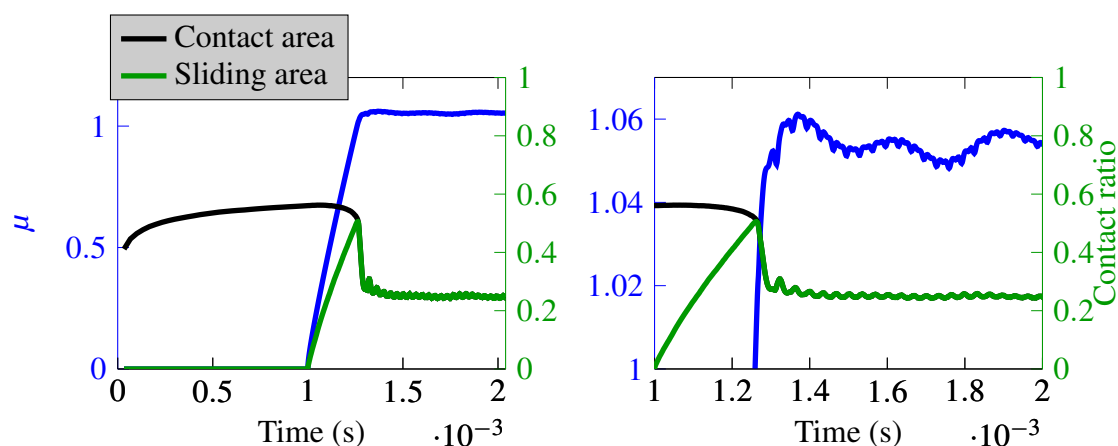


FIGURE 11 : Evolution du frottement apparent et de l'aire de contact. La figure de droite est un zoom sur la zone d'intérêt.

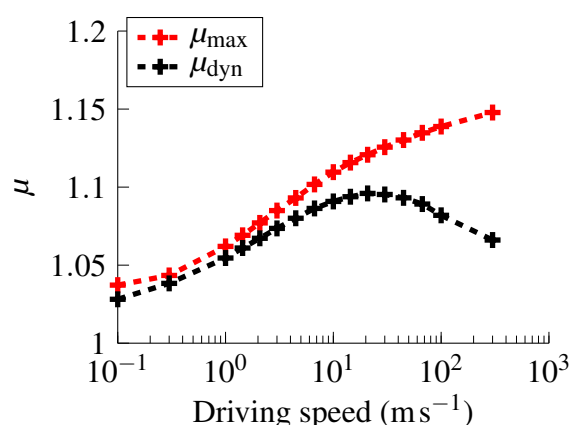


FIGURE 12 : Evolution du frottement avec la vitesse de glissement.

De ces courbes il est possible d'extraire un maximum μ_{\max} et une valeur de régime pseudo-permanent μ_{dyn} , calculé en moyennant le courbe de frottement après le passage du maximum. La Figure 12 montre l'évolution de ces deux valeurs avec la vitesse d'entraînement. Le frottement en régime permanent a une forme de cloche, il augmente d'abord avec la vitesse avant décroître. Ce phénomène est dû à la viscoélasticité, puisque le module de perte a lui aussi une forme de cloche avec la fréquence. A basse vitesse (ou basse fréquence) la gomme se comporte comme un matériau mou, à haute vitesse comme un matériau dur, mais la dissipation viscoélastique n'est présente que pour des fréquences intermédiaires, et donc des vitesses intermédiaires. Le maximum de frottement μ_{\max} est lui une fonction toujours croissante de la vitesse, car il dépend surtout de la variation de rigidité apparente du matériau, qui est toujours croissante avec la fréquence. En effet, le maximum de frottement est ici aussi causé par la montée du pain de gomme causée par la rigidification du matériau lors de la mise en glissement.

Conclusions

Les résultats montrent que le frottement dépend énormément des fréquences excitées lors du chargement et du glissement. La route étant rugueuse sur une large plage de longueurs d'ondes, un large spectre de fréquence est excité lors du glissement, d'où des pertes viscoélastiques qui causent une part non-négligeable du frottement total. Dans de nombreux cas, il apparaît un maximum dans la courbe de frottement. Ce maximum s'explique par la rigidification apparente du matériau lors du glissement, et est causé surtout par les rugosités de grande amplitude. Le modèle permet aussi de caractériser l'influence de l'adhésion dans un contact rugueux. Il apparaît qu'elles ont un effet non négligeable sur le frottement pour un contact lisse, mais que les rugosités diminuent grandement son influence.

Pour arriver à ses résultats, un algorithme de contact performant a été développé. Il est détaillé dans ce manuscrit. C'est un algorithme de type éléments de frontière qui utilise des transformées de Fourier rapides pour le calcul des produits matriciels. Des boucles de gradient conjugué sont utilisées pour la résolution du contact et du frottement. Elles font l'objet d'une optimisation originale et performante. Le modèle permet, via une discrétisation fine du temps, de prendre en compte à la fois la viscoélasticité, le frottement et les forces d'adhésion.

Contents

Résumé étendu en langue française	ix
Contents	xxv
List of Figures	xxvii
List of Tables	xxxii
1 Introduction and bibliography	3
1.1 General introduction	4
1.1.1 The crucial role of tires	4
1.1.2 Friction forces and their origin	6
1.1.3 Viscoelasticity and surface roughness	7
1.2 Bibliography: experimental and theoretical results for a contact at the meso-scale	9
1.2.1 Hertzian contact	9
1.2.2 Adhesion	10
1.2.3 Viscoelasticity	12
1.2.4 Surface roughness	13
1.2.5 Numerical methods	16
2 Numerical model for frictionless contacts and application to Hertzian contacts	21
2.1 Numerical model for normal contacts	22
2.1.1 Discretization and FFT-convolution	22
2.1.2 Conjugate Gradient algorithm for normal contact without adhesion	23
2.1.3 Viscoelasticity	25
2.2 Application: viscoelastic Hertzian contact	27
2.2.1 Convergence analysis	27
2.2.2 Viscoelastic losses in a sliding contact	30
2.3 Adhesion	34
2.3.1 Adhesion model	34
2.3.2 Implementation	36
2.3.3 Validation: viscoelastic Hertzian contact with adhesion	38

3	Contacts with friction	41
3.1	Friction laws	42
3.1.1	Friction forces in a contact problem	42
3.1.2	Coulomb friction and “constant shear stress” friction	43
3.1.3	Effect of the local slope	44
3.2	BEM with friction	46
3.2.1	Tangential problem functional	46
3.2.2	Enforcement of the friction law	47
3.2.3	Conjugate Gradient algorithm	48
3.2.4	Conjugate gradient with perpendicular residual	50
3.3	Validation and performance	51
3.4	Viscoelasticity	52
3.5	Interpolation	53
3.5.1	Comparison with Finite Element simulation	55
3.6	Inertia	56
3.6.1	Numerical instability	56
3.6.2	Implementation	59
4	Rough contact	63
4.1	Numerical generation of rough surfaces	64
4.2	The “Contact Mechanics Challenge”	64
4.3	Transient viscoelastic contact without friction	65
4.4	Computation of the potential energy and loss	67
4.5	Role of the different scales in a frictional contact	70
4.5.1	Effect of adhesion on rubber sliding	78
	Conclusion	83
A	Influence Coefficient matrices in the Fourier space	85
B	Conjugate Gradient modifications to account for the effect of the local slope.	89
	Bibliography	95

List of Figures

1	Cinématique de la bande de roulement lors d'un freinage.	ix
2	Tribomètre de Coulomb. Gravure tirée de [6] disponible à la Bibliothèque Nationale de France.	xi
3	Balayage fréquentiel de l'amplitude du module de cisaillement G^* et du module de perte $\tan(\delta)$ pour un matériau pneumatique.	xii
4	Illustration des différents phénomènes physiques intervenant dans le frottement pneu/route.	xiii
5	Représentation d'un solide de Zener. G_0 et G_1 sont les rigidité des deux ressorts et η_1 la viscosité de l'amortisseur.	xv
6	Profils de pression et de déplacement pour un contact sphère/plan viscoélastique à différents instants.	xvii
7	Illustration de l'effet de la pente locale dans un contact sphère/plan. La sphère glisse vers la gauche dans un matériau viscoélastique. Le cône de frottement est penché à l'avant du contact, ce qui augmente le frottement local par rapport à l'arrière du contact.	xviii
8	Representation de la surface rugueuse utilisée pour la comparaison avec le modèle de Persson.	xx
9	Aire de contact et frottement apparent en fonction du temps pour le modèle numérique et le modèle de Persson. $V_0 = 0.01 \text{ ms}^{-1}$, $V_1 = 3 \text{ ms}^{-1}$	xx
10	Travail des forces et pertes adimensionnés pendant un saut de vitesse. $V_0 = 0.01 \text{ ms}^{-1}$, $V_1 = 3 \text{ ms}^{-1}$	xxi
11	Evolution du frottement apparent et de l'aire de contact. La figure de droite est un zoom sur la zone d'intérêt.	xxii
12	Evolution du frottement avec la vitesse de glissement.	xxii
1.1	Valentino Rossi during the 2017 Argentina MotoGP race. MotoGP riders reach lean angles as high as 60° . Photo: MICHELIN	5
1.2	Kinematics of the rubber tread during braking.	5
1.3	Coulomb's tribometer, picture from [6] made available by the Bibliothèque Nationale de France.	6
1.4	Illustration of the physical phenomena causing energy losses during sliding.	7
1.5	Shear modulus amplitude and $\tan(\delta)$ of a typical tire material	8
1.6	Close-up photography of a road pavement. Photo by Angel Caboodle under the license CC BY-SA 3.0	9

1.7	Evolution of the contact radius with the Tabor coefficient for a Hertzian contact with adhesion. The ‘Hertz’ solution is the contact radius without adhesion. The radius of the sphere is 1 m, the normal force is 0.00001 N, the adhesive energy is $3.2 \times 10^{-5} \text{ J m}^{-2}$ and the material is incompressible and elastic with a shear modulus of 0.37 Pa.	11
1.8	Representation of the Standard Linear Solid. G_0 and G_1 are the stiffness of the two springs, η_1 is the viscosity of the dashpot.	13
1.9	Typical PSD of a road surface.	15
1.10	Evolution of the friction coefficient with the sliding speed according to Persson’s model.	16
1.11	Top view of the numerically computed contact area between a rough surface and an elastic half-space with short range adhesion, as described in [29]. The magnified contact spot shows the very fine resolution of the mesh.	18
2.1	Generalized Zener model	26
2.2	Evolution of the contact radius with time for a viscoelastic Hertzian contact with constant normal load. Analytical solution from Lee and Radok [30].	28
2.3	Pressure and displacement profiles for a viscoelastic hertzian contact at different times.	29
2.4	Temporal evolution of the error in contact radius prediction for different time increments.	30
2.5	Mean error in contact radius. The ‘mesh convergence’ curve is the error as a function of the dimensionless mesh cell length for the smallest time step length, while the ‘Time convergence’ curve is the error as a function of the dimensionless time step length for the smallest mesh cell length. The ‘Theoretical mesh error’ is the minimum mesh error possible.	31
2.6	Normalized contact pressure profile along the sliding direction, for a dimensionless velocity of 0.4, 0.8 and 1.2 top to bottom. Solid lines are for the current model, dashed lines are from [13]. $x = 0$ is the center of the sphere.	32
2.7	Variation of the apparent steady-state friction coefficient with velocity compared to numerical results from Carbone et al. [18].	33
2.8	Friction curves for different loading times T_0^* for $V^* = 0.8$	34
2.9	Evolution of the maximum friction ratio μ_{max}/μ_{dyn} with the loading time at different sliding speeds.	35
2.10	The adhesive force acting on one point (O) is supposed to be the sum of the interactions between O and all the points of the counter surface (left figure). The simplifying assumption used here is to consider that this force is vertical and only depends on the local gap (right figure).	36

2.11	Load/displacement curves for a viscoelastic Hertzian contact with and without adhesion. The normal displacement is imposed with a constant speed during loading and a two times slower speed during unloading. The analytical solution is from Barthel [31], where the precise parameters of this experiment can also be found.	39
3.1	Illustration of the slope effect in a Hertzian contact. The sphere is sliding to the left over a viscoelastic half space. The friction cone is tilted at the leading edge of the contact, leading to an increase in friction compared to the trailing edge.	44
3.2	Traction boundary with or without slope, with $P = 1$ and $\mu = 1$. The slope is in the x direction.	45
3.3	Traction boundary with or without slope, with $P = 1$ and $\mu = 0.1$. The slope is in the x direction. Using Equation 3.10, a traction T is rectified into T_{rec} in order to comply with the friction law.	48
3.4	Ratio between tangential force and normal force as a function of the slip ratio for a Hertzian contact with a Coulomb friction law. The friction coefficient is 0.4. The simulation is in good agreement with the analytical result from [32].	52
3.5	Number of iterations before convergence as a function of the number of unknowns for different slip ratios. Full lines are for the current model, dashed lines are from Zhao's algorithm [19].	53
3.6	Evolution of the tangential force with time during the sliding of a rigid cylinder on a viscoelastic half-space without friction.	56
3.7	FE result at the end of the simulation of the sliding of a rigid cylinder on a viscoelastic half-space. The shear stress in the bulk is plotted.	57
3.8	Shear stress along the x axis during the transient sliding of a rigid cylinder on a viscoelastic half-space at different times. The dashed lines are for the model, the solid lines for the FE simulations. $x = 0$ is the center of the cylinder.	57
3.9	Top view of the pressure field in a viscoelastic Hertzian contact for two consecutive time steps. The sphere is moving from the bottom to the top of the picture. Numerical instability is responsible for the wavy pressure pattern at the leading edge of the contact.	58
3.10	Mean sliding speed as a function of time for a Hertzian viscoelastic contact. A constant velocity prescribed on the top of the block from time $t = 0$ onward.	60
3.11	Illustration of the algorithm with inertia m : a viscoelastic material (here a simple Zener material) with a prescribed displacement at one end and a mass sliding on a rough surface on the other hand.	61
4.1	Representation of the rough surface used in the comparison against Persson's model	65

4.2	Validation against Persson's model for a speed step experiment. $V_0 = 0.01 \text{ ms}^{-1}$, $V_1 = 3 \text{ ms}^{-1}$	66
4.3	Validation against Persson's model for a speed step experiment for different velocities (with $P_m = 0.1 \text{ MPa}$) and different normal loads (with $V_2 = 0.3 \text{ ms}^{-1}$). The left figures show the evolution of μ_{dyn} and μ_{max} . The right figures show the error between the two models, the current model being chosen as reference.	68
4.4	Dimensionless energy variation during a velocity step experiment. $V_0 = 0.01 \text{ ms}^{-1}$, $V_1 = 3 \text{ ms}^{-1}$	69
4.5	Top view of a periodic surface with two length scales.	70
4.6	Frequency sweep of the shear moduli and damping factor of the material. The vertical bars show the frequencies that are excited during a simulation with the default parameters.	72
4.7	Evolution of apparent friction, contact area and sliding speed with time for the default parameters. The figures on the right are magnifications of the ones on the left in the zone of interest.	73
4.8	Evolution of apparent friction with the lateral displacement for a sliding speed of 30 ms^{-1} compared to the default speed 1 ms^{-1}	73
4.9	Frequency sweep of the shear moduli and damping factor of the material. The vertical bars show the frequencies that are excited during the simulation at $V = 30 \text{ ms}^{-1}$	74
4.10	Evolution of friction with the driving speed, for the default parameters. . .	74
4.11	Evolution of friction and mean gap with the load, for the default parameters and for a smooth surface with only the larger wavelength.	76
4.12	Friction curve with a low normal pressure of $P_m = 4 \times 10^{-3} \text{ MPa}$, for the default surface ($\lambda_1 + \lambda_2$) and the surface without the smaller wavelength (λ_1).	76
4.13	Evolution of friction and mean gap with loading time. The steady-state values have a small dependence on the loading time because true steady-state is not reached, but they should be constant.	77
4.14	Friction curves for a rough and a wavy surface with the default parameters. . .	77
4.15	Evolution of friction coefficient, contact area and sliding area with time for the default parameters with adhesion.	80
4.16	Steady state and maximum friction with and without adhesion as a function of the driving velocity for a contact with a high amplitude wavy surface. The dotted green line is the adhesion indicator C	81

List of Tables

4.1 Default parameters for the simulations 71

Chapter 1

Introduction and bibliography

This chapter introduces the subject studied in this thesis: tire friction and how to model it.

1.1 General introduction

1.1.1 The crucial role of tires

Wheels allow heavy objects to be moved easily by reducing the friction between them and the ground on which they lie. As it is in contact with the ground, the outer part of a wheel is subjected to roll wear. That is why it is fitted with a tire, which is usually made of a more wear-resistant material and can be replaced when worn without changing the entire wheel. While early tires were simple metal rings, they have evolved to become inflated rubber doughnuts which now equip all road transportation vehicles. These pneumatic tires provide wheels with a comfortable air cushion and enhanced traction capabilities because of their rubber tread. These two characteristics made pneumatic tires essential in the development of motor vehicles during the 20th century. They are now highly technical parts of modern cars that need to ensure comfort, performance and safety in a multitude of situations: acceleration, braking, cornering, on a dry or wet road, during winter or summer... Typical car tire performance is based on:

- Dry grip
- Wet grip
- Comfort
- Noise
- Service life
- Low resistance to rolling
- Low cost
- Low environmental impact
- ...

To achieve high overall performance tires are made of several layers of different materials (metal, polymers, rubber...). However improving one performance is often prejudicial to another -most of the time several others- which is why tire designers have to find the best compromise for each application.

The tire tread is the only part of a vehicle in contact with the road. When a driver applies the brakes or takes a curve, it is up to the tire tread to transmit all the subsequent stress to the road. If the tangential stress is too high, for example if a driver brakes too hard without ABS, the tire slips, compromising the stability and handling of the vehicle. Maximizing tire friction allows for higher tangential stress to be applied to the tire before it slips uncontrollably, which makes harder braking and higher cornering speed possible. Both of these performances are paramount in racing vehicles such as MotoGP, as shown in Figure 1.1.

In practice there is always a small amount of slip as soon as an effort is applied to the tire. For example during braking, the speed of the tire tread ωR is always smaller than the speed of the vehicle $V_{vehicle}$. This slip is not uniformly distributed in the contact patch: it only happens at the rear of the contact zone, as shown in Figure 1.2. At first, before the rubber actually touches the road, the tire tread is at rest, no stress is applied to it. As the wheel rolls, the tread enters the contact zone where it bears a normal load (due to the



Figure 1.1: Valentino Rossi during the 2017 Argentina MotoGP race. MotoGP riders reach lean angles as high as 60° . Photo: MICHELIN

weight of the car) and a tangential load (due to braking). The relative displacement of the road compared to the tire belt causes the tread to be sheared. At first, it remains stuck to the road. As shear increases so does the tangential stress until it reaches the friction limit and starts to slip, at the rear of the contact patch. The harder the driver is braking, the larger the slipping area gets. It is when the tread slips in the whole contact patch that a driver starts losing control: in full slip, steering one way or another does not have any effect on the direction of the vehicle.

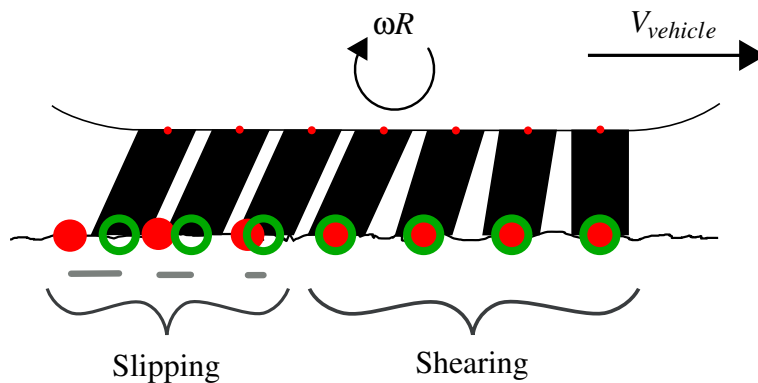


Figure 1.2: Kinematics of the rubber tread during braking.

Tire manufacturers try to maximize the friction limit of the rubber tread compounds and the total amount of energy dissipated during the shearing-slipping process described above for increased security and grip. Experiments show that softer compounds have in general better friction capabilities but shorter service life and higher resistance to rolling. As experimental friction tests on rubber are expensive, analytical and numerical models

are necessary. They are also an appropriate tool to understand the physical phenomena at work.

The subject studied in this thesis is what happens in the contact zone between the tire tread and the road. The problem studied is that of a flat rubber tread sliding on a rough pavement.

1.1.2 Friction forces and their origin

Friction forces between two solids have been studied for centuries. Leonardo Da Vinci studied wood on wood friction using a simple experimental setup (reproduced in [5]), stating that the friction force depended linearly on the normal load with a coefficient $\mu = \frac{\text{tangential force}}{\text{normal force}} = 0.25$. His findings were re-discovered by Amontons in the late 17th century. Using a similar setup shown in Figure 1.3, Coulomb [6] performed a large scale testing campaign using different materials, geometries and surface preparations. He found that the ratio μ was independent of the normal load, of the sliding speed and of the contact area. These observations are the main hypotheses of the Amontons-Coulomb friction law. Coulomb also found that μ depended highly on the materials and on their surface condition. He noticed that the friction coefficient between two bodies at rest was higher than between two sliding bodies.

The Amontons-Coulomb friction law is still used in many applications nowadays because of its simplicity - if this approximation is not good enough, it is easy to modify this law to make the friction coefficient dependent on the various problem parameters such as pressure or velocity.

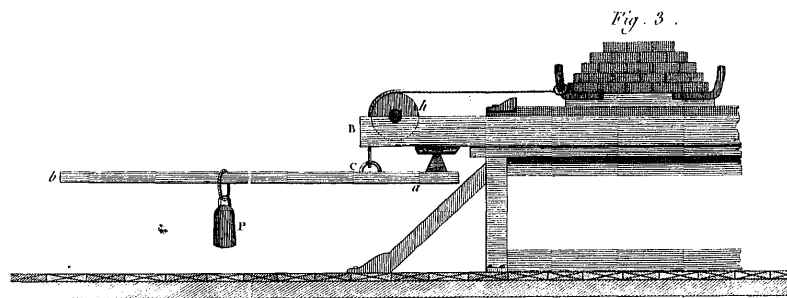


Figure 1.3: Coulomb's tribometer, picture from [6] made available by the Bibliothèque Nationale de France.

In the case of rubber tires, friction is highly dependent on pressure, velocity, temperature and surface roughness. Understanding and predicting this dependence is challenging because friction is caused by several physical phenomena occurring at different scales. The macro-scale corresponds to the length scale at which the experimental observation is made (a few mm).

At meso-scale, (from $0.1 \mu\text{m}$ to 1mm), road roughness deforms the rubber tread at high frequencies as it slides. As rubber is a viscoelastic material, it dissipates energy when it is deformed.

At micro scale (below 100nm), van der Waals forces make the two surfaces attract each other. They cause the adsorption of the long polymer chains of rubber on the road surface. There might also be some covalent bonds forming between the two materials. Because rubber is sliding, these bonds are periodically broken. This bonding/debonding process of weak or covalent bonds also causes energy losses. An illustration of these phenomena is given in Figure 1.4.

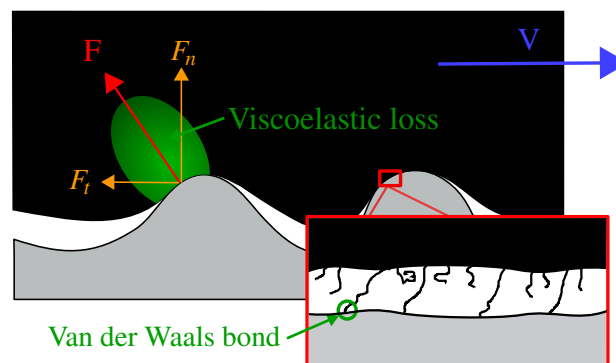


Figure 1.4: Illustration of the physical phenomena causing energy losses during sliding.

The micro scale phenomena do not depend on the local pressure. Most authors agree that they cause a constant shear stress in the contact area during sliding, independent from the local normal pressure. Experimental evidence also supports this hypothesis for very smooth PDMS/glass contacts [8], even for low sliding speeds, in which case viscoelastic losses should be zero. However, if the local shear stress does not depend on the local pressure, the global friction force should be proportional to the contact area, not to the normal load (neglecting viscoelasticity) - which is the opposite of Coulomb's findings. The explanation is that the roughness of real life surfaces make the true contact area different from the apparent contact area. When the Coulomb law is true, it is likely that the real contact area is proportional to the normal load. An extensive review of frictional phenomena can be found in [33].

The present work aims at modeling and understanding tire friction at the meso-scale. Viscoelasticity and surface roughness are the two most important parameters at this scale. What happens at the micro-scale can be modeled independently by an appropriate friction law.

1.1.3 Viscoelasticity and surface roughness

When a shear stress is applied on a perfectly elastic solid, it deforms immediately. Keeping the stress constant for a certain amount of time does not cause any more deformation and the solid goes back to its initial state once the stress is removed. No energy is dissipated

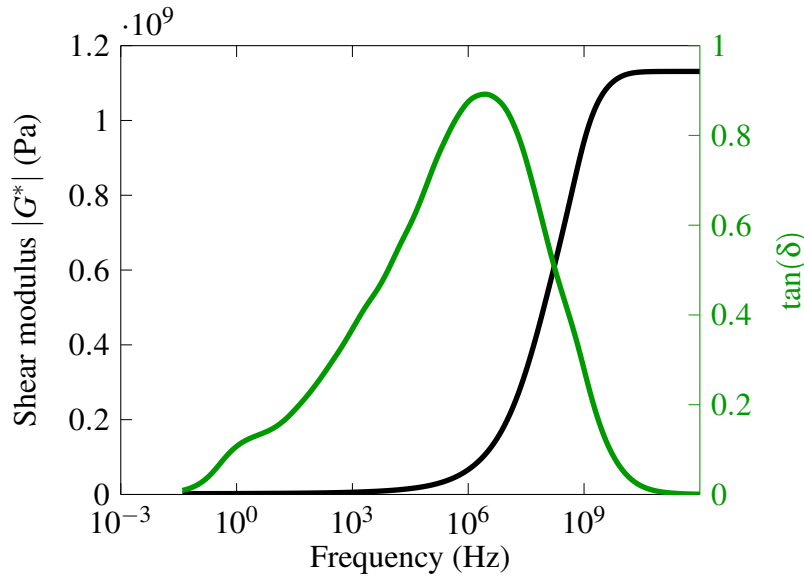


Figure 1.5: Shear modulus amplitude and $\tan(\delta)$ of a typical tire material

in the process. When a shear stress is applied on a perfect fluid, at first it does not move. Keeping the stress constant, the fluid deforms at constant speed (neglecting the inertial effects). When the stress is removed the fluid just stops moving, without getting back to its initial shape. The fluid viscosity causes significant energy losses.

A viscoelastic solid has characteristics from both an elastic solid and a fluid. A constant shear stress causes a deformation that increases with time but is non-zero at $t = 0$. When the stress is removed it takes some time before the solid goes back to its initial state. Contrary to an elastic solid, it dissipates energy when it is deformed.

While crystal-like materials, such as metals, can be modeled as elastic solids in a first approximation, rubber cannot because it is made of long, entangled polymer chains. These chains can move relatively to each other as they mostly interact through weak van der Waals forces (except cross-linking due to vulcanization). The energy barrier between two equilibrium positions is quite low. The probability to cross it is relatively high and increases with the temperature and with time. Consequently rubber is apparently soft at high temperature and long time scales, it is apparently hard at low temperature and short time scales (temperature and time play the same role).

Viscoelastic materials can be characterized using periodic loading tests. Under periodic loading, there is a phase difference δ between the applied stress and the deformation, which represents the energy losses. Because of this phase difference, the ratio between shear stress and shear deformation can be represented as a complex modulus $G^* = G' + iG'' = |G^*|e^{i\delta}$, where $i = \sqrt{-1}$.

Figure 1.5 shows the evolution of the apparent shear modulus with the frequency of a typical tire material. At high frequencies rubber behaves like a stiff elastic solid, at low frequencies like a soft elastic solid. Energy dissipation only occurs for intermediate frequencies.



Figure 1.6: Close-up photography of a road pavement. Photo by Angel Caboodle under the license CC BY-SA 3.0

The pavement of most roads in Europe is made up of a mineral aggregate (crushed stone, gravel, sand...) bound together by asphalt (Figure 1.6). The aggregate size covers several orders of magnitudes and more importantly the particles are not smooth. As a consequence road surfaces are rough from the nanometer up to the millimeter scale. All the length scales *a priori* have an influence on the viscoelastic losses: tires typically slide at 1 ms^{-1} , so the corresponding frequency of the deformation induced by the surface roughness ranges from 1000 Hz to 1 MHz.

1.2 Bibliography: experimental and theoretical results for a contact at the meso-scale

1.2.1 Hertzian contact

A simple and common approach to model contact is to consider a sphere in contact with an elastic half-space. An elastic half-space is an elastic solid that is infinitely large in all directions. It is a reasonable hypothesis for the present case, as the road roughness is much smaller than the rubber tread. Boussinesq [34][35] found a solution to relate the surface pressure to the surface displacement in such a solid. This relation is only the first step to find the solution of the contact of a sphere with a half-space. A contact problem is by definition a mixed boundary value problem. In the contact zone, the displacement is prescribed: the solid must have the shape of the sphere it is in contact with. Outside, the pressure is prescribed to zero: if there is no contact, the sphere cannot produce a

pressure on the solid surface. What makes things even more difficult is that the contact zone is not known beforehand. The half-space approximation makes the problem axis-symmetrical, which means the contact zone is axis-symmetrical and all that remains to find is the contact radius and the shape of the pressure field. Hertz found the solution in 1880. He found the pressure field was a paraboloid and expressed the equations governing the normal displacement, normal load and contact radius- given in Equation 1.1, as reported in [36].

$$\begin{aligned} a &= \left(\frac{3 F_n R}{4 E^*} \right)^{1/3} \\ \delta &= \frac{a^2}{R} \end{aligned} \tag{1.1}$$

a is the contact radius, F_n the normal force, R the radius of the sphere and E^* the equivalent Young modulus such that $1/E^* = (1 - \nu_1^2)/E_1 + (1 - \nu_2^2)/E_2$, E_i and ν_i , $i = 1, 2$ being the Young moduli and Poisson ratios of the two solids.

Hertz' solution as well as Boussinesq's are for an elastic solid undergoing small strain. In particular it means that in the contact zone the slope of the sphere (the inclination of the normal to the sphere compared to the vertical axis) should remain small, which implies that the contact radius should remain small compared to the radius of the sphere R .

Hertz also made the assumption that there was no friction at the interface, or in other words that the surface stress was only in the vertical direction. Not until 1949 was the Hertzian contact with friction problem solved by Mindlin [32]. He used a Coulomb friction law and found that when a tangential displacement is imposed, the contact zone divides into a stick disc in the center where there is no slip and a slip annulus at the edge. The slip is in the same direction as the tangential displacement in all the annulus and its intensity is an increasing function of the radius. As the tangential displacement increases, the stick zone becomes smaller and smaller until it disappears and full sliding occurs.

1.2.2 Adhesion

Van der Waals forces are not only responsible for friction -shear stresses in the contact zone as described in section 1.1.2- but they also cause tensile stresses to develop in the contact zone, which are called adhesive forces. For smooth surfaces that are relatively soft their effect cannot be neglected. The most noticeable effect is that separating two smooth surfaces in contact requires energy proportionally to the contact area. For spherical contacts, it causes the contact radius to be sensibly larger than the Hertzian prediction. This phenomenon was first modeled by Johnson, Kendall and Roberts (JKR) [37] who assumed adhesion had no impact outside of the contact area. Shortly afterwards Derjaguin, Muller and Toporov (DMT) [38] made a similar model assuming that the displacement field remained Hertzian and that adhesive forces were also present outside of the contact zone, leading to different results. Tabor [39] defined a dimensionless parameter given in

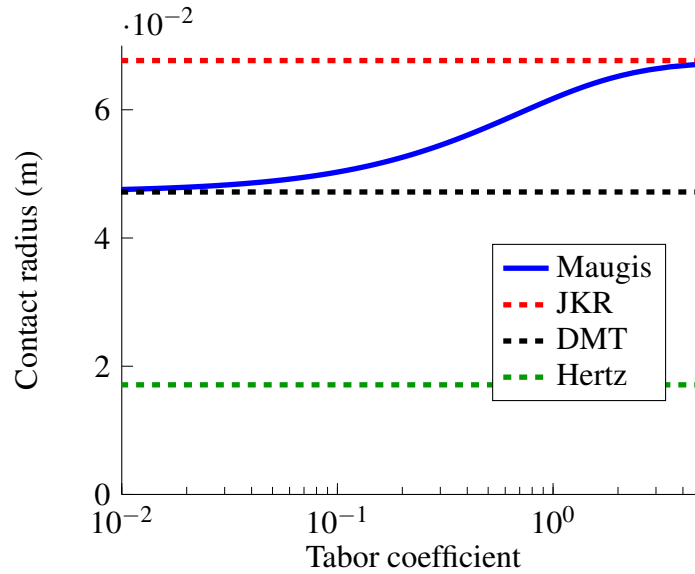


Figure 1.7: Evolution of the contact radius with the Tabor coefficient for a Hertzian contact with adhesion. The ‘Hertz’ solution is the contact radius without adhesion. The radius of the sphere is 1 m, the normal force is 1×10^{-5} N, the adhesive energy is 3.2×10^{-5} J m $^{-2}$ and the material is incompressible and elastic with a shear modulus of 0.37 Pa.

Equation 1.2 for a Hertzian contact with adhesion.

$$\mu_t = \frac{R^{1/3} \gamma_0^{2/3}}{z_0 E^{*2/3}} \quad (1.2)$$

R is the radius of the sphere, γ_0 the work of adhesion, z_0 the characteristic length of the interaction and E^* the equivalent Young modulus. Maugis [40] proved in 1992, through a more general analytical model that the JKR theory is valid for high Tabor numbers (>5), which means short range adhesion and soft surfaces while the DMT theory is valid for low Tabor number (<0.1), that is for long range adhesion and hard surfaces [41]. Figure 1.7 shows Maugis’ solution of the contact radius and its evolution with the Tabor coefficient compared to the DMT and JKR theories.

One of the reasons why the problem of Hertzian contact with adhesion has received so much attention is that it is relatively easy to reproduce experimentally. This kind of experiments are often called ‘JKR tests’ because by measuring the normal force during the separation of a sphere from a flat surface and using JKR equations (or Maugis/DMT equations if necessary), one can deduce the adhesion energy of the two surfaces.

However, this technique sometimes leads to an inconvenient result: the adhesion energy seems to depend on the separation speed, which should not be the case because time does not appear in the different analytical models (see for example [42]). Of course it can come from the adhesion phenomenon itself - as the physical explanation of adhesion is not very well defined it is hard to say it cannot. But bonding/debonding processes and more importantly van der Waals forces have characteristic times that are several or-

ders of magnitude shorter than the experimental times, so this explanation is not entirely satisfying. What is more likely, in particular for rubber applications, is that the material viscoelasticity causes a significant amount of energy dissipation during the peeling process.

1.2.3 Viscoelasticity

The stress/strain relation of viscoelastic materials is time dependent. Restricting to the case of linear viscoelasticity, it can be expressed using an integral formulation (Equation 1.3) or a differential formulation (Equation 1.4). Both of them are equivalent [43].

$$\begin{aligned}\underline{\underline{\sigma}}(t) &= \int \underline{\underline{\psi}}(t-t') : \underline{\underline{\dot{\epsilon}}}(t') dt' \\ \underline{\underline{\epsilon}}(t) &= \int \underline{\underline{\phi}}(t-t') : \underline{\underline{\dot{\sigma}}}(t') dt'\end{aligned}\quad (1.3)$$

$$\sum_{i=0}^n \underline{\underline{S}}_i : \frac{\partial^i \underline{\underline{\sigma}}}{\partial t^i} = \sum_{i=0}^n \underline{\underline{R}}_i : \frac{\partial^i \underline{\underline{\epsilon}}}{\partial t^i} \quad (1.4)$$

$\underline{\underline{\epsilon}}$ is the strain, $\underline{\underline{\sigma}}$ is the stress and a dot denotes a time derivative. $\underline{\underline{\phi}}(t)$ is called the creep compliance function matrix and describes the response to a unit stress increment, while $\underline{\underline{\psi}}(t)$ is called the relaxation function matrix and describes the response to a unit strain increment. In the general case these matrices are composed of two time dependent functions corresponding to the two elastic parameters (one function corresponds to the Young modulus and one to the Poisson ratio for example). However, rubber can reasonably be considered to be an incompressible material so its temporal response is described by only one function, so the creep compliance and relaxation functions can be written as $\underline{\underline{\phi}}(t) = \phi(t) \underline{\underline{S}}$ and $\underline{\underline{\psi}}(t) = \psi(t) \underline{\underline{R}}$.

$\underline{\underline{S}}$ and $\underline{\underline{R}}$ are equivalent to compliance and stiffness tensors in elasticity.

With only one time-dependent function, the time response of rubber materials can be described by simple models such as the Standard Linear Solid model, represented in Figure 1.8. Using models allows the relaxation and creep functions to be fully determined by a finite number of variables (3 for the Standard Linear Solid), which is useful both for their experimental determination and in particular for the implementation of viscoelasticity in analytical or numerical models.

For most problems, finding the viscoelastic solution is not as complicated as it may seem. Lee [44] was the first to realize that in the Laplace domain the viscoelastic problem is similar to the elastic one. Consequently, it is possible to get the time-dependent viscoelastic solution of a given problem simply by using the elastic solution and replacing the elastic constants by the viscoelastic functionals. Unfortunately this technique only works if the boundary conditions can be easily described in the Laplace space, which is not the case for the contact problem as the contact area changes over time. In the continuation of Lee's work, Radok [26] extended the method to more general boundary conditions, he

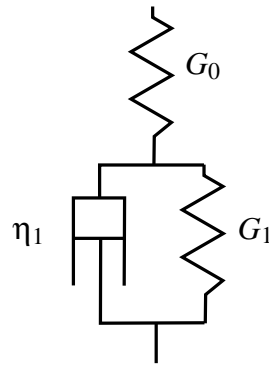


Figure 1.8: Representation of the Standard Linear Solid. G_0 and G_1 are the stiffness of the two springs, η_1 is the viscosity of the dashpot.

called this method the functional equations method. Lee and Radok [30] showed that the functional equations method was valid for growing contact surfaces only - for a Hertzian contact, it means increasing contact radius only. Only through a much more complex method was the receding contact problem solved in 1966 by Ting [45].

Accounting for adhesive forces in a viscoelastic media is similar to studying the propagation or closing of a crack. This has been studied by Schapery, who first derived a solution for the opening of a crack in a viscoelastic material [46] and later for a closing crack [47]. In this latter paper, he applies his theory for the adhesion of viscoelastic spheres, assuming the cohesive zone is very small compared to the contact size. This way the contact problem is the superposition of two problems. On the one hand, the problem of viscoelastic contact and on the other hand the problem of viscoelastic crack propagation. Viscoelastic dissipation happens in the bulk due to the deformation induced by the spherical shape in contact and also the strong and short-range adhesive forces at the edge of the contact produce viscoelastic dissipation during growing and peeling of the contact. Barthel [48] shows that viscoelasticity coupled with adhesive forces creates an apparently higher surface energy, in particular at high crack propagation speeds. The full resolution of viscoelastic, adhesive spheres in contact was obtained by Haiat [49].

1.2.4 Surface roughness

As introduced in section 1.1.3, road surfaces are rough over several length scales. Several methods exist to measure their surface roughness. A first class of method is ‘stylus based’: the principle is to drag a very sharp needle across a sample and measure its deflection. It is probably the oldest method as stylus profilometers have existed at least since 1941 [50]. The resolution of such methods depends on the tip size and its shape can cause measurement artifacts. It measures only a line across a 2D surface, which may not be representative if the surface is not isotropic. Two-dimensional measurements can be achieved by measuring the surface line by line though this technique is quite slow. AFM (Atomic Force Microscopy) techniques use basically the same principle except that the tip can be as small as a few nanometers [51] allowing for a very fine resolution. Another category of

measurement methods is based on light scattering, either of monochromatic or of white light. Though they produce measurement artifacts if the surface reflexive properties are not homogeneous, or if the local slope is too high, they are relatively fast methods. The resolution can be quite high for monochromatic light and can be improved by using X-rays instead of visible light. Confocal microscopy is another optical measurement method. It is more robust than interferometric methods and can achieve 10 nm resolution as well. The idea is to determine for each point its focal plane, which determines its height.

Of course no analytical model can directly be applied to a measured surface. Instead some meaningful statistical properties of the given surface are used. The Power Spectral Density (PSD) is probably one of the most used statistical parameter of a surface, not only in contact mechanics but also in other fields such as optics [52] etc... The PSD represents the amplitude of the Fourier Transform of the surface height at each wavevector $\mathbf{k} = (k_x, k_y)$ - see Equation 1.5.

$$\Phi(k_x, k_y) = \frac{|\hat{h}(k_x, k_y)|^2}{A} \quad (1.5)$$

A is the total surface area and \hat{h} is the 2-dimensional Fourier transform of the surface h . Jacobs *et al.* [51] made a precise review of the different definitions of a PSD and how to calculate it.

A surface PSD is useful to compute more meaningful surface parameters. Road surfaces are often considered to be self-affine. It means they are ‘fractal-like’ and have a similar roughness properties from the nanometer up to the millimeter scale. It causes the PSD to have a constant slope when plotted with a logarithmic scale. This slope is representative of the fractal dimension and Hurst exponent. A PSD of a typical road surface follows Equation 1.6, as shown in Figure 1.9 [53].

$$\Phi(|\mathbf{k}|) = \begin{cases} C & \text{if } k_l < |\mathbf{k}| < k_r \\ C \left(\frac{|\mathbf{k}|}{k_r} \right)^{-2(1+H)} & \text{if } k_r < |\mathbf{k}| < k_s \\ 0 & \text{otherwise} \end{cases} \quad (1.6)$$

$|\mathbf{k}|$ is the norm of the wavevector \mathbf{k} . k_l is the lower wavenumber cut-off, k_r the roll-off wavenumber and k_s the upper wavenumber cut-off. H is the Hurst exponent.

Other meaningful statistical parameters of a rough surface such as its height RMS h_{rms} , its slope RMS ∇h and its summit mean curvature h'' can be derived from the PSD [54].

Simplifying a rough contact by a simple Hertzian contact is only a crude approximation. The multi-asperity approach initiated by the pioneering work of Greenwood and Williamson [1] generalizes Hertz’ result by using an infinite distribution of spheres of different height and different radii. The radius and height distributions are derived from the summit height distribution and the summit curvature distribution of the rough surface under consideration. For an elastic contact at low normal loads, it predicts a linear relation between load and real contact area which is compatible with Coulomb’s friction law if the

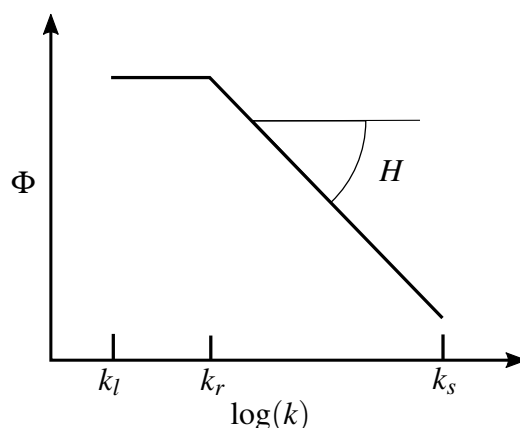


Figure 1.9: Typical PSD of a road surface.

shear stress is considered to be constant in the true contact zone. It has been studied and modified by many authors: initially all the spheres had the same radius, until the modification by Bush, Gibson and Thomas [2], later simplified in [55]. A review can be found in [56]. It has also been extended to viscoelastic, adhesive contacts in [57].

The major criticism of multi-asperity approaches is that, as they are more or less a sum of Hertzian contacts, they do not take into account the influence asperities have on each other, so should remain valid only at low normal loads. Persson's model [3][4] overcomes this problem by using a completely different approach. His main hypothesis is that the PSD of the rubber surface is the same as the PSD of the road surface it is in contact with - which is *a priori* only valid for full contact, but that he shows is a reasonable hypothesis in most cases [58]. This approach was from the beginning developed for viscoelastic materials sliding at constant speed without friction. It allows one to find the roughness length scales that dissipate the most energy for a given normal load and sliding speed, as well as the corresponding true contact area. A major result of his approach, which follows the intuition, is that the true contact area decreases when smaller and smaller length scales are accounted for - and disappears entirely under some conditions if the surface is considered to be self-affine down to infinitely small length scales. Such an extrapolation is wrong though, as the continuum mechanics equations his model is based on are wrong at the atomic scale. A delicate question arises: what is an appropriate short wavelength cut-off? Though some guidelines exist [59], it remains an open question.

An illustration of the results from Persson's model is given in Figure 1.10. It shows the evolution of apparent friction coefficient with the sliding velocity for the contact of a typical tire rubber on a self-affine rough surface (its PSD is similar to the one given in [59]). The normal pressure is 1 bar. The curve has a typical bell shape caused by the viscoelastic characteristics of rubber: it only dissipates energy in a transition zone and behaves like an elastic solid at low and high frequencies. The friction coefficient is rather low: ≈ 0.3 whereas typical friction coefficient of rubber on a dry road is ≈ 1.3 . The reason is that Persson's model only accounts for the viscoelastic part of friction at length scales between $0.1 \mu\text{m}$ and 1mm .

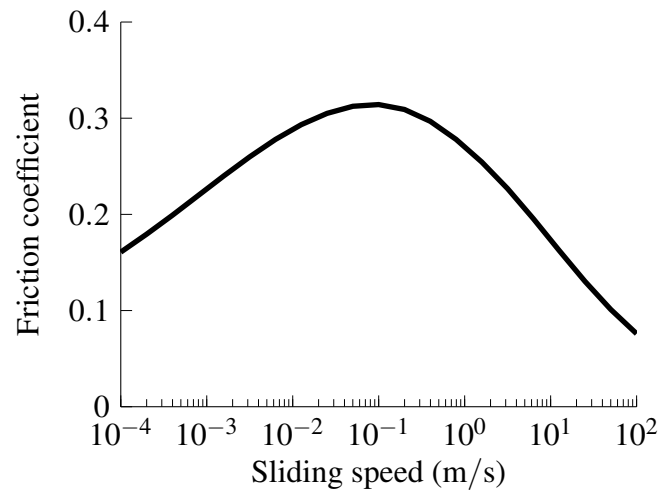


Figure 1.10: Evolution of the friction coefficient with the sliding speed according to Persson's model.

It should be mentioned that Persson's model has been extended to tackle transient sliding problems [28] and to include thermal effects [60]. Thermal effects have an influence on rubber contacts because viscoelastic losses change the temperature field and the material characteristics strongly depend on temperature. However these effects are outside the scope of the present study.

1.2.5 Numerical methods

Analytical methods for rough contact all rely on hypotheses. Finding out which of them are reasonable is difficult using only experimental evidence. Numerical simulations are of great help for this task because all the physical phenomena modeled in the simulations can be switched on and off at will, making them a powerful tool for understanding what happens -and what does not- in a rough contact.

The Finite Element Method (FEM) seems, at first sight, to be the appropriate method for contact simulation. FEM has been developed for decades and commercially available softwares-such as Abaqus or COMSOL Multiphysic- allow for different physics to be used in a single simulation, which means one could in principle perform a contact simulation with dynamic effects, adhesion, friction, viscoelasticity, thermal effects, finite deformations... without having to implement anything. Though some authors have used FEM for contact simulations (for example [7]), it is not the most popular method. Its major drawback is that it does not take advantage of the half-space hypothesis described in Section 1.2.1. Consequently meshing in the 3 dimensions is necessary. Though it is reasonable to mesh in 3D a simple Hertzian contact, it gets more complicated for rough surfaces. The shortest roughness length scale λ_s considered in a simulation should be discretized with elements ≈ 10 times smaller to achieve meaningful results. Similarly, the total length of the simulation should be larger than the larger roughness length scale λ_l (≈ 4 times larger

according to Yastrebov [53]). Assuming a regular mesh with the same mesh size in all directions, the total number of elements in the simulation is $\approx (40 \frac{\lambda_l}{\lambda_s})^{\text{number of spatial dimensions}}$ which is ≈ 64 billion for a 3-dimensional mesh and a ratio $\frac{\lambda_l}{\lambda_s} = 100$ (for a road surface represented from 100nm up to 1mm, the ratio is $\frac{\lambda_l}{\lambda_s} = 10000$). Running a simulation on such a large mesh would be -despite the high performance of recent FEM solvers- extremely expensive, if at all possible. For a dry contact problem, this number can be reduced because the stress gradient is only high in a thin layer below the surface - its thickness is approximately the size of the surface asperities. Consequently the mesh can be coarsened in the upper layers of the solid, as described in [61], which reduces the number of elements to $\approx (40 \frac{\lambda_l}{\lambda_s})^2 \log(40 \frac{\lambda_l}{\lambda_s}) \approx 133$ million.

The half-space hypothesis allows even further reduction. Using Boussinesq's equations, Love [62] found the surface displacements induced by a uniform pressure applied on a rectangular area at the surface of an elastic half-space. The principle of Boundary Element Methods (BEM, sometimes named semi-analytical methods) is to discretize the surface *and only the surface* of the solid and to use Love's results to solve the contact problem. In other words, the half space approximation allows the 3-dimensional contact problem to be solved using only a 2-dimensional mesh. The total number of elements required for a ratio $\frac{\lambda_l}{\lambda_s} = 100$ is only 16 million, so that the simulation can be run on a standard desktop computer. BEM for contact problems has been described extensively in Kalker's book [9] where he describes the Influence Coefficient matrices (equivalent to rigidity matrices in FEM) for elastic half-spaces and appropriate solvers for contact problems with or without friction. He shows the existence and unicity of the solution of the contact problem even with friction. A few years later Stanley and Kato [10] first used Fast Fourier Transforms to compute the displacements from the pressure field using a uniform mesh and a periodic problem, reducing the computational cost from $O(N^2)$ to $O(N \log(N))$ (N being the number of variables). Liu [11] showed that this method could be extended to non-periodic problems using the appropriate zero-padding. Brand and Lubrecht [63] developed a multi-level multi-summation technique which allows for the same speed-up of the computation.

Another approach is to use a mesh smart enough to reduce the number of variables without impacting precision. This is achieved by refining the mesh at the edges of contact clusters only and keeping a relatively coarse mesh in the inner part. This 'Active Sets' methods are developed in [64].

Contact solvers also evolved. Kalker's solver is composed of two loops: the inner loop computes the pressure field giving the appropriate displacement in the contact surface, while the outer loop updates the contact surface. More recent algorithms [12][24] use only one loop where the contact surface is updated on the fly. Comparisons of different BEM models can be found in [24][65].

Beginning with the GFMD method [66], some authors have used molecular dynamics

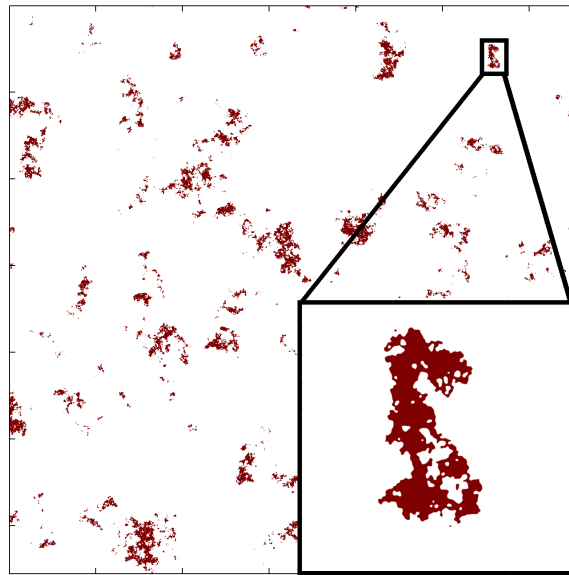


Figure 1.11: Top view of the numerically computed contact area between a rough surface and an elastic half-space with short range adhesion, as described in [29]. The magnified contact spot shows the very fine resolution of the mesh.

solvers to solve the contact problem which proved to be efficient. These simulations use the half-space approximation and Boussinesq's equations, which are implemented in a molecular dynamics solver.

Molecular dynamics solvers have the ability to account for normal adhesion in a contact problem, which has been used for example by Muser [67]. He announced a Contact mechanics modeling challenge in 2015 [29]. The aim of this challenge was to solve, using numerical, analytical or experimental methods, a multi-scale rough contact problem with short range adhesion, which he solved using GFMD with a very fine grid on a super-computer. Among the 13 answers from 12 different groups, 6 are numerical methods: 2 of them are based on molecular dynamics solvers and 4 of them are BEM methods. All of them were successful, which shows that adhesion can be implemented in BEM codes without any major problem. Figure 1.11 shows the contact area of the solution.

Solving the contact problem with friction using BEM has been studied by different authors such as [19, 20, 21, 22] and proves to be quite difficult. In the general case, the normal and lateral displacements are coupled so both the contact problem and the friction problem should be solved simultaneously. If the two contacting materials are the same, or if one is incompressible and the other rigid (as is the case in rubber/road contact), the coupling disappears, but other nonlinearities remain. The first reason is that in transient sliding only part of the contact area is actually sliding, while the rest remains stuck. It gives rise to a strong non-linearity as the boundary conditions are not the same: the displacement is imposed in the stuck area and the norm of the shear stress is imposed in the sliding area. In addition to this in the sliding zone, the local sliding direction should be the same as the shear stress direction. This last condition is omitted by some [21] who sup-

pose that the shear stress is always in the global, imposed sliding direction. In a Hertzian contact with friction, Johnson [36] shows that displacements in the direction perpendicular to the global sliding direction are of the order of $v/(4 - 2\nu) \approx 0.15$ compared to the displacement parallel to the sliding direction. Zhang does take the direction into account by using polar coordinates for the stress in the sliding zone: the stress norm is given by Coulomb's friction law and its direction is an unknown variable.

Viscoelasticity has also received much attention. Implementing viscoelasticity in a BEM code can be done by using 'standard' procedures as described in [25] or [68]. An integral formulation of viscoelasticity is used in [13, 14, 15, 16]. Using the creep or the relaxation function and discretizing Equation 1.3 with respect to time, it is possible to solve transient viscoelastic problems. As Equation 1.3 depends on the loading/displacement history it is necessary to keep in memory the stress (or displacement) of all the time steps, which may be exceedingly demanding for fine resolution or a large number of time steps.

A differential formulation of viscoelasticity is used in [17] which is based on the first order discretization of Equation 1.4. With this formulation a finite number of state variables in addition to the stress (or displacement) need to be kept in memory, but only for the previous time step, so the memory requirement does not depend on the number of steps. Other authors such as [18] focused on steady-state viscoelasticity. Considering that the two contacting bodies are sliding without friction at constant speed (and that the problem is periodic) the problem of steady-state sliding can be solved with only one iteration.

1. Introduction and bibliography

Chapter 2

Numerical model for frictionless contacts and application to Hertzian contacts

A numerical model for the simulation of contact between a half-space and a rigid surface is presented. Viscoelasticity and adhesive forces are accounted for efficiently. Examples and validation for Hertzian contacts are presented.

2.1 Numerical model for normal contacts

2.1.1 Discretization and FFT-convolution

As mentioned in section 1.2.1, a contact problem is a mixed boundary value problem. Solving the problem of a half-space in contact with a rigid surface is finding the surface pressure field $P(X)$ such that:

$$\begin{aligned} P(X) &\geq 0 \quad \forall X \\ U_z(X) - H(X) &\geq 0 \\ U_z(X) &= H(X) \quad X \in S_c \\ P(X) &= 0 \quad X \in \neg S_c \end{aligned} \quad (2.1)$$

X is the position, U_z the normal displacement, H the height of the rigid surface and S_c is the contact surface. $U_z(X) - H(X)$ is the gap between the two surfaces. Boussinesq's equation (see Equation 2.2) describes the relation between pressure and normal displacement for an elastic half-space:

$$U_z(X) = \frac{1-\nu}{2\pi G} \iint_{\Omega} \frac{P(X')}{\|X - X'\|} dX' \quad (2.2)$$

G is the shear modulus of the half-space, ν the Poisson ratio, X and X' are spatial variables ($\|X - X'\|$ is the distance between them).

This integral is defined over all the half-space -which is, by definition, infinitely large- which makes its numerical computation difficult. Fortunately, for a contact problem, the pressure is zero outside of the contact zone, so integrating over the contact surface only is sufficient.

Another possibility is to consider that the contact is periodic, so that P is known in all the half-space. The integral is best computed in the Fourier space, where Boussinesq's equation reads:

$$\widehat{U}_z(\xi) = \frac{1-\nu}{2\pi G} \widehat{a_{zz}}(\xi) \widehat{P}(\xi) \quad (2.3)$$

where $\widehat{}$ denotes a Fourier transform and $a_{zz} : X \rightarrow \frac{1}{\|X\|}$. As Boussinesq's equation in the real space is a convolution product, it turns into a simple multiplication in the Fourier domain.

In the periodic case the problem is defined on a square which size is the period of the contact. The first step to build the numerical model is to discretize this surface into N^2 square elements. All the elements are the same size. Given the pressure $P(i, j)$ at the center of each element (i, j) , deriving the corresponding normal displacement $U_z(i, j)$ can be done efficiently with a Fast Fourier Transform (FFT) using Equation 2.4.

$$U_z = \text{FFT}^{-1}(\text{FFT}(A_{zz})\text{FFT}(P)) \quad (2.4)$$

A_{zz} is the discretized version of a_{zz} , it is called the Influence Coefficient matrix.

Similarly, for a non-periodic problem, the first step is to mesh a square of the half-space surface where the contact is likely to occur: there cannot be any point in contact outside of this area. Once again the surface is discretized into N^2 regular square elements. The pressure field is assumed to be constant over an element, the corresponding displacement is then found in [62]. The relation between pressure and displacement can be written as $U_z = A_{zz}^{np} P$ where A_{zz}^{np} is the non-periodic Influence Coefficient matrix. Following the method described in [11] the size of the pressure field P is doubled in each direction and padded with zeros. The corresponding displacement field also has its size doubled, but now the relation $U_z = A_{zz}^{np} P$ has an advantageous property: the matrix A_{zz}^{np} is now a convolution matrix and the matrix multiplication can be done in the Fourier domain as in Equation 2.4. Moreover, when the displacement field U_z is truncated back to its original size, the periodicity of the problem induced by the Fourier transform does not have any impact so the convolution is exact.

For the rest of this work the periodic and non periodic influence coefficient matrices will both be denoted A_{zz} . The periodic and non-periodic problems are in every way similar except for the zero-padding technique and slightly different influence coefficient matrices.

2.1.2 Conjugate Gradient algorithm for normal contact without adhesion

The numerical model developed is similar to the one presented in [12] and [24]. A conjugate gradient algorithm is developed to find the pressure field P solution of the contact problem. Let us introduce the functional $\mathcal{F} = P^T \cdot H - \frac{1}{2} P^T \cdot A_{zz} \cdot P$. For a given contact surface S_c and if $P = 0$ outside of it, $\frac{\partial \mathcal{F}}{\partial P}$ is given in Equation 2.5.

$$\frac{\partial \mathcal{F}}{\partial P} = \begin{cases} H - A_{zz} \cdot P & \text{if } (i, j) \in S_c \\ 0 & \text{if } (i, j) \in \neg S_c \end{cases} \quad (2.5)$$

Solving the contact problem is consequently equivalent to finding P such that $\frac{\partial \mathcal{F}}{\partial P} = 0$, in other words it is equivalent to minimizing the functional \mathcal{F} . As \mathcal{F} is quadratic, it can be minimized efficiently using a Conjugate Gradient algorithm. This algorithm is a loop which, starting from an initial guess of the pressure field P_0 , converges towards the solution of the problem P_* .

At the end of iteration n , the pressure field is P_n , the residual is $r_n = H - A_{zz} \cdot P_n$ in S_c ($r_n = 0$ outside of it) and the search direction is d_n .

The first step of iteration $n + 1$ is to find $P_{n+1}^t = P_n + \alpha d_n$. α is a scalar chosen to minimize \mathcal{F} . It is given in Equation 2.6.

$$\alpha = \frac{r_n^T \cdot d_n}{d_n^T \cdot A_{zz} \cdot d_n} \quad (2.6)$$

At this point, if the mean normal pressure is prescribed by P^m , the pressure field P_{n+1}^t is corrected in order to satisfy $\bar{P}_{n+1} = P^m$. A convenient way to achieve this is to set $P_{n+1} = P_{n+1}^t * \frac{P^m}{\bar{P}_{n+1}}$.

The new residual is computed $r_{n+1} = H - A_{zz} \cdot P_{n+1}$.

The new contact surface is computed. It is defined as the set of points where the pressure is positive or where the residual is positive. The new residual is set to 0 outside of the new contact surface.

The last step of the algorithm is to compute the new search direction d_{n+1} from the new residual. In order to achieve a fast convergence d_{n+1} is computed in order to be A_{zz} -orthogonal to d_n , that is to say $d_{n+1}^T \cdot A_{zz} \cdot d_n = 0$. This is achieved by setting $d_{n+1} = r_{n+1} + \beta d_n$ where β is given by Equation 2.7

$$\beta = -\frac{r_{n+1}^T \cdot A_{zz} \cdot d_n}{d_n^T \cdot A_{zz} \cdot d_n} = \frac{r_{n+1}^T \cdot (r_{n+1} - r_n)}{\alpha d_n^T \cdot A_{zz} \cdot d_n} \quad (2.7)$$

For a linear problem, the exact solution is found after N^2 conjugate gradient iterations, as N^2 is the number of mesh cells and consequently the number of unknown variables. But knowing the exact solution is not necessary: what is needed is only an approximation of the exact solution and each iteration of conjugate gradient gives a better one.

The convergence criterion chosen here is the Root-Mean-Square (RMS) of the residual normalized by the characteristic length of the problem. When this convergence criterion is below a given tolerance, the result is considered to be precise enough and the loop stops.

It can be shown that for a perfectly linear problem, d_{n+1} is A_{zz} -orthogonal to all the previous search directions: $d_{n+1}^T \cdot A_{zz} \cdot d_k = 0, \forall k < n + 1$. Also the residual can be computed with $r_{n+1} = r_n - \alpha A_{zz} \cdot d_n$, so only one matrix multiplication ($A_{zz} \cdot d_n$) is necessary at each step. These two properties make the conjugate gradient algorithm very effective in this case.

Unfortunately the present contact problem is linear only if the contact surface remains the same during all the iterations and if the mean normal displacement is imposed, not the nominal pressure. Consequently this last simplification for the residual computation cannot be used. However as the algorithm converges towards the solution the problem becomes more and more linear so a fast convergence is achieved.

The most time-consuming parts of each iteration of the algorithm are the Fast Fourier Transforms used to perform the matrix multiplications: $A_{zz} \cdot P_{n+1}$ for the computation of the residual and $A_{zz} \cdot d_n$ for the computation of α and β . Following Equation 2.4, a matrix multiplication requires one FFT and one inverse FFT to be performed, both being equally time-consuming (computing $\text{FFT}(A_{zz})$ is only required once and not at each iteration). For the computation of α and β , computing $A_{zz} \cdot d_n$ is in fact not necessary as only $d_n^T \cdot A_{zz} \cdot d_n$ is required. This parameter can be computed with only one FFT using Parseval's theorem, which leads to Equation 2.8, where N^2 is the number of mesh cells. Using this simplification only 3 FFTs (or inverse FFT) are performed per iteration instead of 4, which significantly speeds up the computation.

$$d_n^T \cdot A_{zz} \cdot d_n = \frac{1}{N^2} \text{FFT}(d_n)^T \cdot \text{FFT}(A_{zz}) \cdot \text{FFT}(d_n) \quad (2.8)$$

2.1.3 Viscoelasticity

A differential formulation of viscoelasticity [25] is chosen to model the transient viscoelastic behaviour of rubber. The Zener, or Standard Linear Solid viscoelastic model is used - see Figure 1.8.

An incompressible viscoelastic material such as rubber with a Zener law follows the differential equation 2.9, where s and e are the deviatoric parts of the stress and strain tensors, the dot denotes a time derivative.

$$\left(1 + \frac{G_1}{G_0}\right) s + \frac{\eta_1}{G_0} \dot{s} = 2G_1 e + 2\eta_1 \dot{e} \quad (2.9)$$

Using Radok's method of functional equations as described in section 1.2.3 for a Zener material and applying it to the Boussinesq elastic potential yields the viscoelastic Boussinesq Equation 2.10.

$$\iint_{\Omega} \frac{1}{4\pi\rho} \left(P(\xi, \eta) \left(1 + \frac{G_1}{G_0}\right) + \frac{\eta_1}{G_0} \dot{P}(\xi, \eta) \right) d\xi d\eta = G_1 U_z(x, y) + \eta_1 \dot{U}_z(x, y) \quad (2.10)$$

with $\rho = \sqrt{(x - \xi)^2 + (y - \eta)^2}$

Equation 2.10 is discretized in space and leads to Equation 2.11.

$$A_{zz} \cdot P \left(1 + \frac{G_1}{G_0}\right) + \frac{\eta_1}{G_0} A_{zz} \cdot \dot{P} = G_1 U + \eta_1 \dot{U} \quad (2.11)$$

Assuming that pressure and displacements vary linearly between time steps t and $t + \Delta t$ leads to Equation 2.12. This assumption is wrong in the general case, but provided the time step Δt is small compared to the characteristic time $\tau = \frac{\eta_1}{G_0 + G_1}$ it is reasonable.

$$A_{zz} P_{t+\Delta t} \left(1 + \frac{G_1}{G_0}\right) + \frac{\eta_1}{G_0} A_{zz} \frac{\Delta P}{\Delta t} = G_1 U_{t+\Delta t} + \eta_1 \frac{\Delta U}{\Delta t} \quad (2.12)$$

ΔP and ΔU are the variation of pressure and displacement between t and $t + \Delta t$. This equation yields a linear relation between pressure and displacement, which allows the problem to be solved using the solver described in the previous paragraph - in particular, the convolution property remains.

A Zener model only has three material constants, one being its characteristic time. This is not sufficient to accurately model a real-life material such as rubber over a large range of frequencies. It can be generalized by connecting different Zener models in parallel along with a branch with just one spring G_∞ , as shown in Figure 2.1. The displacement

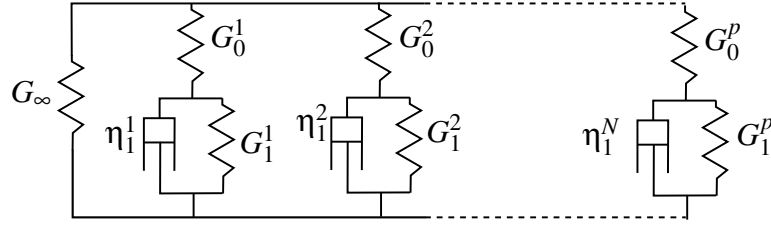


Figure 2.1: Generalized Zener model

in each branch is the same and the pressures in each branch add up. Each branch k follows Equation 2.12. The generalized version of Equation 2.12 is Equation 2.13.

$$U_{t+\Delta t} \left[G_\infty + \sum_k \frac{G_1^k + \frac{\eta_1^k}{\Delta t}}{1 + \frac{G_1^k}{G_0^k} + \frac{\eta_1^k}{G_0^k \Delta t}} \right] = A_{zz} \sum_k P_{t+\Delta t}^k + U_t \sum_k \frac{\frac{\eta_1^k}{\Delta t}}{1 + \frac{G_1^k}{G_0^k} + \frac{\eta_1^k}{G_0^k \Delta t}} \quad (2.13)$$

$$- \sum_k A_{zz} P_t^k \frac{\frac{\eta_1^k}{G_0^k \Delta t}}{1 + \frac{G_1^k}{G_0^k} + \frac{\eta_1^k}{G_0^k \Delta t}}$$

It is then possible to use the 'elastic' Conjugate Gradient contact solver using P' , U'_z and H' instead of P , U_z and H according to Equation 2.14. This yields $U_{t+\Delta t}$ and $\sum_k P_{t+\Delta t}^k$, which is the total pressure acting on the surface.

$$P' = \sum_k P_{t+\Delta t}^k$$

$$U'_z = A_{zz} P'$$

$$H' = H \left[G_\infty + \sum_k \frac{G_1^k + \frac{\eta_1^k}{\Delta t}}{1 + \frac{G_1^k}{G_0^k} + \frac{\eta_1^k}{G_0^k \Delta t}} \right] - U_t \sum_k \frac{\frac{\eta_1^k}{\Delta t}}{1 + \frac{G_1^k}{G_0^k} + \frac{\eta_1^k}{G_0^k \Delta t}} \quad (2.14)$$

$$+ \sum_k A_{zz} P_t^k \frac{\frac{\eta_1^k}{G_0^k \Delta t}}{1 + \frac{G_1^k}{G_0^k} + \frac{\eta_1^k}{G_0^k \Delta t}}$$

It should be highlighted that it is necessary to compute and to store the state variables $A_{zz} P_t^k$ for each branch of the generalized Zener model between each time step using

Equation 2.12. This makes the viscoelastic solver more memory intensive than the elastic one.

2.2 Application: viscoelastic Hertzian contact

2.2.1 Convergence analysis

In order to validate the algorithm developed above, the case of a viscoelastic half-space in contact with a rigid sphere is studied. The material chosen is a one-branch Zener model. For a single branch Zener model, the relaxation function $\psi(t)$ and creep compliance function $\phi(t)$ are:

$$\phi(t) = \frac{1}{G_0} + \frac{1}{G_1} \left(1 - e^{-\frac{t}{\tau'}} \right) \quad (2.15)$$

$$\tau' = \frac{\eta_1}{G_1}$$

$$\psi(t) = \frac{1}{\frac{1}{G_0} + \frac{1}{G_1}} \left(1 + \frac{G_0}{G_1} e^{-\frac{t}{\tau}} \right) \quad (2.16)$$

$$\tau = \frac{\eta_1}{G_0 + G_1}$$

In the following, $G_0 = 1$ MPa, $G_1 = 0.1$ MPa and $\tau' = 1$ s. The sphere radius is 1 mm. A normal load $F_n = 0.02$ mN is applied from $t = 0$.

The analytical solution to this problem can be deduced from Lee and Radok's results [30] using the creep compliance function. The evolution of contact radius with time, for example, is given in Figure 2.2. As expected the contact radius increases with time, quite fast at the beginning then slower and slower as the contact radius converges towards its steady-state value.

Figure 2.3 shows cross-sections of the displacement and pressure at different times as calculated with the current model. For $t \ll \tau$ or $t \gg \tau$, the pressure profile is Hertzian, otherwise during the transient evolution it sometimes shows short pressure spikes at the edge of the contact with an almost constant pressure in the center. These features are due to the material viscoelasticity.

The current viscoelastic model allows to reproduce the same response although the precision of the results is impeded by the time discretization and the spatial discretization.

The time discretization is characterized by the dimensionless time step length $\Delta t^* = \Delta t / \tau'$ and the spatial discretization by the dimensionless length of a mesh cell $l_m^* = l_m / a_{max}$ where l_m is the mesh cell length and a_{max} the contact radius for $t \rightarrow \infty$ as predicted by the analytical model.

To quantify the influence of these parameters the error in contact radius is studied in comparison with the analytically exact solution. The contact radius error is defined by

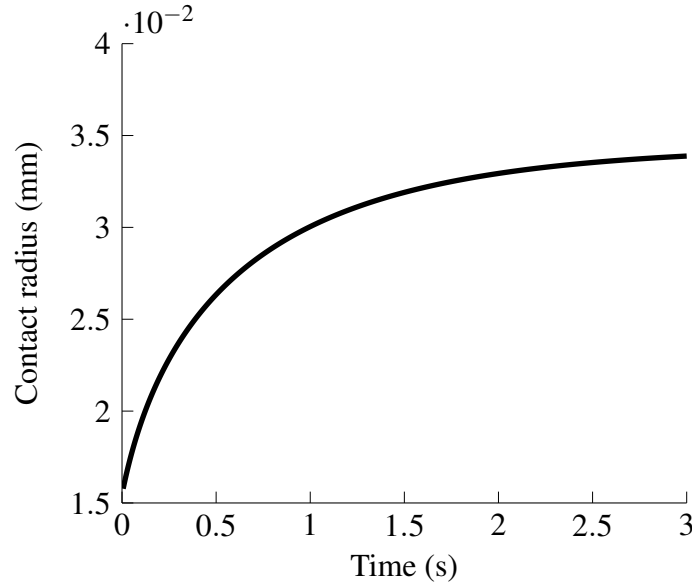


Figure 2.2: Evolution of the contact radius with time for a viscoelastic Hertzian contact with constant normal load. Analytical solution from Lee and Radok [30].

$a_{simulation} - a_{analytical} / a_{analytical}$ where $a_{analytical}$ is the contact radius given by the analytical solution and where $a_{simulation}$ is the contact radius given by the current model. It is calculated from the contact surface area \mathcal{A} : $a_{simulation} = \sqrt{\mathcal{A}/\pi}$.

Figure 2.4 shows the evolution of this error with time, for different time increments. If it is quite evident from paragraph 2.1.3 that the longer the time step, the larger the error, understanding why, for a given time step length, the error is maximum at $t \approx 0.7$ is not as easy. One explanation is that both the long-term ($t \gg \tau'$) and the instantaneous response ($t \ll \tau'$) of the material do not depend on the time step length, so the error is maximum during the transient part between the two extrema.

The lowest curve, corresponding to the smallest time step length, does not exhibit this bell shape and this maximum. The reason is that in this case the error is caused to a great extent by the insufficient mesh discretization: $l_m^* = 0.006$.

A similar study is also performed for different mesh sizes. The results of both time convergence and mesh convergence studies are shown in Figure 2.5. The error values are the average error over the first 3 seconds. The x-axis corresponds to either Δt^* or l_m^* for the time convergence and mesh convergence curves respectively.

The mesh and time convergence speeds are: $error \propto (l_m^*)^{1.3} \propto (\Delta t^*)^{1.1}$. The lowest point of the time convergence curve deviates significantly from the rest of the curve which is another sign of the error being caused by the mesh discretization rather than the time discretization for this point.

Interestingly, a lower bound of the mesh error can be estimated using the results of *Gauss's circle problem* [69]. This problem is to find the number of lattice points \mathcal{N} laying inside a circle of a given radius a . The answer is given in Equation 2.17 for a lattice spacing of 1.

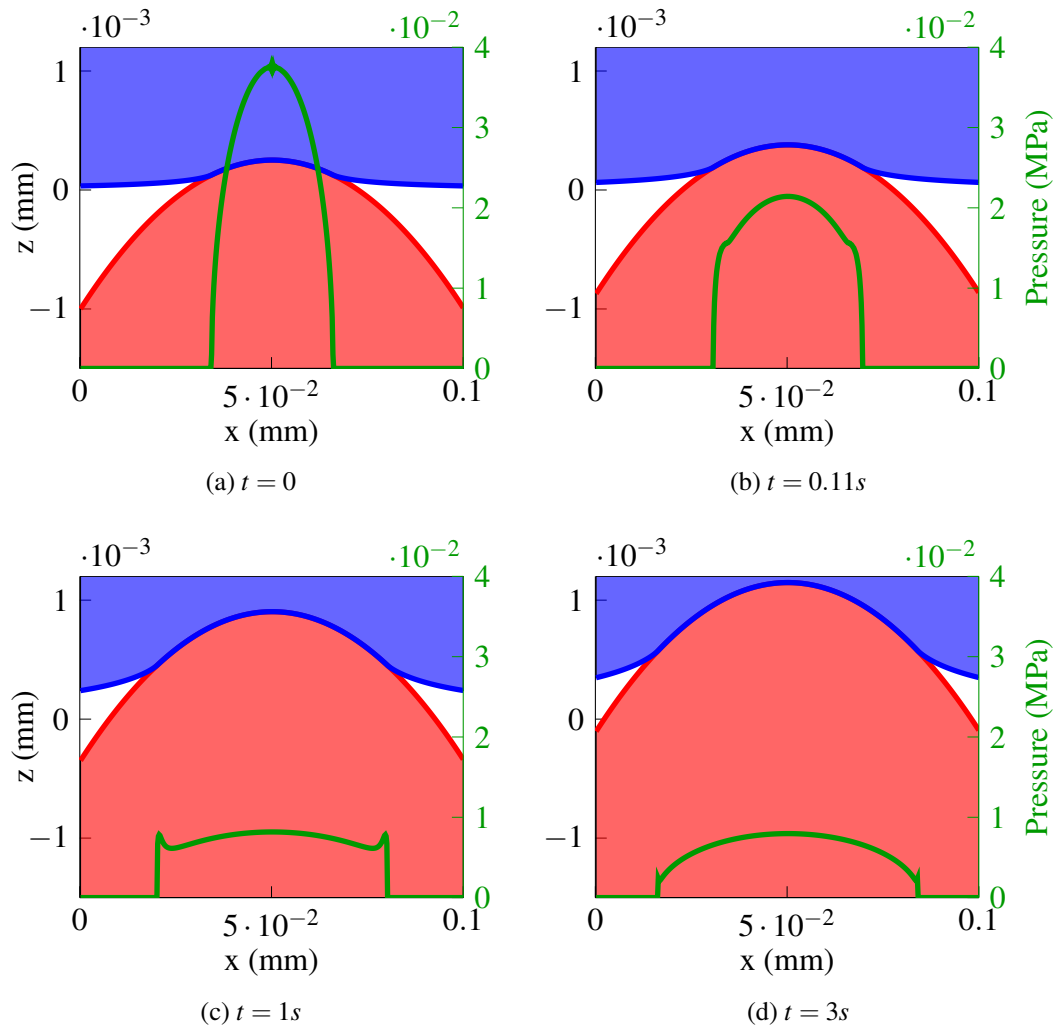


Figure 2.3: Pressure and displacement profiles for a viscoelastic hertzian contact at different times.

$$\mathcal{N}(a) = 1 + 4[r] + 4 \sum_{i=1}^{\lfloor a \rfloor} \lfloor \sqrt{a^2 - i^2} \rfloor \quad (2.17)$$

The $\lfloor \rfloor$ signs stand for the floor function. In the current model, the contact radius is deduced from the contact area $\mathcal{A} = l_m^2 \mathcal{N}_{contact}$ where $\mathcal{N}_{contact}$ is the number of points in contact in the simulation. For a given contact radius a_{ref} , Equation 2.17 can be used to find an estimation of the number of points laying inside the disc N_{Gauss} , which is similar to $\mathcal{N}_{contact}$. As $l_m^2 \mathcal{N}_{Gauss} \neq \pi a_{ref}^2$, the difference can be used as an estimation of contact area error caused by the mesh discretization, which in turns gives an estimation of the contact radius error. This error is shown in the ‘Theoretical mesh error’ curve in Figure 2.5. It is a lower bound of the simulation error as it is purely geometrical and does not

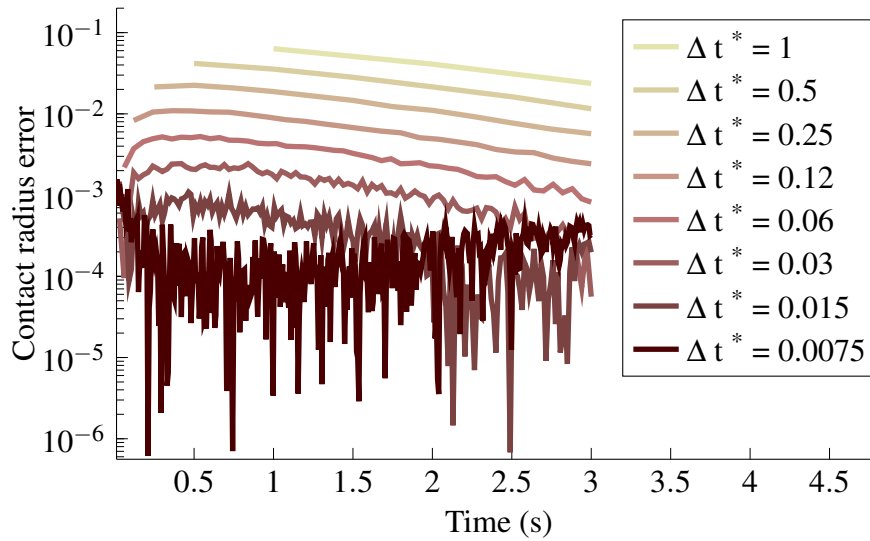


Figure 2.4: Temporal evolution of the error in contact radius prediction for different time increments.

account for the error caused by the poor discretization of the pressure field for example.

2.2.2 Viscoelastic losses in a sliding contact

So far only a normal force has been applied to the viscoelastic half space. In tire application however, the rubber block slides upon the road which causes viscoelastic losses. Predicting these losses is of primary importance as they play a significant role in tire friction. Using Persson's analytical model [3] and comparing his results to experimental data, Lorenz [59] estimated that viscoelastic losses could represent more than half of the friction losses during sliding, depending on the sliding speed.

To implement sliding in the current model, the rigid surface is translated uniformly by a quantity Δx between each time step, so that $V_x = \Delta x / \Delta t$ where Δt is the length of the time step and V_x the required sliding speed. The best choice for Δt is such that $\Delta x = l_m$: in this case the coordinates of the rigid surface just need to be translated by one mesh cell at each time step. Otherwise, it is necessary to interpolate the surface which is time consuming and may reduce precision: interpolation is likely to smooth the surface. It may be necessary in some cases to ensure that the time step is small compared to the characteristic time of the material.

When a sphere slides on a viscoelastic half-space, the contact is not symmetrical anymore. The pressure becomes higher at the leading edge of the contact, sometimes showing a sharp pressure spike at the contact entrance. The pressure at the trailing edge of the contact is lower and the contact surface is shifted to the front of the sphere. These phenomena were studied in [13] for transient sliding and in [18] in steady-state sliding using the same parameters. Their results are reproduced using the current model, showing good agreement.

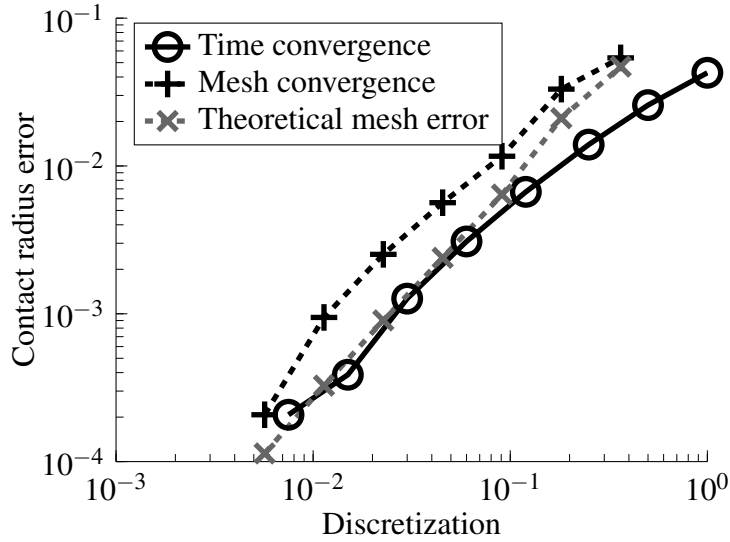


Figure 2.5: Mean error in contact radius. The ‘mesh convergence’ curve is the error as a function of the dimensionless mesh cell length for the smallest time step length, while the ‘Time convergence’ curve is the error as a function of the dimensionless time step length for the smallest mesh cell length. The ‘Theoretical mesh error’ is the minimum mesh error possible.

The material is a one branch Zener model with $G_0 = 2.75$ MPa, $G_0/G_1 = 9$ and $\tau' = \eta_1/G_1 = 0.01$. The radius of the sphere is 10 mm. The speed and pressure are normalized using the Hertzian contact parameters with the instantaneous elastic shear modulus G_0 . The contact radius is a^* and the mean pressure in the contact area p_0 . The normalized time and speed are $t^* = t/\tau'$ and $V^* = V\tau'/a^*$.

The mesh used for the current model is a non-periodic (zero-padded) 1024×1024 regular mesh and the domain length is $L = 10$ mm $\approx 21a^*$. Figure 2.6 clearly shows the pressure difference between the leading and trailing edge of the contact: small, sharp pressure spikes at the leading edge at low speed, which get larger and higher as the speed increases.

Figure 2.7 shows the evolution of the steady-state apparent friction coefficient with velocity as calculated with a 512×512 mesh with $L = 12$ mm with a comparison to the results of Carbone [18].

The apparent friction coefficient μ is defined as the absolute value of the tangential force divided by the normal force. The tangential force F_t is computed from Equation 2.18 where S_c is the contact surface and H the height map of the rigid substrate - in the present case the sphere.

$$F_t = \int_{S_c} P \frac{\partial U_z}{\partial t} dS / V = \int_{S_c} P \frac{\partial H}{\partial x} dS \quad (2.18)$$

The steady state friction coefficient is approximated from the transient computation by averaging the value of the friction coefficient during the last part of sliding, once it

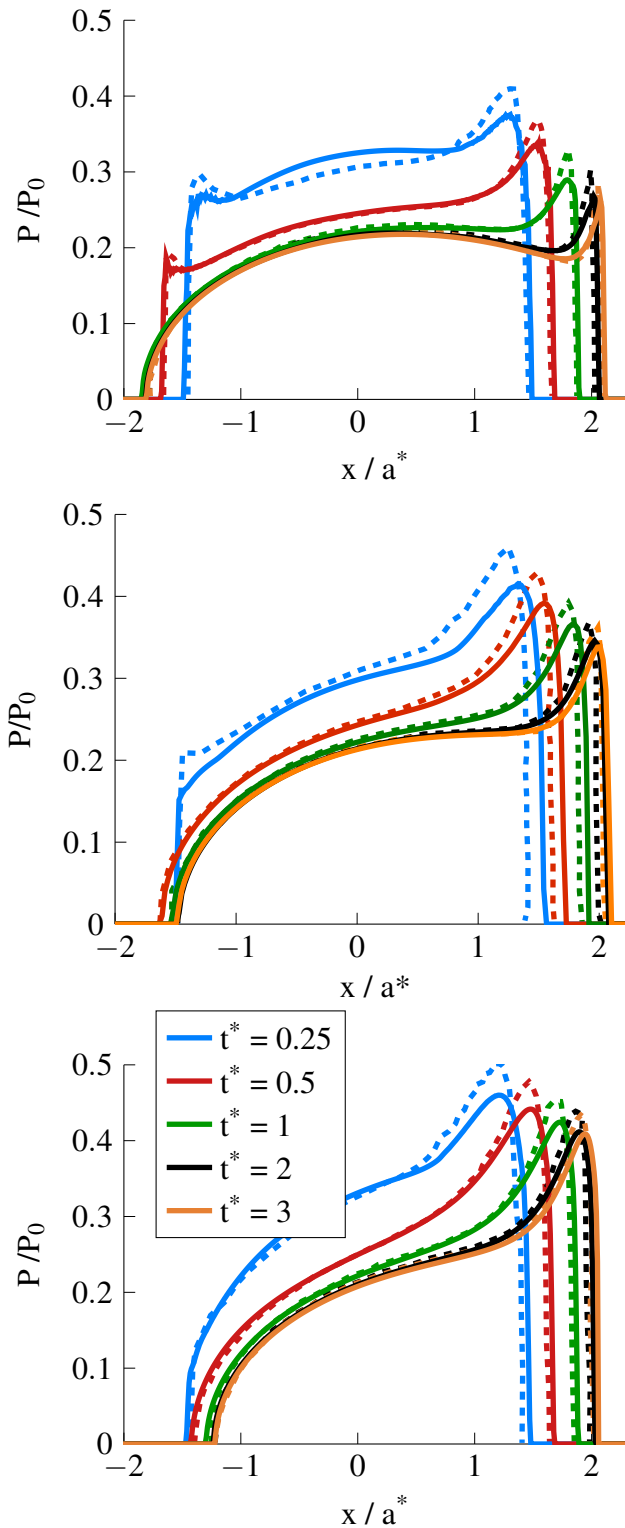


Figure 2.6: Normalized contact pressure profile along the sliding direction, for a dimensionless velocity of 0.4, 0.8 and 1.2 top to bottom. Solid lines are for the current model, dashed lines are from [13]. $x = 0$ is the center of the sphere.

has reached an almost constant value. Figure 2.7 shows a friction curve with a bell shape: friction is maximum at intermediate speeds and tends to zero at infinitely low or high speeds. This curve is typical of rubber friction: at low speed, rubber behaves like a soft elastic solid while at high speed it behaves like a hard elastic solid. In both cases, it does not dissipate energy as it slides. At intermediate speeds (which corresponds to intermediate frequencies), viscoelasticity has a strong effect which causes energy losses and consequently friction.

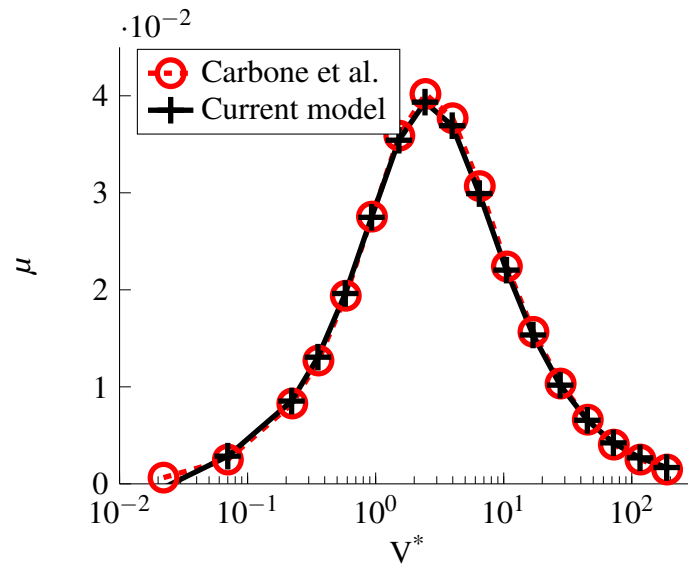


Figure 2.7: Variation of the apparent steady-state friction coefficient with velocity compared to numerical results from Carbone et al. [18].

Another parameter is of primary importance for transient sliding: the time $T_0 = T_0^* \tau'$ between the moment when the normal load is applied and the moment when sliding starts. During this period, the normal displacement increases because of viscoelasticity. If it is small ($T_0^* \ll 1/V^*$ and $T_0^* \ll 1$), the normal displacement will continue to increase during sliding causing friction to increase slowly as the amplitude of the deformation increases. If it is large ($T_0^* \gg 1/V^*$ and $T_0^* \gg 1$) the normal displacement will reach a higher value than in steady-state sliding. Consequently, sliding decreases the normal displacement which causes an increase of the potential energy of the normal force. As sliding is at constant speed, this extra energy is provided by a temporary increase in tangential force which in some cases causes the friction curve to have a maximum μ_{max} before reaching its steady state value μ_{dyn} , as shown in Figure 2.8.

The maximum μ_{max} depends also on the sliding speed: the higher the sliding speed, the higher the μ_{max} , because at higher sliding speeds the normal displacement is lower. At higher speeds the maximum also appears after a shorter loading time, as shown in Figure 2.9. On this figure the ratio μ_{max}/μ_{dyn} is presented as it is more appropriate to compare the results for different sliding speeds.

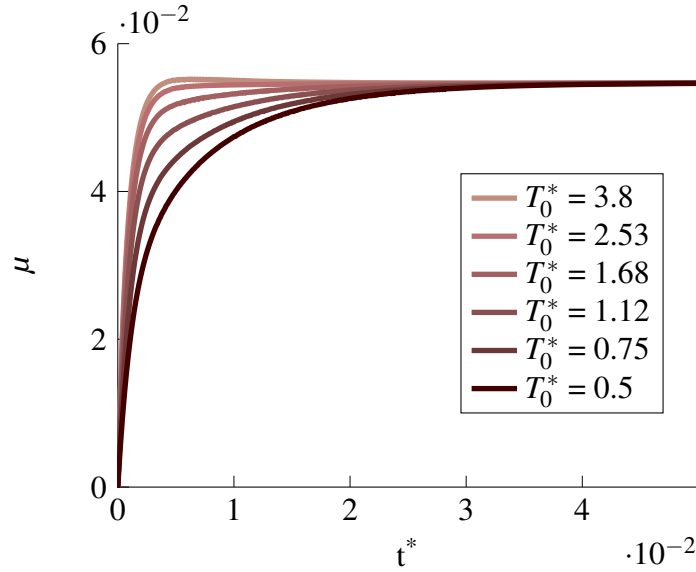


Figure 2.8: Friction curves for different loading times T_0^* for $V^* = 0.8$

2.3 Adhesion

2.3.1 Adhesion model

Adhesive forces as described in paragraph 1.2.2 are tensile forces developing between two surfaces. In the general case, one geometric point of a surface attracts all the points of the other surface with a force depending on the distance between them. For a surface of a half-space discretized into N^2 points, computing the adhesive forces acting on each point requires $O(N^4)$ operations. As these forces depend on the geometry of the rigid substrate and on the deformation of the half-space, these operations cannot be simplified with a convolution product. In addition to this, the direction of the adhesive force acting on one point is not necessarily vertical. As the surfaces are nominally flat and the slopes are small, the common way to model adhesion in both analytical and numerical studies is to consider that the magnitude of the force depends only on the local gap and its direction is always vertical as illustrated in Figure 2.10 (this hypothesis is used for example in [40] or [67]).

Using this assumption, the potential adhesive energy between two surfaces is defined by Equation 2.19, where $g(X) = U_z(X) - H(X)$ is the local gap and S is the surface of the half-space.

$$E_{adh} = \iint_S e_{adh}(g(X)) \quad (2.19)$$

e_{adh} is the local adhesive potential. The local adhesive pressure deriving from this potential is $P_{adh} = -\frac{\partial e_{adh}(g)}{\partial g}$. In most cases the precise shape of this potential is unknown. What can be measured on the other hand is the adhesive energy γ_0 which is required

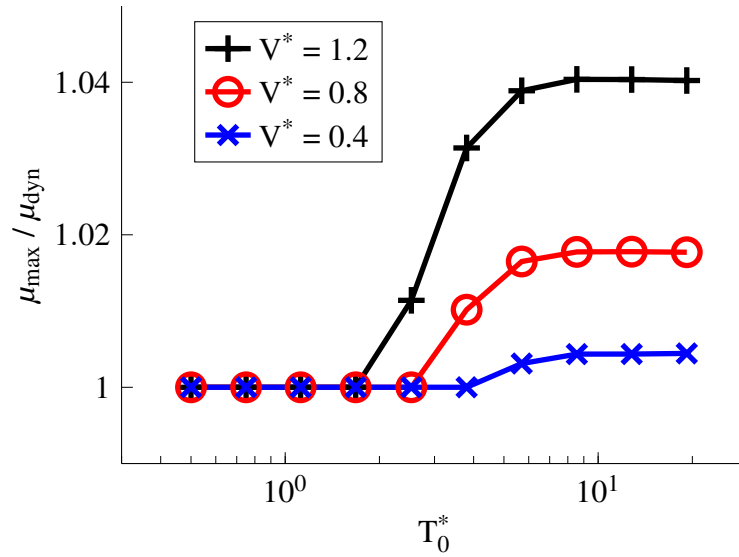


Figure 2.9: Evolution of the maximum friction ratio μ_{max}/μ_{dyn} with the loading time at different sliding speeds.

to separate two surfaces in contact. Another important parameter is an estimation of the range of the interactions z_0 . A number of different potentials can be built from these two parameters. A few are given in Equation 2.20.

$$e_{adh} = -\gamma_0 \begin{cases} \exp\left(-\frac{g}{z_0}\right) & \text{Exponential [67]} \\ \exp\left(-\frac{g^2}{z_0^2}\right) & \text{Gauss [67]} \\ \left(1 - \frac{g}{z_0}\right)\Theta(z_0 - g) & \text{Maugis-Dugdale [40]} \end{cases} \quad (2.20)$$

where Θ is the Heaviside step function.

In the present case the exponential potential is chosen because it is shown in [67] that it gives similar results to Maugis-Dugdale's model, but with the advantage of being continuous. The adhesive pressure is given by Equation 2.21. The minimum adhesive pressure is reached when the gap is zero and is $-\frac{\gamma_0}{z_0}$.

$$P_{adh} = -\frac{\gamma_0}{z_0} \exp\left(-\frac{g}{z_0}\right) \quad (2.21)$$

The contact problem is not the same: Equation 2.1 turns into Equation 2.22:

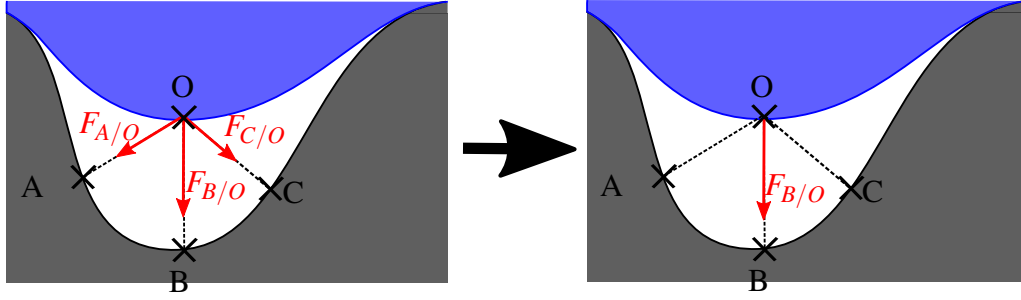


Figure 2.10: The adhesive force acting on one point (O) is supposed to be the sum of the interactions between O and all the points of the counter surface (left figure). The simplifying assumption used here is to consider that this force is vertical and only depends on the local gap (right figure).

$$\begin{aligned}
 P(X) &\geq -\frac{\gamma_0}{z_0} && \forall X \\
 g(X) &\geq 0 \\
 g(X) &= 0 && X \in S_c \\
 P(X) &= -\frac{\gamma_0}{z_0} \exp\left(-\frac{g(X)}{z_0}\right) && X \in \neg S_c
 \end{aligned} \tag{2.22}$$

2.3.2 Implementation

Implementing adhesion in the algorithm described in 2.1.2 can be done in a rather simple way. The first step is to change the definition of the contact surface by allowing negative pressures in it (as long as $P(i, j) \geq -\frac{\gamma_0}{z_0}$, the point (i, j) can remain in the contact surface). Despite adhesion, the search direction remains 0 outside of the contact surface: the adhesive pressure outside of the contact surface is computed from the local gap at each iteration, after the computation of the residual. A problem arises: to compute the residual, the adhesive pressure is required, but this adhesive pressure depends on the residual! A first solution is to make an inner loop: compute the residual, the corresponding adhesive pressure, compute the residual again with this new pressure... This proves quite slow. Another solution is to consider that as the algorithm converges, the gap difference from one iteration to another is small compared to the characteristic length z_0 .

In both cases, the algorithm proves to be quite unstable, especially for short range adhesion on rough surfaces.

A more suitable approach to solve the adhesive contact problem is to try to find the displacement U_z solution to the problem instead of trying to find the pressure. This way, the computation of the residual is exact. This is the solution chosen in [23] in which an algorithm very similar to the one presented here is developed. It should be mentioned that both were developed independently. The algorithm is also similar to the one explained in paragraph 2.1.2: it is a Conjugate Gradient loop, starting from an initial guess of gap g_0

and converging towards the right solution.

The first difference is the functional to be minimized. Here it is given by Equation 2.23:

$$\mathcal{F} = -E_{adh}/l_m^2 - E_{elas}/l_m^2 = \gamma_0 \sum_{(i,j)} \exp\left(-\frac{g}{z_0}\right) - \frac{1}{2}(H+g)^T \cdot A_{zz}^{-1} \cdot (H+g) \quad (2.23)$$

l_m^2 is the mesh cell length and g is the local gap which is always 0 in the contact surface, so that:

$$\frac{\partial \mathcal{F}}{\partial g} = r = \begin{cases} -\frac{\gamma_0}{z_0} \exp\left(-\frac{g}{z_0}\right) - A_{zz}^{-1} \cdot (H+g) & \text{if } (i,j) \in \neg S_c \\ 0 & \text{if } (i,j) \in S_c \end{cases} \quad (2.24)$$

In theory the mean term of \widehat{A}_{zz}^{-1} is infinite for a periodic contact: a non-zero mean displacement yields an infinite mean pressure. That is why the mean displacements and pressure are treated separately and the mean term is set to 0 to avoid computational problems. In all cases, the mean displacement needs to be zero, which implies $A_{zz}^{-1}(H+g) = 0$. If the mean pressure P^m is imposed as boundary condition, the real pressure field is simply deduced from the displacement field as $P = P^m + A_{zz}^{-1}(H+g)$, which makes the pressure correction scheme used in paragraph 2.1.2 unnecessary. Accordingly, Equation 2.24 is replaced by Equation 2.25.

$$\frac{\partial \mathcal{F}}{\partial g} = r = \begin{cases} -\frac{\gamma_0}{z_0} \exp\left(-\frac{g}{z_0}\right) - A_{zz}^{-1} \cdot (H+g) - P^m & \text{if } (i,j) \in \neg S_c \\ 0 & \text{if } (i,j) \in S_c \end{cases} \quad (2.25)$$

At the end of iteration n , the gap field is g_n , the residual is r_n in $\neg S_c$ ($r_n = 0$ in the contact zone) and the search direction is d_n .

The first step of iteration $n+1$ is to find $g_{n+1} = g_n + \alpha d_n$. α is a scalar chosen to minimize \mathcal{F} along the search direction. The simplest way to find α is to use Equation 2.6, replacing A_{zz} by A_{zz}^{-1} . But this α only minimizes \mathcal{F} if the adhesive forces do not change between two iterations, which is only approximately true when the algorithm is close to convergence - in other words this equation only works in linear conjugate gradient. Instead, finding α such that $\partial \mathcal{F} / \partial \alpha = 0$ after linearizing P_{adh} yields:

$$\alpha = \frac{d_n^T \cdot r_n}{d_n^T \cdot A_{zz}^{-1} \cdot d_n - d_n^T \cdot \frac{\partial P_{adh}}{\partial g}(g_n) \cdot d_n} \quad (2.26)$$

The matrix $\partial P_{adh} / \partial g$ is diagonal and with an exponential adhesion potential:

$$d_n^T \cdot \frac{\partial P_{adh}}{\partial g}(g_n) \cdot d_n = - \sum_{i,j} d_n^2(i,j) \frac{P_{adh}(i,j)}{z_0} \quad (2.27)$$

As the adhesive pressure P_{adh} is already in memory (it was computed during the computation of the residual), the extra computational time and memory required to compute α compared to the linear version is small.

g_{n+1} is computed and all the points where the new gap is negative are added to the contact surface and their gap is set to 0. The new residual r_{n+1} is computed using Equation 2.25. The points of the contact surface with a pressure inferior to $-\gamma_0/z_0$ are removed from the contact surface.

The new search direction d_{n+1} is computed from the new residual. In linear conjugate gradient d_{n+1} is computed in order to be A_{zz}^{-1} – orthogonal to d_n , but a slightly better solution can be found. After a first order expansion, the residual is $r(g + \varepsilon) \approx r(g) - (A_{zz}^{-1} - \partial P_{adh}/\partial g(g)) \cdot \varepsilon$ instead of $r(g + \varepsilon) = r(g) - A_{zz}^{-1}(g) \cdot \varepsilon$. The linearized local matrix $B = A_{zz}^{-1} - \partial P_{adh}/\partial g(g)$ plays a more important role than A_{zz} locally, that is why it is chosen to set the new search direction to be B – orthogonal to the previous one. Consequently, the new search direction is $d_{n+1} = r_{n+1} + \beta d_n$ where:

$$\beta = - \frac{r_{n+1}^T \cdot A_{zz}^{-1} \cdot d_n - r_{n+1}^T \cdot \frac{\partial P_{adh}}{\partial g} \cdot d_n}{d_n^T \cdot A_{zz}^{-1} \cdot d_n - d_n^T \cdot \frac{\partial P_{adh}}{\partial g} \cdot d_n} \quad (2.28)$$

This non linear algorithm converges in theory faster than the linear one. It needs $\approx 10\%$ less iterations to achieve convergence, depending on the problem. However, the extra computational cost caused by the more complex formulas for α and β counter-balance the gain, so that the total time required to perform a computation remains approximately the same. The values of α are necessarily larger than with the linear algorithm which makes the algorithm a bit less stable, in particular the determination of the contact area may take more iterations. A convergence study of the different algorithms is performed in [70].

2.3.3 Validation: viscoelastic Hertzian contact with adhesion

As mentioned in paragraph 1.2.2 and 1.2.3 the case of a rigid sphere in contact with a viscoelastic half-space with adhesive forces is of practical importance and its full resolution was obtained by Haiat [49]. A simplified solution is given in [31]. In this last publication an example is given for a loading/unloading cycle with prescribed normal displacement. This example is reproduced here using the current model.

In the adhesive algorithm previously described the normal load is prescribed. It can be adapted for a prescribed normal displacement Δz instead using the same scheme as the algorithm without adhesion, the roles of normal displacement and normal load being reversed: in the latter the normal load is corrected at each iteration to match the prescribed normal load, here the gap is corrected at each iteration to match the prescribed mean normal displacement - details of this implementation can be found in [70].

The comparison between the analytical result [31] and the current model shows a good agreement, which validates the coupling between the contact solver with adhesion

and the transient viscoelastic scheme. On the load/displacement curve 2.11 a small discrepancy can be seen at the end of the unloading. It can be explained by the fact that Barthel, following the work of Greenwood [71], uses a double-Hertz adhesive potential which cannot be easily implemented numerically. The current model uses an exponential adhesive potential with a matching adhesion energy and interaction length.

These curves also highlight the fact that, despite being conservative forces, adhesive forces cause energy losses as they couple with viscoelasticity. The adhesion-less curve shows a much smaller hysteresis than the curve with adhesion. It should also be kept in mind that after the unloading, at $\Delta z = 0$, the contact surface is still non-zero in the adhesive case, which means adhesion is not yet fully released and the losses are higher than the area inside the curve suggests.

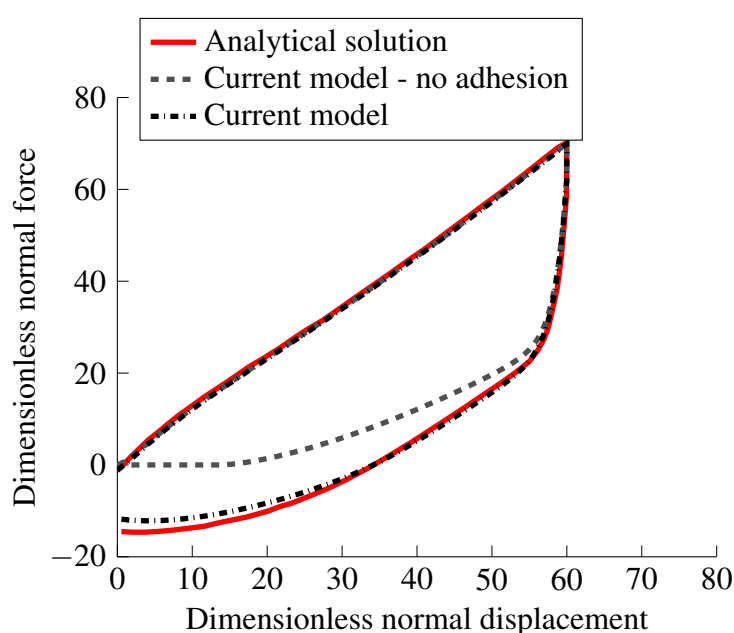


Figure 2.11: Load/displacement curves for a viscoelastic Hertzian contact with and without adhesion. The normal displacement is imposed with a constant speed during loading and a two times slower speed during unloading. The analytical solution is from Barthel [31], where the precise parameters of this experiment can also be found.

2. Numerical model for frictionless contacts and application to Hertzian contacts

Chapter 3

Contacts with friction

The numerical model is extended to handle sliding contacts with friction. First different friction laws are discussed. The implementation of friction in the code is then detailed. A number of numerical problems arising from viscoelastic contacts with friction are treated. Examples are given for Hertzian contacts.

3.1 Friction laws

3.1.1 Friction forces in a contact problem

The algorithm presented in Chapter 2 only solves the contact problem in the normal direction, as if there were no friction at all. This simplification makes it difficult to accurately model real-life contacts where several phenomena cause friction. As detailed in paragraph 1.1.2, at macro scale experimental data suggests that when a solid is sliding, it opposes a tangential force proportional to the normal force: this is the Coulomb friction law. The phenomena occurring at micro scales (van der Waals bonds, physisorption...) on the other hand are more likely to cause a friction force proportional to the contact surface - a fact that is supported by experimental data for smooth contacts. This is the 'constant shear stress' friction law. At last, viscoelastic losses in the bulk of a rubber material also result in a friction force.

The necessity to take friction into account in the computation is arguable: for an incompressible half-space sliding on a rigid surface (which is a good representation of rubber sliding on a road at meso-scale), there is no coupling between the normal displacements and the tangential displacements. Consequently the simplest way to account for friction would be to use the previous algorithm to quantify the viscoelastic losses and the contact surface of the sliding contact and then to apply the appropriate friction law to compute the total friction force.

Though this approach works well for a steady-state elastic contact, as long as the precise knowledge of the tangential displacement field is not required, it is not sufficient for a transient viscoelastic contact. During the transient part of sliding, the contact area is divided in a slipping part and a sticking part. This separation plays an important role in the evolution of the tangential force as a function of the lateral displacement. As sliding does not occur at the same time at every point, it also influences the viscoelastic response of the material. In other words, there is an indirect coupling between the tangential and normal displacements in the present case caused by the transient aspect of sliding and the material viscoelasticity.

Handling this coupling directly, that is to say solving the normal contact and tangential sliding in the same conjugate gradient loop is quite tricky. Instead it is chosen to separate the normal and tangential contact problems and to follow a step by step approach in the same way as for the implementation of the transient viscoelasticity (see paragraph 2.1.3).

The overview of the algorithm is as follows:

Initialization

- Computation of normal pressure and displacement

Beginning of the time step loop

- Computation of the tangential displacement
- Interpolation of the half space according to the local slip
- Computation of the normal pressure and displacement

End of the loop

Using this scheme, the normal and tangential problems are solved separately, which makes the algorithm much simpler but may induce an error if the time steps are too big. This separation of the two problems remains a valid hypothesis as long as the difference of the normal pressure field between two steps remains small. It is true if the two following conditions are met:

- The length of the time step is small compared to the characteristic time of the viscoelastic material.
- The tangential slip during a step is small compared to the characteristic size of the problem.

The first condition is the same as the condition described in paragraph 2.1.3 for a contact without friction.

3.1.2 Coulomb friction and “constant shear stress” friction

In the following section, P denotes the normal pressure and (T_x, T_y) the shear stress at the surface of the half-space in the x and y directions. As the tangential and normal directions are decoupled, it is supposed that the contact surface S_c is already known. This contact surface is then separated into two zones: the ‘sticking’ contact surface S_{stick} where no relative displacement between the half-space occurs and the substrate and the ‘slipping’ contact surface S_{slip} where there is. These two should be calculated by the tangential contact algorithm: if the norm of the shear stress $\|T\| = \sqrt{T_x^2 + T_y^2}$ is strictly below a limit T_{max} , the point is in the stick zone, otherwise the point is in the slip zone and the norm of the shear stress is prescribed by T_{max} and the direction of the shear stress should be the same as the direction of slip. These conditions are summed-up by Equation 3.1, where the relative displacement between the two surfaces is $r = (r_x, r_y)$ and (i, j) is the point under consideration.

$$\begin{aligned} \|T\| &\leq T_{max} \\ r &= 0 \end{aligned} \quad (i, j) \in S_{stick} \tag{3.1}$$

$$\begin{aligned} \|T\| &= T_{max} \\ r/\|r\| &= T/\|T\| \end{aligned} \quad (i, j) \in S_{slip}$$

T_{max} depends on the friction law considered. For a Coulomb friction law, it depends linearly on the normal pressure through a coefficient μ which is close to 1 in rubber/ road applications: $T_{max} = \mu P$. Otherwise for a ‘Constant shear stress’ friction law it is simply a constant independent from the pressure $T_{max} = \sigma_{max}$. For this last law, the shear stress is not continuous at the edge of a contact patch. To avoid this discontinuity, a ‘mixed’ friction law can be used. At low pressure, it is a Coulomb friction law and at high pressure the shear stress is constant: $T_{max} = \min(\mu P, \sigma_{max})$. This law is also known as Coulomb-Orowan friction.

The condition that the direction of the shear stress should be the same as the direction of slip ($r/\|r\| = T/\|T\|$) is equivalent to T minimizing the friction losses, by minimizing the sliding distance. That is because r is an affine function of T : $r = A + BT$ where B is

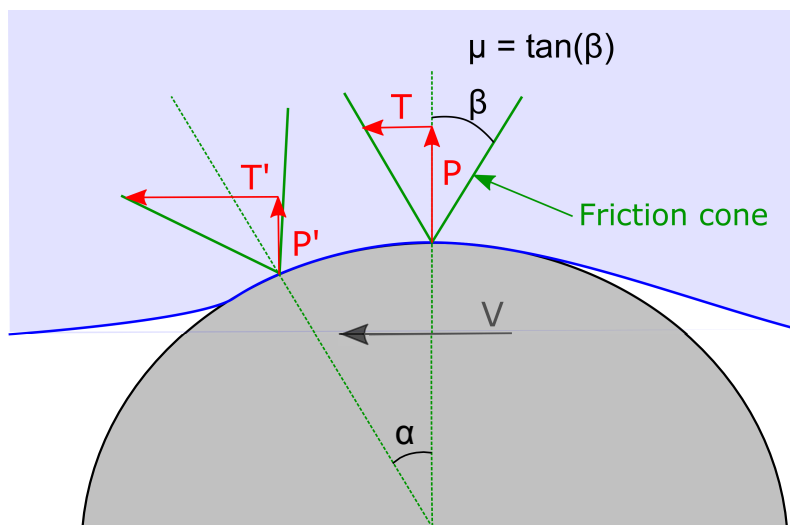


Figure 3.1: Illustration of the slope effect in a Hertzian contact. The sphere is sliding to the left over a viscoelastic half space. The friction cone is tilted at the leading edge of the contact, leading to an increase in friction compared to the trailing edge.

positive and A is the displacement caused by the traction field in the other points than the one under consideration.

3.1.3 Effect of the local slope

In the previous paragraph the friction laws are written in terms of P and T which are the surface stresses in the vertical and horizontal directions. They are consequently strictly valid only for a flat contact: in the general case, they should be expressed in terms of normal stress and tangential stress, using the local normal to the surface instead of the general vertical and horizontal axes. This effect is illustrated in Figure 3.1: for a Coulomb friction law, the admissible stresses lie inside a cone. This cone is tilted depending on its position on the sphere, which means that there is slightly more friction at the leading edge of a sliding contact than at the trailing edge.

Though the current model makes use of the “small slope approximation”, this effect cannot be overlooked altogether, as it is a first order effect. If at a given position the normal to the surface makes an angle θ with the vertical axis in the x direction and considering that T_x is still in the horizontal direction, its maximum value is then given by Equation 3.2.

$$T_{max}^{slope} = P \frac{\mu + \tan(\theta)}{1 - \mu \tan(\theta)} \approx P(\mu + \tan(\theta) + \mu^2 \tan(\theta)) \quad (3.2)$$

For a friction coefficient of $\mu = 1.5$ and a local slope of only 6° , which corresponds to a shear strain of 10 %, the error made by not considering this slope is close to 20 %.

Taking the slope into account is equivalent to saying that, locally, $\|\sigma_t\| = \mu \sigma_n$, where σ_n is the stress in the direction of the normal to the surface and σ_t the stress perpendicular

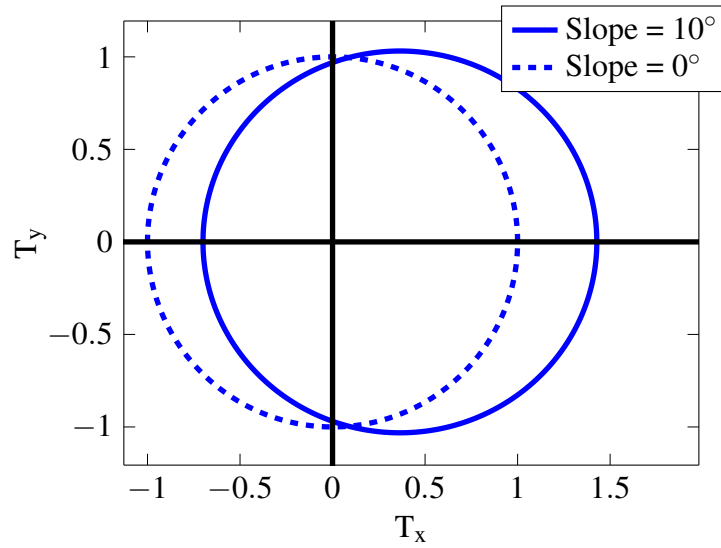


Figure 3.2: Traction boundary with or without slope, with $P = 1$ and $\mu = 1$. The slope is in the x direction.

to this normal. If the surface is H then we define (N_x, N_y, N_z) so that:

$$\nabla H = \begin{cases} N_x \|\nabla H\| \\ N_y \|\nabla H\| \\ N_z \|\nabla H\| \end{cases} \quad (3.3)$$

The vector (N_x, N_y, N_z) is a unitary vector which is normal to the surface and which is expressed in the global coordinates, that is to say z is in the vertical direction and (x, y) in the horizontal directions. Stating that $\|\sigma_t\| = \mu \sigma_n$ and using the variables (T_x, T_y, P) in the global coordinates leads to Equation 3.4

$$\begin{aligned} & T_x^2(1 - N_x^2(1 + \mu^2)) + T_y^2(1 - N_y^2(1 + \mu^2)) \\ & + P^2(1 - N_z^2(1 + \mu^2)) - 2T_x T_y N_x N_y (1 + \mu^2) \\ & - 2T_x P N_x N_z (1 + \mu^2) - 2T_y P N_y N_z (1 + \mu^2) = 0 \end{aligned} \quad (3.4)$$

This is the equation of an ellipse, which is expected as it corresponds to the intersection between a tilted cone and a plane. An illustration of the difference of traction boundary with or without slope is found in Figure 3.2. It highlights the fact that the traction boundary is no longer independent of the sliding direction.

In the same way that the traction boundary T_{max} is modified in Equation 3.1, the condition on the sliding direction $r/\|r\| = T/\|T\|$ is also changed, but remains equivalent to T being in the direction that minimizes the sliding losses and consequently the sliding distance.

Equations for friction laws with slope for a ‘‘Constant shear stress’’ friction law and for a Coulomb friction law with adhesive forces are found in Appendix B.

3.2 BEM with friction

3.2.1 Tangential problem functional

In order to implement friction in a Boundary Element code, the problem is discretized in the same way as in Chapter 2. Rubber is considered to be incompressible and the substrate to be rigid, so the problem is ‘quasi-identical’ and the tangential and normal displacements are decoupled. The relation between displacement and traction/pressure is given in Equation 3.5

$$\begin{aligned} U_x &= A_{xx}T_x + A_{xy}T_y \\ U_y &= A_{xy}T_x + A_{yy}T_y \\ U_z &= A_{zz}P \end{aligned} \quad (3.5)$$

The $A_{...}$ Influence Coefficient matrices are all convolution matrices, so that all the matrix multiplications can be done efficiently in Fourier space. They are described in Kalke’s book [9] for the non-periodic case. For the periodic case they can be deduced using integral transforms, as described in unpublished work by P.Sainsot given here in Appendix A. Special attention is required concerning the mean displacement. For a semi-infinite half-space, the mean displacement should be zero, which is equivalent to $\bar{A}_{xx} = \bar{A}_{yy} = 0$. In most real-life situations, the half-space is considered to be semi-infinite because it is thick and large compared to the size of the contact problem, but it has a finite thickness. As the thickness increases, for a given mean tangential force, the mean displacement actually increases. Accounting for this effect can be done by changing the mean term of the influence coefficient matrices into $\bar{A}_{xx} = \bar{A}_{yy} = h/G$, where h is the thickness of the half-space and G the shear modulus of the material.

The best way to compute the displacement in Fourier space is to use Equation 3.6, which is equivalent to performing two matrix multiplications instead of four by using in an advantageous way the complex nature of the Fourier transform. ι is the imaginary number.

$$\begin{aligned} U_x &= \text{real} \left(\text{FFT}^{-1} \left(\text{FFT}(A_{xx} + \iota A_{xy}) \text{FFT}(T_x - \iota T_y) \right) \right) \\ U_y &= \text{real} \left(\text{FFT}^{-1} \left(\text{FFT}(A_{yy} + \iota A_{xy}) \text{FFT}(T_y - \iota T_x) \right) \right) \end{aligned} \quad (3.6)$$

A conjugate gradient iterative method was chosen to solve the problem, as in chapter 2. The algorithm iterates on the tangential traction fields $T = (T_x, T_y)$ to find the lateral displacements satisfying the friction law (Equation 3.1).

The functional to minimize is given in Equation 3.7:

$$\mathcal{F}_{tan} = \frac{1}{2} T^T . A_T . T - D X^T . T \quad (3.7)$$

where:

$$U_T = \begin{pmatrix} U_x \\ U_y \end{pmatrix}, \quad T = \begin{pmatrix} T_x \\ T_y \end{pmatrix}, \quad A_T = \begin{pmatrix} A_{xx} & A_{xy} \\ A_{xy} & A_{yy} \end{pmatrix} \quad (3.8)$$

DX is the imposed lateral displacement. Kalker [9] proved that minimizing this functional under the assumption $\|T\| \leq T_{max}(P)$ gives the solution to the tangential contact problem: in particular, once this functional is minimized the direction of slip is the same as the direction of the tangential traction, so this boundary condition does not need to be explicitly enforced in the conjugate gradient loop. This theorem is valid for a Coulomb friction law, for a constant shear stress friction law and for a ‘mixed’ friction law.

This theorem unfortunately does not apply to the friction law with slope, as one of the hypothesis is that T_{max} does not depend on the slip or the direction of the traction. In this case, the existence and unicity of the solution is therefore not guaranteed, nor is the direction of sliding. For reasonable slopes, it should nonetheless not be a problem.

3.2.2 Enforcement of the friction law

The conjugate gradient loop described below gives at each iteration a new guess for the tangential traction fields, until the functional is minimized. But the conjugate gradient procedure by itself does not guarantee that the traction field satisfies the condition on the traction boundary $\|T\| \leq T_{max}(P, T/\|T\|)$. (The notation $T_{max}(P, T/\|T\|)$ means the traction boundary can depend on the direction and on the pressure in order to be representative of all the friction laws described above, with or without slope.) Consequently at each iteration the traction field should be adapted in order to respect this condition. This is achieved using Equation 3.9.

$$T \rightarrow T_{rec} = \begin{cases} T & \text{if } T \in S_{stick} \\ k * T & \text{if } T \in S_{slip} \end{cases} \quad (3.9)$$

k is chosen so as to satisfy the traction boundary. S_{stick} is the area where the traction is already within the limit and where there should be no slip, so the traction does not need to be changed.

An alternative way to ensure this would be to change the variables in the slip area: as the traction norm is prescribed, only the angle is unknown. This is the approach chosen in [19], but it was not tested here.

The current way of changing the traction may fail at low friction coefficients when slope is accounted for: indeed $T = 0$ does not necessarily lie within the ellipse of admissible traction in this case, so sometimes there is no solution for k . This problem can be avoided by using the following equation instead:

$$T \rightarrow T_{rec} = \begin{cases} T & \text{if } T \in S_{stick} \\ \begin{pmatrix} T_x + k(T_x - P \frac{N_x}{N_z}) \\ T_y + k(T_y - P \frac{N_y}{N_z}) \end{pmatrix} & \text{if } T \in S_{slip} \end{cases} \quad (3.10)$$

This equation always works as the point $\begin{pmatrix} T_x - PN_x/N_z \\ T_y - PN_y/N_z \end{pmatrix}$ is always inside the ellipse.

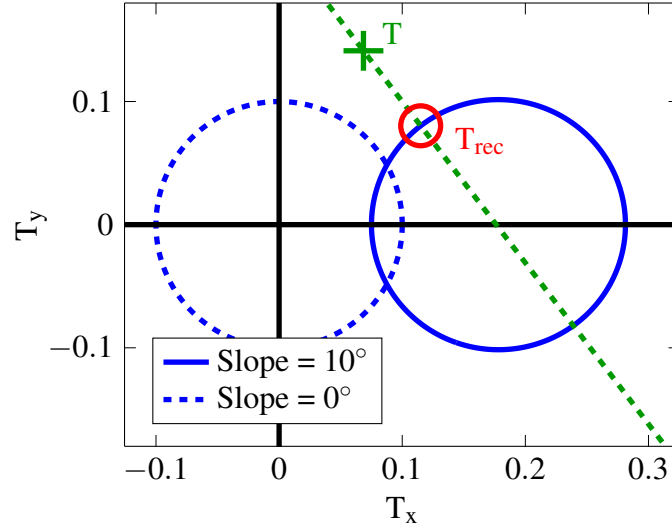


Figure 3.3: Traction boundary with or without slope, with $P = 1$ and $\mu = 0.1$. The slope is in the x direction. Using Equation 3.10, a traction T is rectified into T_{rec} in order to comply with the friction law.

Figure 3.3 shows how the traction is modified according to Equation 3.10 for a contact with a low coefficient of friction $\mu = 0.1$. In this case, using Equation 3.9 would not have allowed any admissible solution.

For both equations, k is such that T_{rec} is on the traction boundary, that is to say T_{rec} satisfies Equation 3.4. It leads to a second order equation for k ; which can be found in Appendix B.

3.2.3 Conjugate Gradient algorithm

Minimization of the functional defined in Equation 3.7 is done by a conjugate gradient algorithm, similar to the one described in Chapter 2 for the normal contact, that is to say the algorithm iterates on the tangential stress fields (T_x, T_y) until the displacement field satisfies the boundary conditions.

The residual can be deduced from the functional and is:

$$r = -\frac{\partial \mathcal{F}_{tan}}{\partial T} = \begin{cases} DX - A_T \cdot T & \text{if } (i, j) \in S_c \\ 0 & \text{if } (i, j) \in \neg S_c \end{cases} \quad (3.11)$$

S_c is the contact surface and $\neg S_c$ is the surface that is not in contact. Interestingly, the residual corresponds to the local slip: it should converge towards zero in the stick zone.

The algorithm starts with an initial traction guess T_0 . This traction is modified into $T_{rec,0}$ so that it follows the friction law. The residual is computed using Equation 3.11. The initial search direction d_0 is set to be equal to the initial residual r_0 .

Suppose it is the end of iteration n .

Line search

The new traction field is $T_{n+1} = T_n + \alpha d_n$. α is such that $-\partial \mathcal{F}_{tan} / \partial \alpha = r_{n+1}^T \cdot \partial T_{rec} / \partial \alpha = 0$. Its computation is quite complicated because of the traction rectification process described in the previous paragraph. To compute it, the first step is to input T_{n+1} instead of T into equation 3.10 and then into Equation 3.4. This allows the computation of an approximation of k and $\partial k / \partial \alpha$, using the hypothesis $\|\alpha d\| \ll \|T\|$.

After a first order expansion, α is given by Equation 3.12. $K_{\alpha,1}$ and $K_{\alpha,2}$ are defined in Appendix B and are equal to zero in the stick zone. If there is no slip at all, Equation 3.12 is simply the standard formula for α in the linear conjugate gradient method.

$$\alpha = \frac{(d_n + K_{\alpha,1})^T \cdot r_n}{(d_n + K_{\alpha,1})^T \cdot A_T \cdot (d_n + K_{\alpha,1})^T - K_{\alpha,2}^T \cdot r_n} \quad (3.12)$$

New residual

The sliding surface S_{slip} is defined as the set of points where the traction is out of bounds. The new traction field T_{n+1} is modified in S_{slip} into $T_{rec,n+1}$ so as to satisfy the friction law, using Equation 3.10 with the appropriate value of k . A second order equation is solved in order to get the right value at each point of the mesh in S_{slip} , which impacts the total computational time.

Using this traction field the new residual is computed from Equation 3.11.

The points sliding in the opposite direction of the friction force are removed from S_{slip} , in other words they are removed if $(T_{rec,n+1} - PN/N_z)^T \cdot r_{n+1} < 0$, where $N = \begin{pmatrix} N_x \\ N_y \end{pmatrix}$.

New search direction

The new search direction is computed from the new residual and the previous search direction $d_{n+1} = r_{n+1} + \beta d_n$. As the problem is strongly non-linear due to the friction law, a formula for β adapted to non-linear problems is used. Several choices are possible and here we use the value given by Hager and Zhang [72] and given by Equation 3.13, with $\theta \in [\frac{1}{4} : +\infty]$ being a free parameter. The original Hager-Zhang model uses $\theta = 2$, but some authors [73] argue that $\theta = 1$ may be a better choice.

$$\begin{aligned} \beta &= \beta_1 + \theta \beta_2 \\ \beta_1 &= -\frac{y_{n+1}^T \cdot r_{n+1}}{d_n^T \cdot y_{n+1}} \\ \beta_2 &= d_n^T \cdot r_{n+1} * \frac{y_{n+1}^T \cdot y_{n+1}}{(d_n^T \cdot y_{n+1})^2} \\ y_{n+1} &= r_{n+1} - r_n \end{aligned} \quad (3.13)$$

β_1 is very similar to the value of β in the linear conjugate gradient method, as y_i is an approximation of $\alpha A_T \cdot d_n$. So β_1 is the classical value which gives the best results in the linear conjugate gradient method. Consequently, small values of θ are likely to give better results for low slip ratios, while for high slip ratios $\theta \in [1 : 4]$ is likely to have a better convergence rate.

Using the formula as is, the algorithm has a poor convergence rate and often fails to converge at all. Equation 3.12 which describes α suggests that $d_n + K_{\alpha,1}$ plays the role of d_n in the present case. Using this in Equation 3.13 leads to Equation 3.14.

$$\begin{aligned}\beta &= \beta_1 + \theta\beta_2 \\ \beta_1 &= -\frac{y_{n+1}^T \cdot r_{n+1}}{(d_n + K_{\alpha,1})^T \cdot y_{n+1}} \\ \beta_2 &= (d_n + K_{\alpha,1})^T \cdot r_{n+1} * \frac{y_{n+1}^T \cdot y_{n+1}}{((d_n + K_{\alpha,1})^T \cdot y_{n+1})^2} \\ y_{n+1} &= r_{n+1} - r_n\end{aligned}\tag{3.14}$$

Using this last equation along with $d_{n+1} = r_{n+1} + \beta d_n$ for the computation of the new search direction, the algorithm converges.

Convergence criterion

The loop stops if the convergence criterion is below a given tolerance. The convergence criterion is given in Equation 3.15, it is the same as the one used in [19]. $\|\dots\|_{RMS}$ stands for the RMS norm.

$$c = \frac{\|T_{n+1} - T_n\|_{RMS}}{\|T_{n+1}\|_{RMS}}\tag{3.15}$$

This convergence criterion might not be suitable if the convergence is slow. In this case a second convergence criterion can be used using the RMS of the residual *in the sticking area*, which should converge towards zero (the residual in the slipping area does not). In this latter case the loop stops if both the criteria are below the tolerance.

This algorithm works well as long as the required precision is not too high. Its main problem is that the residual does not tend to zero in the slip zone because the residual actually measures the slip.

3.2.4 Conjugate gradient with perpendicular residual

One way to avoid this problem is to modify the value of the residual in the slip zone for the computation of both α and β . The modified residual r_{mod} is computed in order to be perpendicular to the traction at each point. It can be approximated by ensuring that for

each point (i, j) , $r_{mod,(i,j)}^T \cdot (T_{(i,j)} - P_{(i,j)}N_{(i,j)}/N_z) = 0$, where $N_{(i,j)} = \begin{pmatrix} N_{(i,j),x} \\ N_{(i,j),y} \end{pmatrix}$. The term $P_{(i,j)}N_{(i,j)}/N_z$ is added to account for the slope effect.

This is achieved by using Equation 3.16 for each point in the slip area. The residual for the points in the stick area is not modified.

$$r_{mod,(i,j)} = r_{(i,j)} - r_{(i,j)}^T \cdot \left(T_{(i,j)} - P_{(i,j)} \frac{N_{(i,j)}}{N_z} \right) \frac{T_{(i,j)} - P_{(i,j)} \frac{N_{(i,j)}}{N_z}}{\|T_{(i,j)} - P_{(i,j)} \frac{N_{(i,j)}}{N_z}\|} \quad (3.16)$$

Using r_{mod} instead of r in Equations 3.12 and 3.14 leads to a more precise and more stable algorithm.

3.3 Validation and performance

The algorithm is validated against the analytical result for a Hertzian contact with friction derived by Mindlin [32] and described in paragraph 1.2.1. Figure 3.4 shows the evolution of the tangential force with the slip ratio, showing very good agreement- the simulation is run without accounting for the slope. The tangential force is represented as an apparent friction coefficient μ , which is simply the tangential force divided by the normal force. The lateral displacement is dimensionless: its unit is the contact radius. It should be mentioned that the agreement is not perfect, independently of the mesh size or the convergence criterion of the algorithm: that is because Mindlin's solution assumes there is no traction acting in the direction perpendicular to the sliding direction. This assumption is known to be wrong as it leads to displacements that are not strictly parallel to the sliding direction (which should not be possible as one of the condition of the friction law is that stress and slip are in the same direction). However, it appears to be a very reasonable assumption, as the relative error in global tangential force between Mindlin's result and the simulation is $\approx 10^{-3}$.

To assess the performance of the algorithm, it is compared to the one described in [19]. As they both use a conjugate gradient algorithm, they are compared in terms of number of iterations before convergence, using the same convergence criterion (Equation 3.15 with a tolerance of 10^{-5}). All the other parameters are the same: shear modulus $G = 200$ MPa, Poisson coefficient $\nu = 0.42$, radius of the sphere $R_h = 50$ mm, normal force $F_n = 9.196$ N. Once again the slope is not accounted for.

Figure 3.5 shows that the algorithm described in this section is competitive compared to Zhao's algorithm in terms of number of iterations. A comparison in terms of computational time was not made as it depends strongly on the detailed optimization of each algorithm and may have consequently been biased. This figure also shows that the number of iterations increases with the number of unknowns, it is approximately $O(\mathcal{N}_T^{0.4})$, where \mathcal{N}_T is the number of traction unknowns. There is an exception for the full slip case

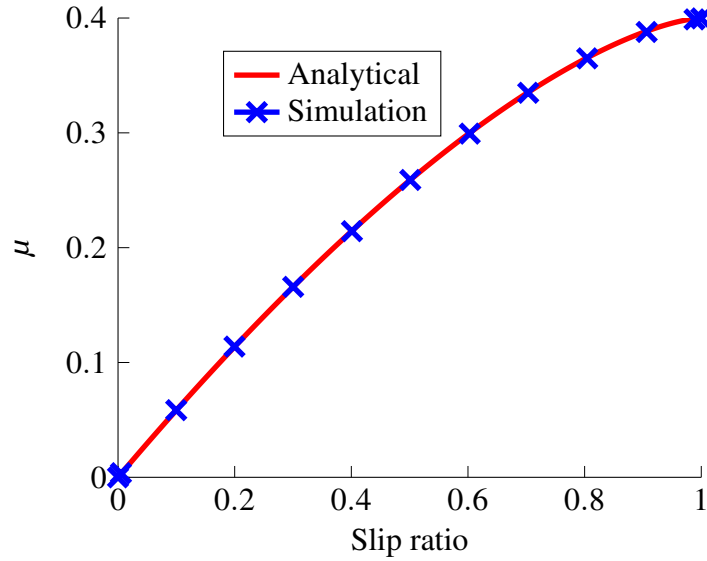


Figure 3.4: Ratio between tangential force and normal force as a function of the slip ratio for a Hertzian contact with a Coulomb friction law. The friction coefficient is 0.4. The simulation is in good agreement with the analytical result from [32].

where the number of iterations seems relatively independent of the number of unknowns. A possible explanation is that in this case, using $T_x(i, j) = \mu P(i, j)$ and $T_y(i, j) = 0$ for each point (i, j) already yields a quite good solution, as it is the traction field of the analytical solution from Mindlin. This traction field is also the one that the current algorithm is likely to try at the first iteration of the conjugate gradient, which means that after only one iteration the algorithm already yields a good solution independently of the number of unknowns.

3.4 Viscoelasticity

Viscoelasticity can be implemented in the tangential direction exactly in the same way as in the normal direction (paragraph 2.1.3), by discretizing time into small time steps and considering that the traction field and displacements vary linearly between the time steps. It leads to a tangential version of Equation 2.13, where A_T should be used instead of A_{zz} and U_T instead of U . The algorithm described above for an elastic material can be used to solve the viscoelastic problem by using T' , U'_T and DX' instead of T , U_T and DX according to Equation 3.17. This yields $U_{T,t+\Delta t}$ and $\sum_k T_{t+\Delta t}^k$, which is the total traction acting on the surface.

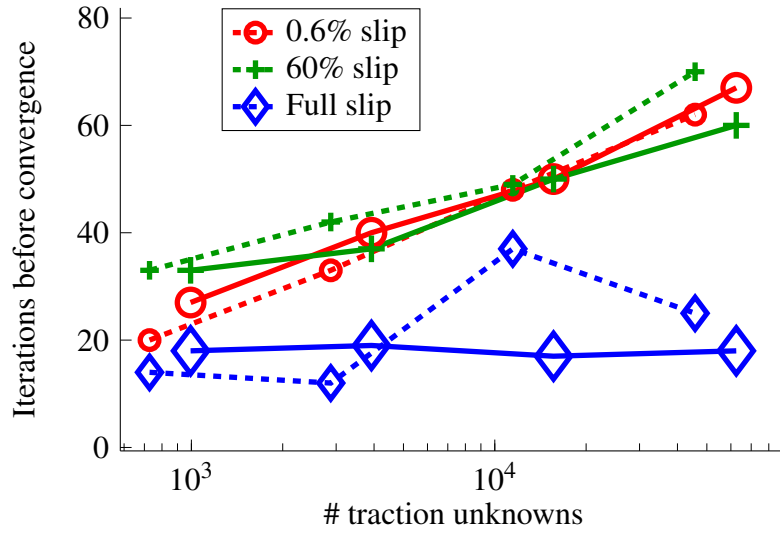


Figure 3.5: Number of iterations before convergence as a function of the number of unknowns for different slip ratios. Full lines are for the current model, dashed lines are from Zhao's algorithm [19].

$$\begin{aligned}
 T' &= \sum_k T_{t+\Delta t}^k \\
 U_T' &= A_T T' \\
 DX' &= DX \left[G_\infty + \sum_k \frac{G_1^k + \frac{\eta_1^k}{\Delta t}}{1 + \frac{G_1^k}{G_0^k} + \frac{\eta_1^k}{G_0^k \Delta t}} \right] - U_{T,t} \sum_k \frac{\frac{\eta_1^k}{\Delta t}}{1 + \frac{G_1^k}{G_0^k} + \frac{\eta_1^k}{G_0^k \Delta t}} \\
 &\quad + \sum_k A_T T_t^k \frac{\frac{\eta_1^k}{G_0^k \Delta t}}{1 + \frac{G_1^k}{G_0^k} + \frac{\eta_1^k}{G_0^k \Delta t}}
 \end{aligned} \tag{3.17}$$

It should be pointed out that it is necessary to compute and to store the state variables $A_T T_t^k$ for each branch of the generalized Zener model between each time step using Equation 2.12.

3.5 Interpolation

The naive way to model a contact with a prescribed lateral displacement of ΔX would be simply to use $DX = \Delta X$ in the current model and solve it in one step. Doing this would

however give a slightly wrong answer because a frictional contact is history dependent, that is to say the result would not be the same if the problem is solved in one step or if it is solved after a number of small steps. The latter solution is of course closer to the reality, as long as the displacement during one step is small compared to the characteristic size of the problem.

Suppose it is the end of step n . The total lateral displacement is ΔX_n , the tangential displacement of the half-space is $U_{T,n}$. During the next step, an extra lateral displacement of δ is prescribed, so that the total lateral displacement is $\Delta X_{n+1} = \Delta X_n + \delta$. The proper way to solve the problem for step $n + 1$ is to use $DX = U_{T,n} + \delta$ in the algorithm.

During each step, the half-space and the surface it is in contact with move relatively to each other as they slip. These movements have to be accounted for with an interpolation procedure. Even if they are small (because of the hypothesis of small strain), these movements can influence the transient contact if the material is viscoelastic: the local slip is likely to cause energy dissipation even if the surface is only partly sliding.

The interpolation needs to be done at each step according to the extra slip during the step. It can be done in two ways. The ‘Eulerian’ way is to interpolate the material characteristics depending on the slip at each point of the rigid substrate, while the ‘Lagrangian’ way is to interpolate the rigid substrate depending on the slip of each point of the half-space. Both approaches should lead to the same results as long as the small strain hypothesis remains valid. The ‘Eulerian’ way may seem more appropriate: as the substrate is rigid, it seems counter-intuitive to distort it through an interpolation procedure. But it means all the variable fields related to the material have to be interpolated: the displacement fields (3 fields: one in each direction) and the internal viscoelastic variables (3 fields multiplied by the number of viscoelastic branches of the material), so this solution is quite expensive in terms of computing time. The ‘Lagrangian’ way is much more efficient: only the height map H of the substrate needs to be interpolated (1 field) and the slopes have to be re-computed. In this case, it might be useful to keep the original, not interpolated height map H_0 in memory at all times instead of storing the new, interpolated height map at each time step as the repeated interpolations may modify it: they are very likely to gradually smoothen the summits.

A linear interpolation was chosen in all cases, but higher order interpolation procedures can also be used.

The edges of the simulation area should be treated with care. In the case of periodic boundary conditions, the interpolation procedure should take this particularity into account. In the case of non-periodic boundary conditions, it is more difficult: at each step, some points leave the zone under consideration while other points enter. For a ‘Lagrangian’ interpolation, the height of the points entering the contact zone should be low enough so as to never touch the elastic half-space, otherwise they may interfere with the simulation.

For a non periodic contact, it is tempting to use a ‘Eulerian’ interpolation, as it would allow to discretize only a small square around the contact surface (the smallest square possible so as to get the best precision). During sliding, the points entering the simulated zone and then the contact zone will have a physical meaning and thus provide a precise

result.

Unfortunately, this approach only works for elastic materials because in the case of a viscoelastic material, the internal variables of the points entering the simulation zone are unknown and are not zero. It means that in this case, all the points that are likely to enter the contact area at some point in time have to be included in the simulation from the beginning. If the sliding distance is large compared to the length of the contact area, it leads to either slower computations due to a higher number of points, or a loss of precision due to the poor discretization of the contact zone. This effect, in addition to the zero-padding procedure described in paragraph 2.1.1 makes the non-periodic algorithm inefficient compared to the periodic one.

3.5.1 Comparison with Finite Element simulation

In order to validate the model and to illustrate the slope effect a comparison with a Finite Element (FE) analysis is performed, using the commercial software Abaqus 6.14. The case studied is a 2-D plane strain analysis of a cylinder on a viscoelastic half space. In Abaqus, the half space is approximated by a rectangle 5 mm high and 15 mm long, which makes it large compared to the size of the contact. The cylinder radius is 10 mm. A normal force of 100 N is first applied during 0.1 ms, then sliding starts at constant speed (110 mm s^{-1}) until a “pseudo” steady-state is reached. The material characteristics are the same as the one used in [74] (where an analytical solution of a similar problem in steady-state is derived): a Zener branch ($G_0 = 3 \text{ MPa}$, $\tau = 1.11 \text{ ms}$) in parallel with an elastic branch ($G_\infty = 0.333 \text{ MPa}$).

First the contact is modeled without friction. Both the FE simulation and the current model predict a tangential force of 4.5 N caused by the viscoelastic losses (see Figure 3.6). There is a 3.5 % difference between the two solutions.

With a Coulomb friction law ($\mu = 1.5$), the current model yields different predictions if the slope is accounted for or not. Without slope effect, the tangential force at $t = 0.025 \text{ s}$ is $F_{t,\text{no slope}} = 154 \text{ N}$, while with slope $F_{t,\text{slope}} = 165 \text{ N}$ and the FE simulation predicts $F_{t,\text{FE}} = 168 \text{ N}$. Consequently, the current model gives far better predictions when the local slope is taken into account as the relative difference of tangential force goes from 8 % without slope to only 2 % with slope, taking the FE result as a reference. Figure 3.7 shows the mesh and the shear stress in the bulk predicted by the FE simulation. It should be mentioned that the ‘slope effect’ is accounted for in the FE simulation, as the cylinder is not considered to be flat.

Interestingly, the tangential force without slope is almost exactly equal to the sum of the tangential forces caused by the viscoelastic losses without friction and the tangential force caused by the friction law μF_n . As discussed in paragraph 3.1.1 it is not a surprising result as there is no coupling between normal and tangential directions in the present case. In order to model a contact in full sliding and with very low slopes, modeling friction is not really necessary: the total tangential force can be easily deduced from the viscoelastic losses and the friction law. However, as soon as slopes are not negligible they cause an extra tangential force which has to be accounted for. This extra tangential force is not

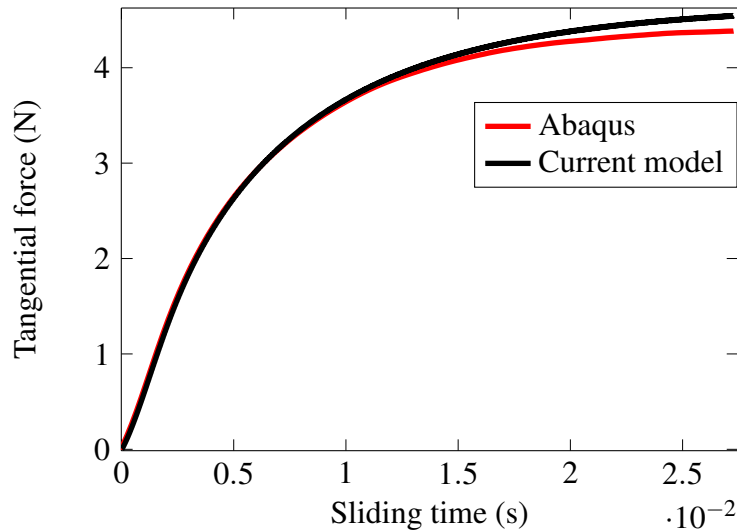


Figure 3.6: Evolution of the tangential force with time during the sliding of a rigid cylinder on a viscoelastic half-space without friction.

only related to the geometry and the friction law, but also to the viscoelasticity: if the viscoelastic losses are low (at very low or very high velocity for example), the contact area is symmetric. The extra friction caused by the slope at the leading edge of the contact is therefore balanced by the friction deficit at the trailing edge of the contact, so that the total tangential force is almost unaffected. On the other hand if viscoelastic losses are high the contact area is not symmetric anymore and is located mainly at the front of the cylinder (or of the sphere in the case of Hertzian contact) so the extra friction force at the leading edge remains but is not balanced anymore by a friction deficit at the trailing edge.

Figure 3.8 shows the tangential stress along a cross-section of the cylinder at different times. It shows that the current model slightly overestimates the contact area but otherwise the results remain very close to the FE simulation. At $t = 0.14$ ms, a small area is not yet sliding in the FE simulation, which causes a ‘hole’ in the shear stress distribution - this area is already sliding in the prediction made by the current model, so the hole does not appear.

3.6 Inertia

3.6.1 Numerical instability

The algorithm works well in a lot of cases but proves to be unstable under certain conditions. This problem can be caused by a number of reasons and is characterized by oscillations in the tangential force, sliding speed or local shear stress during the time steps. These oscillations are dependent on the length of the time steps but in a number of cases reducing the time step length tends to amplify the problem. Because of friction, these oscillations turn into stick/slip motions when their amplitude is too high but do not have any

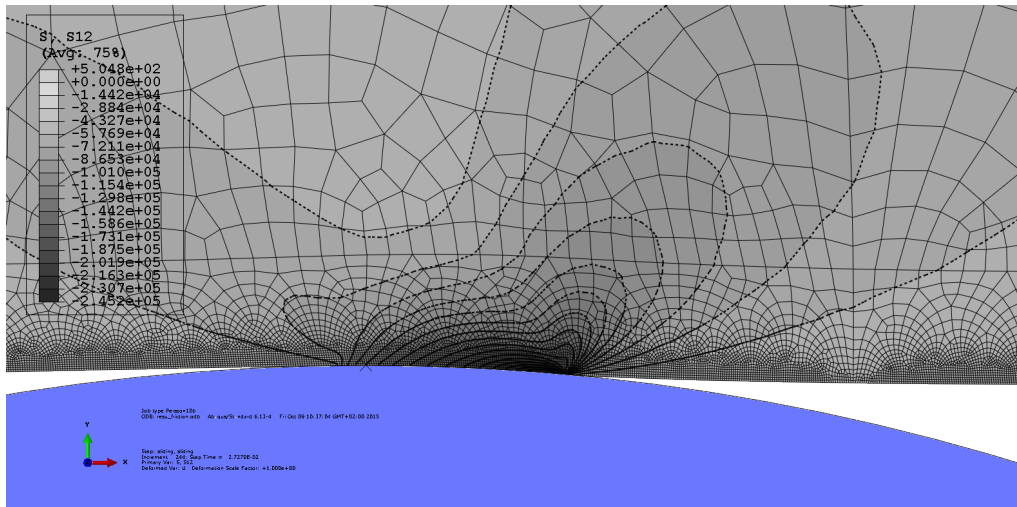


Figure 3.7: FE result at the end of the simulation of the sliding of a rigid cylinder on a viscoelastic half-space. The shear stress in the bulk is plotted.

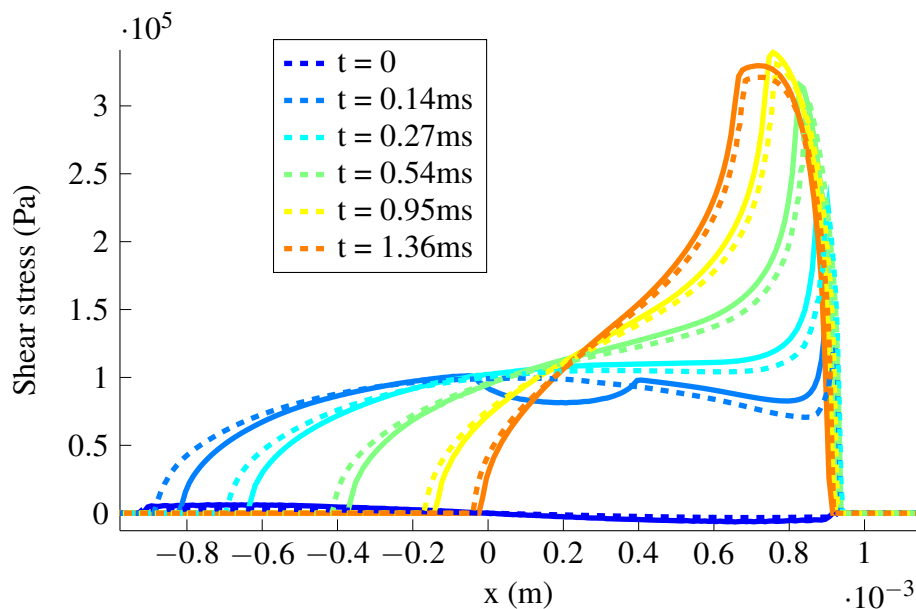


Figure 3.8: Shear stress along the x axis during the transient sliding of a rigid cylinder on a viscoelastic half-space at different times. The dashed lines are for the model, the solid lines for the FE simulations. $x = 0$ is the center of the cylinder.

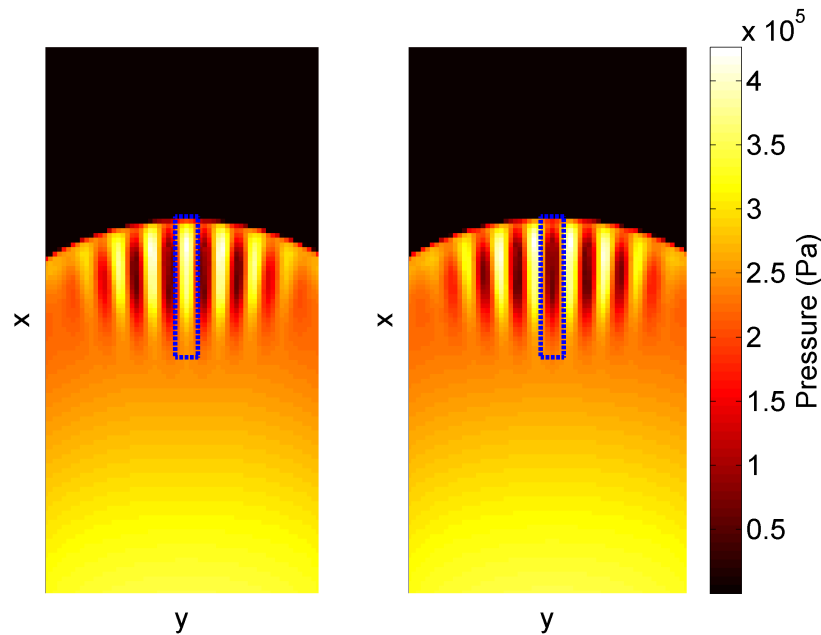


Figure 3.9: Top view of the pressure field in a viscoelastic Hertzian contact for two consecutive time steps. The sphere is moving from the bottom to the top of the picture. Numerical instability is responsible for the wavy pressure pattern at the leading edge of the contact.

physical meaning as their period is only 1 time step.

There are two kinds of oscillations: they can be either local (typically, stick/slip of certain points at the leading edge of a contact) or global (stick slip occurring for the full half-space). Local stick slip can be caused by excessive strain, for example if two points overlap. It can also be caused by a coupling between the Coulomb friction law and viscoelasticity. Suppose sliding is occurring at constant speed and steady state has been reached. At one point, if there is a small ‘overpressure’, the friction force will also be slightly higher, which in turns reduces the local sliding hence the local sliding speed. For a viscoelastic material, a lower speed means a softer material, so at the next step the pressure at this point will be slightly lower than the normal steady-state value. This lower pressure means less friction, higher sliding speed... and this phenomenon in certain cases becomes unstable. These two phenomena causing local stick/slip cannot be helped, except by using the algorithm in easier conditions, that is to say keeping the strains small (not to mention that high strain also degrades the precision of the results). An example of this behaviour is given in Figure 3.9, which represents the pressure field of at the leading edge of a viscoelastic Hertzian contact for two consecutive time steps. In the dashed rectangle, the pressure oscillates between a very high and a very low value. The total normal force is constant because the high pressure zones are balanced by low pressure zones, which forms a wavy pattern.

The ‘global’ stick/slip phenomenon is quite similar and happens mostly when slope is accounted for. It can be understood as follows. Suppose the global sliding speed is a bit too high. In some conditions, it causes the contact area to be less symmetric and located a bit more at the front side of the cylinder or sphere. At the next step, it causes more friction because of the slope effect and consequently a sliding speed slightly too low compared to its steady-state value. Once again in some cases this motion can amplify and become unstable, usually when the material is soft and thick.

3.6.2 Implementation

This latter phenomenon can be overcome by adding inertia effects to the model. A complete dynamic analysis is not possible, as it would require a 3-dimensional mesh to account for the wave propagation inside the bulk. Moreover, the problem under consideration only concerns the mean speed of the interface. The oscillations of the mean speed can be damped by adding a ‘mean mass’ to the problem, that is to say the inertial effects only have to impact the mean displacement of the interface in the tangential direction.

A simple first order backwards scheme is used to include inertial effects. Though a first order scheme may impede precision (by artificially damping the oscillations due to inertia if the time steps are too large), it has the advantage of being easy to implement along with viscoelasticity and proves to be efficient for the purpose of damping the non-physical, numerical oscillations. It is also supposed that the lateral displacement is imposed uniformly at the top of the rubber block by U^{top} .

Adding a mass to the system is then done by using Equation 3.18 instead of Equation 3.17.

$$\begin{aligned}
 T' &= \sum_k T_{t+\Delta t}^k \\
 U_T' &= A_T T' \\
 DX' &= \left[G_\infty + \sum_k \frac{G_1^k + \frac{\eta_1^k}{\Delta t}}{1 + \frac{G_1^k}{G_0^k} + \frac{\eta_1^k}{G_0^k \Delta t}} + \frac{2}{\Delta t^2} A_T M \right] DX - U_{T,t} \sum_k \frac{\frac{\eta_1^k}{\Delta t}}{1 + \frac{G_1^k}{G_0^k} + \frac{\eta_1^k}{G_0^k \Delta t}} \\
 &\quad + \sum_k A_T T_t^k \frac{\frac{\eta_1^k}{\Delta t}}{1 + \frac{G_1^k}{G_0^k} + \frac{\eta_1^k}{G_0^k \Delta t}} + A_T M \left(\frac{2}{\Delta t^2} U_{T,t} - \frac{2}{\Delta t^2} (U_{t+\Delta t}^{top} - U_t^{top}) + \frac{2}{\Delta t} \dot{U}_{T,t} + \ddot{U}_{T,t} \right)
 \end{aligned} \tag{3.18}$$

Acceleration \ddot{U}_{t+dt} and speed \dot{U}_{t+dt} are given by Equation 3.19. U^{top} appears in the definition of the speed because the displacement field U_T is relative to the movement of the top of the rubber block: if the relative displacement is zero, the sliding speed (the

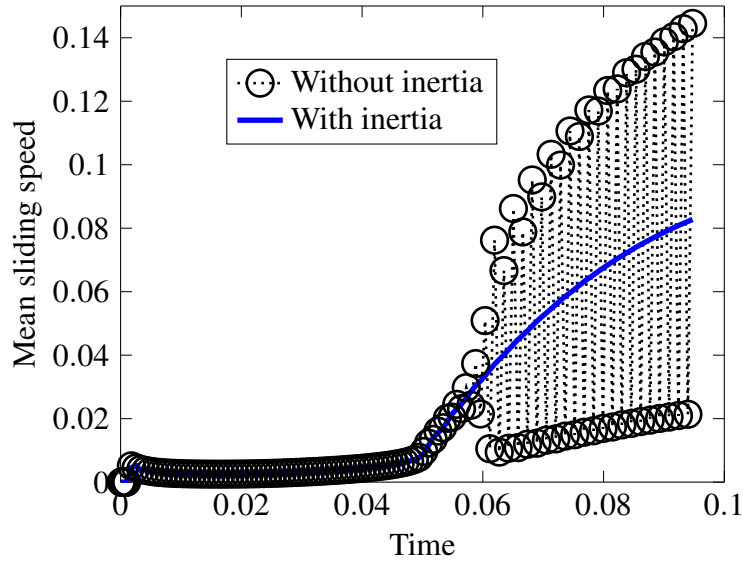


Figure 3.10: Mean sliding speed as a function of time for a Hertzian viscoelastic contact. A constant velocity prescribed on the top of the block from time $t = 0$ onward.

mean speed at the bottom of the block) is equal to the speed of the top of the block.

$$\begin{aligned}\dot{U}_{T,t+\Delta t} &= \frac{U_{T,t+\Delta t} - U_{T,t} + U_{t+\Delta t}^{top} - U_t^{top}}{\Delta t} \\ \ddot{U}_{T,t+\Delta t} &= 2 \frac{\dot{U}_{T,t+\Delta t} - \dot{U}_{T,t}}{\Delta t} - \ddot{U}_{T,t}\end{aligned}\quad (3.19)$$

The mass matrix M is such that $MU_T = m\bar{U}_T = m \begin{pmatrix} \bar{U}_x \\ \bar{U}_y \end{pmatrix}$. m is the mean mass of the system, which should be chosen to prevent the numerical instabilities without impacting the result otherwise.

Figure 3.10 shows the evolution of the mean sliding speed with time for a Hertzian viscoelastic contact, with a constant velocity prescribed on the top of the block from time $t = 0$ onward. The parameters chosen in this simulation lead to numerical stick-slip if no inertia is accounted for (dotted line). The plain line shows the result with a small mass added, which effectively damps the oscillations. The mean sliding speed remains close to zero at first: although a constant, non-zero velocity is applied at the top of the rubber block, the friction forces refrain the contact surface from sliding, which causes the rubber block to be sheared, up to a certain point (here $t = 0.05$) where the shearing force exceeds the friction force and sliding starts. The sliding speed is not constant because of viscoelasticity, which causes a delayed shearing of the block.

Though it is implemented primarily for damping purposes, the mass matrix can be given a physical meaning as it can be used to model the first mode oscillations of a half-space of finite thickness. For a periodic half space of thickness h and of constant density ρ , considering the shear strain is constant at all heights z , the equivalent mass is $m = \rho * h/2$.

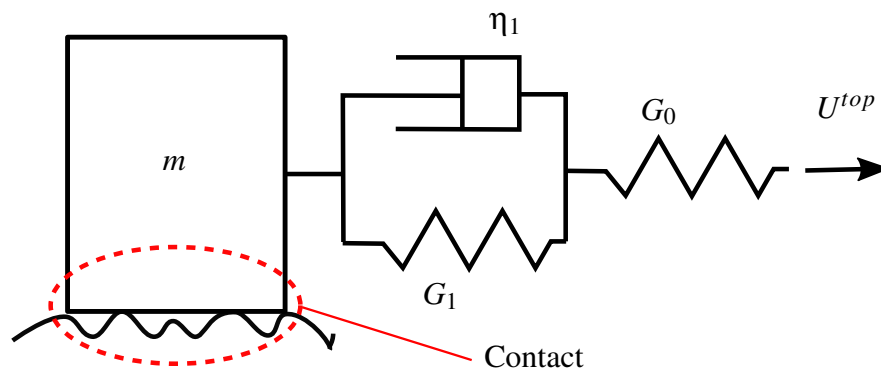


Figure 3.11: Illustration of the algorithm with inertia m : a viscoelastic material (here a simple Zener material) with a prescribed displacement at one end and a mass sliding on a rough surface on the other hand.

The problem under consideration is illustrated by Figure 3.11.

Chapter 4

Rough contact

A description of rough surfaces such as road pavement is made. Several results are presented using the current Boundary Element Method. Firstly, an elastic contact with adhesion with an extremely fine mesh is modeled for the 'Contact Mechanics Challenge'. Secondly, a comparison to Persson's analytical model is performed for a transient viscoelastic contact. Finally, simulations on a 2-scale model surface are run to investigate the roles of the different scales on a transient, viscoelastic contact, with friction and adhesion.

4.1 Numerical generation of rough surfaces

As mentioned in paragraph 1.2.4, road surfaces are self-affine rough surfaces which can be characterized by their Power Spectral Density Φ . A first approximation of the PSD of road surfaces is given in Equation 1.6, which reduces the surface description to several meaningful statistical parameters. These parameters are useful for the development of analytical theories such as Persson's [3][4], but cannot be used directly as an input in a numerical simulation. This input should be the height map of the surface itself, or at least a good representation. The best way to get this height map would be to measure a surface, filter the result in order to get rid of the measurement defects and format it properly. A first drawback of this method is the difficulty and cost to measure the surface, in particular if different surfaces are to be tested. A second drawback is that, despite having results close to what happens in real life, using this method makes it difficult to understand the role of the different parameters of the surface as they cannot be easily modified.

That is why a simpler method is commonly used in simulation. Using the hypothesis that road surfaces are random, self-affine and fully characterized by their PSD, methods have been developed to numerically generate random surfaces having the same characteristics. The algorithm described in [75] starts by generating a sequence of independent random numbers (in the present case, having a Gaussian distribution). By applying a linear filter to this sequence, it is possible to generate a random Gaussian surface. In [75] the parameters of the filter necessary to obtain a surface with a given PSD are described. Applying the filter to the random sequence can be performed efficiently in Fourier space as it is a convolution product. This method is quite complex but very general as it can be used to generate anisotropic, non-Gaussian surfaces. A simpler method is described in [64], where the amplitude of each component of the Fourier Transform of the surface are derived from the PSD and where the phase of each component is randomly generated. An inverse Fourier Transform is then performed to have a surface in real space.

When generating random surfaces, particular attention is required concerning the wavenumber cut-offs k_l and k_s . Yastrebov *et al.* [53] highlighted that the largest wavelength should remain small compared to the size of the simulation ($k_l > 2\pi/L$) in order to achieve meaningful results. Otherwise, the generated surfaces are non Gaussian and possibly non isotropic. The smallest wavelength should also be larger than the size of a cell to achieve a reasonable precision: $k_s < 2\pi N/L$.

4.2 The “Contact Mechanics Challenge”

The algorithm for elastic contact with adhesive forces presented in Section 2.3 was used to participate to M. Müser's *Contact Mechanics Challenge*. The results of this challenge can be found in [27]. It consists of a self-affine rough substrate in normal contact with a linear elastic half-space and a short-range adhesion force. Prediction of numerous unknowns including contact area and mean gap as a function of the normal pressure were expected.

Answering this challenge required several simulations to be run on a very fine mesh

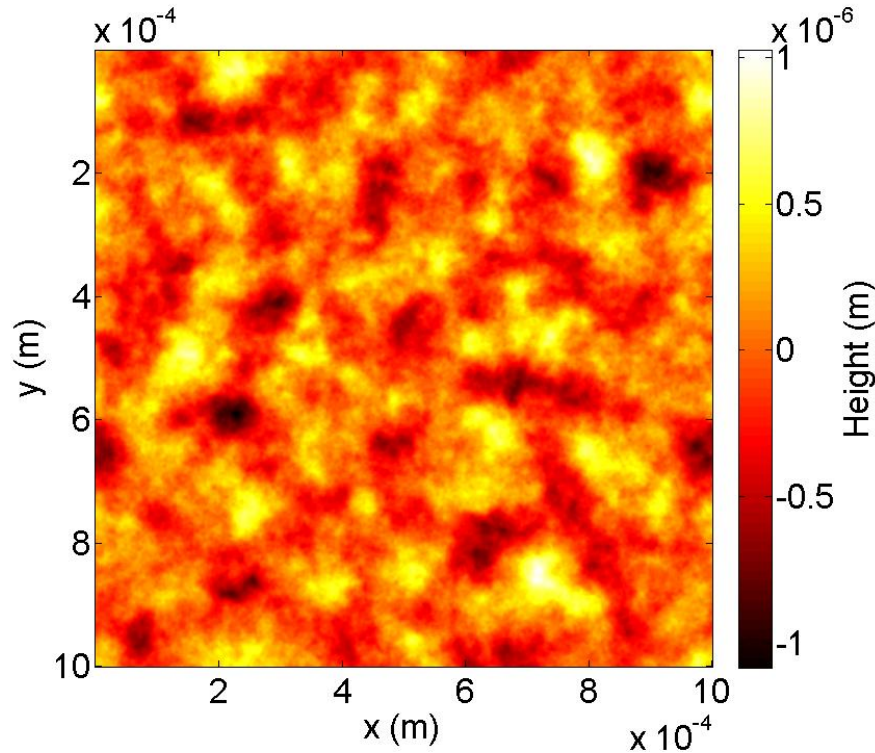


Figure 4.1: Representation of the rough surface used in the comparison against Persson’s model

(16384×16384 up to 32768×32768). On the finer mesh, the computing time was 3 weeks using a single-core computer with extra RAM memory (≈ 100 Go were necessary). A detailed study of the performance of different adhesive contact solvers can be found in [70]. In the end our simulations agreed perfectly with M.Müser’s although the results were disclosed only after our work was submitted. This fact validates the precision of the model as well as its performance for very demanding simulations.

4.3 Transient viscoelastic contact without friction

Persson’s analytical model for a transient viscoelastic contact on a rough surface [28] described in paragraph 1.2.4, uses slightly stronger hypotheses than the ones made to develop the current algorithm. In addition to the linear viscoelasticity and small strain hypotheses, his model also supposes that the deformation of the half-space follows the same PSD as the rough surface, which is strictly true only for full contact. Although it does not account for friction, it provides a good comparison for rough contacts.

His model was thus implemented with a small modification to include the correction factor introduced in [4] which gives good results at low contact area ratios [76]. This correction factor aims at reducing the predicted friction in the case of partial contact. It

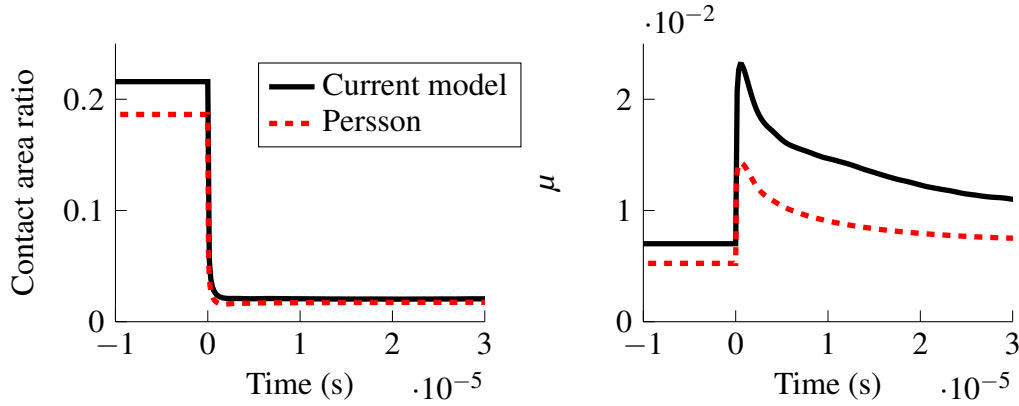


Figure 4.2: Validation against Persson's model for a speed step experiment. $V_0 = 0.01 \text{ ms}^{-1}$, $V_1 = 3 \text{ ms}^{-1}$

depends on a parameter $\gamma \in [0, 1]$. When $\gamma = 1$ the correction factor has no influence. Friction decreases as γ decreases. In the following section, the parameter $\gamma = 0.45$ is chosen as in [76].

In the examples given in [28], rubber is first sliding at constant velocity V_0 in steady-state. At $t = 0$ the prescribed speed is changed to V_1 . When $V_1 > V_0$ friction increases until it reaches a maximum μ_{max} and then decreases to its steady-state value (which can be either higher or lower than the previous steady-state value). The steady state friction coefficient is named μ_{dyn} . The existence of a friction maximum can be understood as follows: when sliding at low speed, the contact area is high and the mean gap between the two surfaces is low. When sliding at a higher speed, the steady state value of the contact area is lower while the mean gap is higher. This means the potential energy of the normal force increases. This extra energy is provided by a temporary increase of the tangential force, which is responsible for the maximum.

Simulations are run comparing the current model to Persson's. The simulations are run on a $L = 1 \text{ mm}$ large square with a $N \times N = 2048 \times 2048$ mesh and periodic boundary conditions. The random surface H has the following properties: $k_l = k_r = 2\pi * 4/L$, $k_s = 2\pi * 128/L$, $\sqrt{\langle (\nabla H)^2 \rangle} = 0.02$ and a Hurst exponent $H = 0.9$. The random surface is represented in Figure 4.1. The normal pressure is $P_m = 0.1 \text{ MPa}$. The initial velocity is $V_0 = 0.01 \text{ ms}^{-1}$ and V_1 is between 0.1 and 100 ms^{-1} . The material chosen is a typical tire material, modeled using a generalized Zener model.

Figure 4.2 shows that both models give the same evolution of the contact area ratio and of the friction coefficient μ with time, which validates the transient aspect of the current model. Both models give very similar contact area ratios, for a large range of velocities and pressures (see Figures 4.3) - Persson's model under estimating the contact area by less than 15%.

Concerning the friction coefficient, results are not as good. The difference between the models is around 30% for the steady state friction coefficient μ_{dyn} and up to 50% for the maximum friction coefficient μ_{max} at high velocities. The steady state friction coeffi-

cient is approximated by averaging the friction during the last $\approx 75\%$ of the total sliding distance, which is 0.5 mm. It is an approximation: as the size of the simulation is 1 mm, sliding for several millimeters would be necessary to reach steady state. Persson's model gives an exact solution for full contact. That is why at high pressures, when the contact area ratio is close to 1, the two models agree perfectly. From these results it seems that the reduction factor of 0.45 in Persson's model (which only applies for partial contacts) is slightly too low for the problem considered, although a 30% difference is still acceptable considering the differences between the hypotheses (and the computing time) of the two models.

Steady state friction is maximum at $V_{max} = 0.3 \text{ ms}^{-1}$. Contrary to the conclusions in [28], we find that a maximum of friction μ_{max} can appear even if V_0 and V_1 are both lower than V_{max} . It is coherent with the explanation for μ_{max} given above, as it is caused by a change in apparent stiffness of the material, independently of the viscoelastic losses. This is also confirmed by the fact that contrary to the steady state friction μ_{dyn} , μ_{max} is constantly increasing with speed, in the same way as the storage modulus is an increasing function of the frequency.

Interestingly, both μ_{dyn} and μ_{max} are only slightly dependent on pressure at low pressures. At high pressures there is almost complete contact. In this case the viscoelastic losses do not depend on pressure, leading to decreasing values of the apparent friction coefficient.

4.4 Computation of the potential energy and loss

In order to better understand the origin of the maximum in the friction curves, it is useful to compute the evolution of both the elastic energy and the viscoelastic loss during sliding. Considering a generalized standard linear solid as represented in Figure 2.1, the elastic energy stored in branch i is:

$$W_{elas}^i = W_0^i + W_1^i \quad (4.1)$$

where:

$$W_0^i = \frac{1}{2G_0^i} P_i^T A_{zz} P_i^T \quad (4.2)$$

$$W_1^i = \frac{G_1^i}{2} U^T A_{zz}^{-1} U - \frac{G_1^i}{G_0^i} U^T P_i + \frac{G_1}{2G_0^2} P_i^T A_{zz} P_i \quad (4.3)$$

These quantities can be easily computed from AP_0^i which is stored for each branch at each time step.

The energy dissipated during one time step (from t to $t + \delta t$) can be computed in two ways. The first way is to deduce the elastic energy from the total energy:

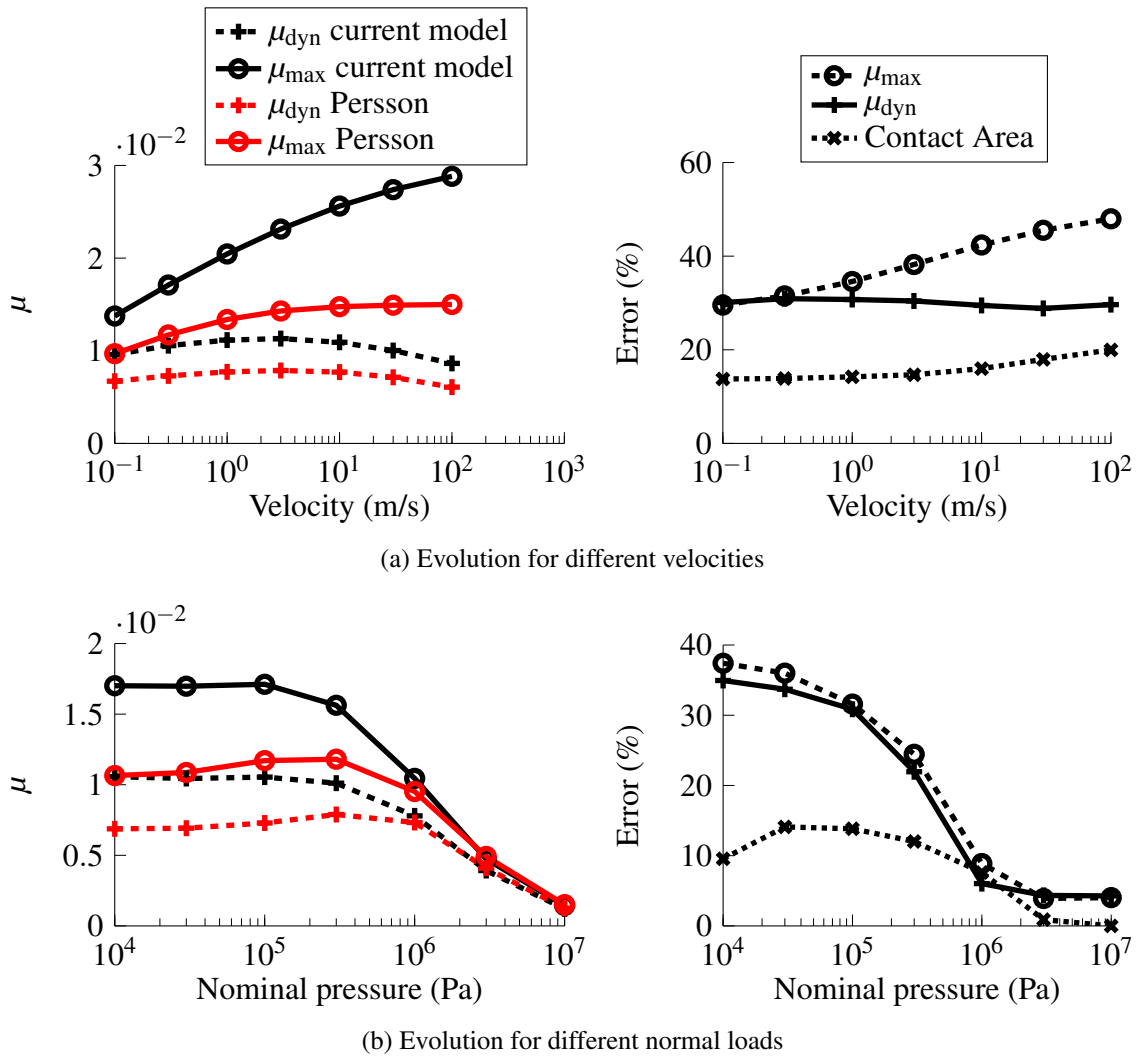


Figure 4.3: Validation against Persson’s model for a speed step experiment for different velocities (with $P_m = 0.1$ MPa) and different normal loads (with $V_2 = 0.3$ m s⁻¹). The left figures show the evolution of μ_{dyn} and μ_{max} . The right figures show the error between the two models, the current model being chosen as reference.

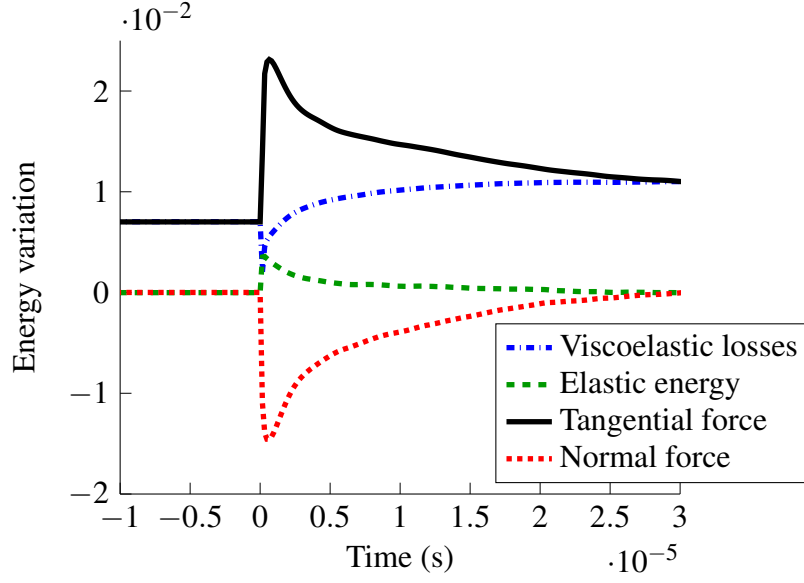


Figure 4.4: Dimensionless energy variation during a velocity step experiment. $V_0 = 0.01 \text{ m s}^{-1}$, $V_1 = 3 \text{ m s}^{-1}$

$$\begin{aligned} \Delta W_{visco} &= \Delta W_{tot} - \Delta W_{elas} \\ \Delta W_{visco} &= \left(\frac{P_{i,t+\delta t} + P_{i,t}}{2} \right)^T \cdot ((U_{t+\delta t} - \overline{U}_{t+\delta t}) - (U_t - \overline{U}_t)) - \Delta W_{elas} \end{aligned} \quad (4.4)$$

The second way is to compute it directly from the viscosity parameter:

$$\begin{aligned} \Delta W_{visco} &= \eta_1 \Delta V^T A_{zz}^{-1} \frac{\Delta V}{\Delta t} \\ \Delta V &= \Delta U - \frac{\Delta A_{zz} P}{G_0} \end{aligned} \quad (4.5)$$

This last formula does not seem to give very accurate results though. Computing the work of the normal and tangential forces is trivial using the mean normal and lateral displacements and the corresponding normal force and tangential force.

Figure 4.4 shows the variations of the potential energy of the normal force, of the tangential force, the potential elastic energy and the viscoelastic loss during the same experiment as the one in Figure 4.2, with a speed step at $t = 0$. Plotted is the variation of these energies between each time step made dimensionless by dividing them by $\Delta x P_m L^2$. This way, the dimensionless variation of potential energy of the tangential force is equal to the friction coefficient plotted in Figure 4.2. This figure confirms the fact that the maximum in the friction force is caused by an increase of potential energy of the normal force, as the rubber moves upward when the sliding speed increases. It also shows that the velocity step first causes an increase of elastic energy and a decrease of the viscoelastic losses, which increase again afterwards to reach its steady-state value, necessarily equal to the work of the tangential force.

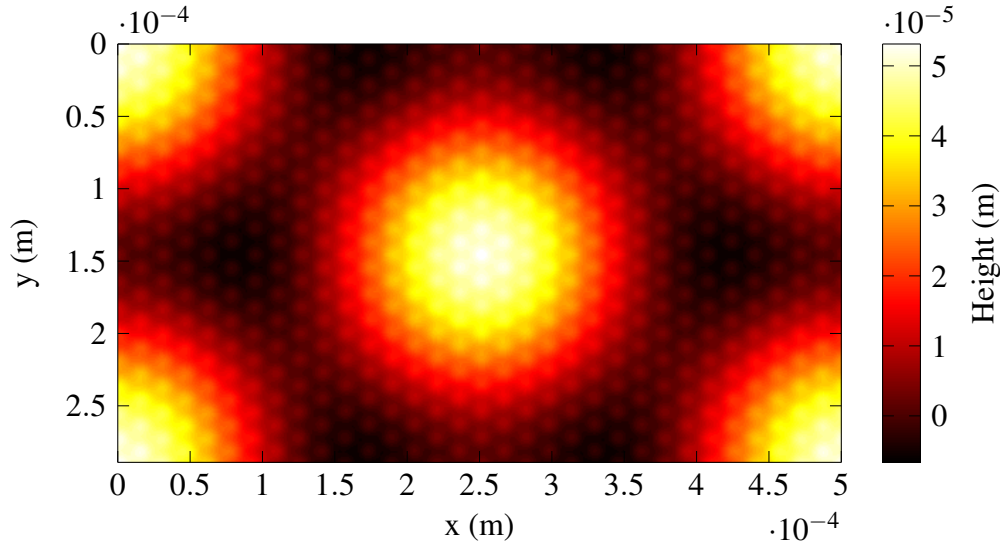


Figure 4.5: Top view of a periodic surface with two length scales.

4.5 Role of the different scales in a frictional contact

This section shows results for the sliding of a rubber material on a simplified, periodic, 2-scale rough surface. The effects of friction, sliding speed, normal load and adhesion are investigated. A simple model of a rough surface is chosen with only two length scales represented by sinusoidal waves. The height map of the surface is given in Equation 4.6, where λ is the wavelength. For each length scale, the height is a product of three sine waves in three directions.

$$H = H_{sin}(A_1, \lambda_1) + H_{sin}(A_2, \lambda_2) \quad (4.6)$$

$$H_{sin}(A, \lambda) = A \sin\left(\frac{2\pi}{\lambda} \left(\frac{1}{2}x + \frac{\sqrt{3}}{2}y\right)\right) \sin\left(\frac{2\pi}{\lambda} \left(-\frac{1}{2}x + \frac{\sqrt{3}}{2}y\right)\right) \sin\left(\frac{2\pi}{\lambda}x\right)$$

A top view of the surface used in the following is represented in Figure 4.5. Using this very simple surface allows one to easily understand the relative role of each length scale using a coarse mesh (512×296).

The loading history used is as follows: first a normal load with a mean pressure P_m is imposed during a certain loading time LT . Then, a constant driving speed V is prescribed at the top of the rubber block. It causes the rubber block first to shear, then to slide and eventually to reach a steady-state. Despite a large number of time steps (≥ 800), it should be highlighted that a true steady-state is not reached. This large number of time steps makes the computation time important in spite of the coarse mesh, typically taking 10 to 24 hours depending on the conditions. More than 300 cases were run to analyze the effects of the different parameters, for each of them the evolution of friction, contact

Larger length scale	λ_1	500 μm
Larger length scale amplitude	A_1	$\lambda_1/100$
Smaller length scale	λ_2	$\lambda_1/16$
Smaller length scale amplitude	A_2	$\lambda_2/100$
Mesh size	$N_x \times N_y$	512×296
Loading time	LT	1 ms
Sliding speed	V	1 m s^{-1}
Mean normal pressure	P_m	0.4 MPa
Coulomb friction coefficient	μ_C	1
Temperature	T	25 $^\circ\text{C}$
Thickness	h	4 mm
Density	ρ	20 kg m^{-3}

Table 4.1: Default parameters for the simulations

area and mean gap were monitored. Friction is computed in terms of apparent friction coefficient $\mu = T_m/P_m$ where T_m is the mean tangential stress in the x direction, which is the direction of sliding. For each case, the maximum friction μ_{max} and the pseudo steady-state friction μ_{dyn} are computed. μ_{dyn} is computed by averaging friction during sliding after the maximum has been reached. Unless otherwise specified, the default parameters used in the simulations are given in Table 4.1.

The density is used for damping purposes only, hence its very low value compared to real rubber.

Figure 4.6 shows a frequency sweep of the shear moduli and damping factor of the material. The three vertical black lines correspond to the characteristic frequencies of the problem for the default parameters. The first line is the characteristic frequency of the loading time $1/LT$, the second line corresponds to the characteristic frequency of the larger wavelength during steady state sliding V/λ_1 and the last line to the smaller wavelength V/λ_2 .

The evolution of contact area, apparent friction coefficient and sliding speed with time is shown in Figure 4.7. During the first millisecond, the contact area increases exponentially because of the viscoelastic relaxation. Then a driving speed of 1 m s^{-1} is prescribed on the top of the rubber block, but the sliding speed of the bottom of the rubber block where contact occurs does not change instantaneously: first shearing occurs, during which the part of the contact area that is sliding increases almost linearly. As soon as the whole contact area is sliding ($t \approx 1.25 \text{ ms}$, when the green and the black curves meet), the ‘bottom’ sliding speed increases sharply. Friction reaches a maximum, then continues to oscillate because of the periodicity of the surface. The ‘bottom’ sliding speed follows approximately the same oscillations and interestingly does not reach exactly the prescribed sliding speed, because the rubber block continues to shear while it is sliding. $\mu_{max} \approx 1.06$ and $\mu_{dyn} \approx 1.05$: those values are only slightly above the Coulomb friction coefficient $\mu_C = 1$, which indicates that the viscoelastic dissipation is low compared to the energy lost in the

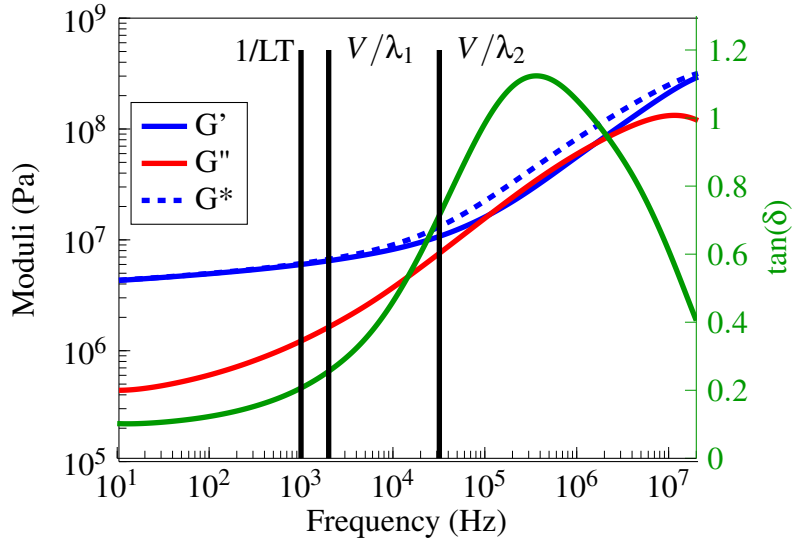


Figure 4.6: Frequency sweep of the shear moduli and damping factor of the material. The vertical bars show the frequencies that are excited during a simulation with the default parameters.

contact area because of Coulomb friction. The maximum friction is caused not only by the work of the normal force when rubber has to leave its footprint (*cf.* paragraph 4.3), but also by an increase in friction caused by the slope effect. When rubber leaves its footprint, the pressure field and contact area are highly non-symmetrical, so the mean slope in the contact area is opposite to the direction of sliding, which increases the friction forces. It was checked that inertia did not significantly impact the results.

A careful look at the oscillations of the friction curve allows one to see two wavelengths, which are reminiscent of the two wavelengths of the surface. By increasing the sliding speed to 30 ms^{-1} and looking closely, it becomes even more evident, as shown in Figure 4.8. The longer wavelength of the oscillations shown in this figure is $\approx 500 \mu\text{m}$ and the smaller wavelength $\approx 32 \mu\text{m}$, which indeed correspond to the wavelengths of the wavy surface. (They are actually a bit longer than those values due to the fact that the sliding speed of the bottom of the rubber block is lower than the driving speed).

This figure also shows the dramatic increase in shear stiffness at higher speeds, as well as a global increase in both maximum and steady-state friction. This can be explained by looking at the material characteristics in Figure 4.9, where the vertical bars show the frequencies that are excited during the simulation at $V = 30 \text{ ms}^{-1}$. The difference of material stiffness between the loading time and sliding is much more important than for the default parameters, which explains an increase in maximum friction and the material is more dissipative during sliding: both frequencies are around the peak of the damping factor $\tan(\delta)$. This explains the higher value of steady-state friction. Following the same reasoning, the steady-state friction should reach its maximum value at $V \approx 30 \text{ ms}^{-1}$ and decrease at higher velocities.

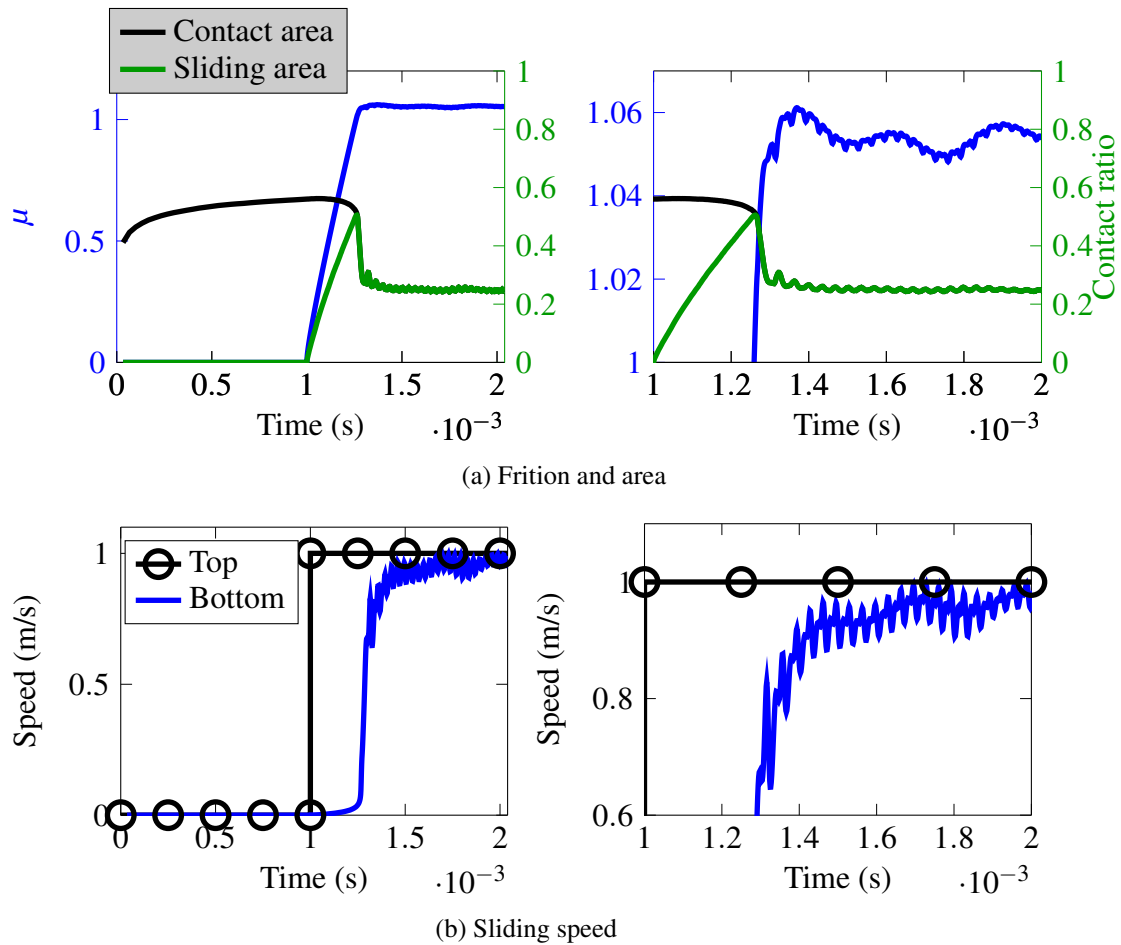


Figure 4.7: Evolution of apparent friction, contact area and sliding speed with time for the default parameters. The figures on the right are magnifications of the ones on the left in the zone of interest.

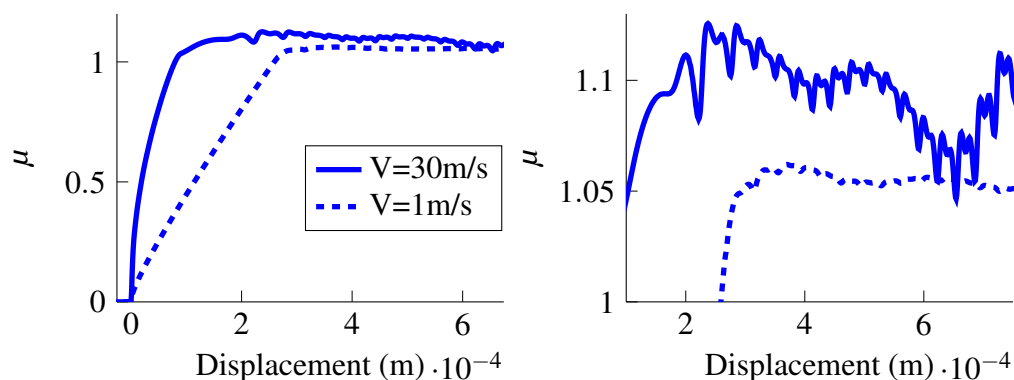


Figure 4.8: Evolution of apparent friction with the lateral displacement for a sliding speed of 30 m s^{-1} compared to the default speed 1 m s^{-1} .

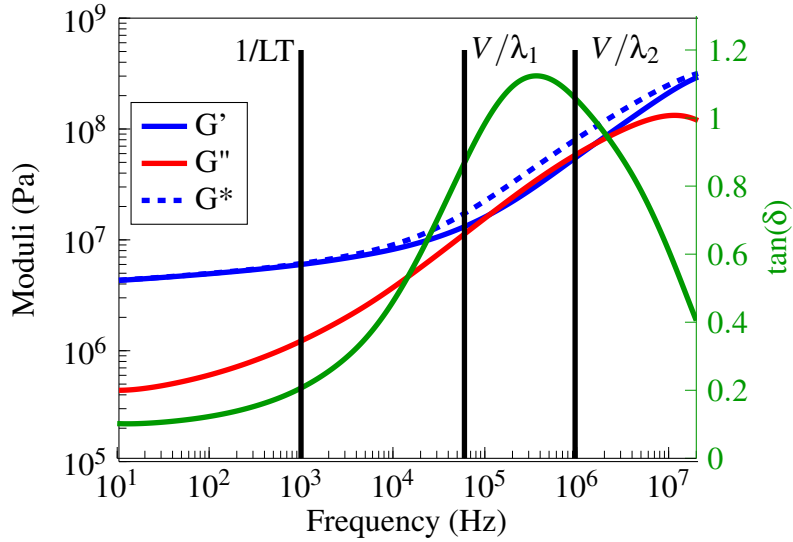


Figure 4.9: Frequency sweep of the shear moduli and damping factor of the material. The vertical bars show the frequencies that are excited during the simulation at $V = 30 \text{ m s}^{-1}$

Plotting the evolution of μ_{max} and μ_{dyn} with driving velocity validates this hypothesis (Figure 4.10). Similarly, μ_{max} keeps increasing with speed just as G' does with the frequency- we would expect a plateau at some point but simulations were not run for high enough velocities, not to mention that unrealistically high driving velocities cause significant inertial effects even with a low density of 20 kg m^{-3} .

The evolution of friction with the normal load as shown in Figure 4.11 is not as easy to understand. Steady-state friction first increases along with the normal load. There are two explanations: the first is an increase in the slope effect, as the mean slope increases with the contact surface. The second explanation is that viscoelastic losses increase faster than linearly with the normal load. It is not a surprising result: at low normal loads, the wavy

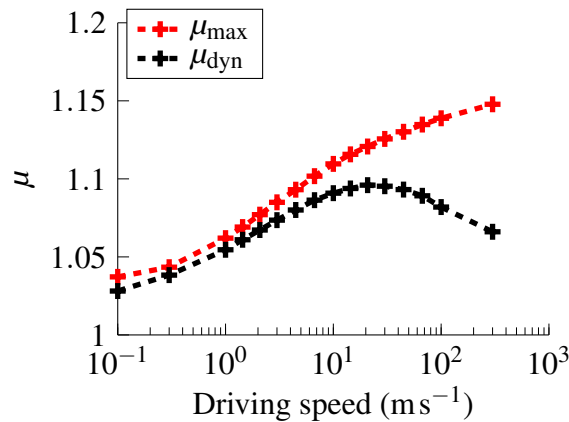


Figure 4.10: Evolution of friction with the driving speed, for the default parameters.

surface under consideration behaves like a sum of Hertzian contacts. It was shown in [74] that the friction forces caused by the viscoelastic losses for such a contact increased with the load with an exponent of $1 + 1/3$, in other words $\mu_{visco} = P_m^{1/3}$. In the present case the exponent is much lower because the contact area is quite large compared to the Hertzian hypotheses.

As the normal load increases, steady state friction goes through a maximum before decreasing. This is because of the saturation of the surface. As the load increases rubber completely fills the wavy surface, so the deformations of rubber during sliding become independent of the normal load. As the viscoelastic losses depend on the deformation, they stop to increase as well and the apparent friction coefficient decreases. This explanation is confirmed by the evolution of mean gap with load which tends to zero at high normal load, shown also in Figure 4.11.

Computations with and without the slope effect show that both the increase of viscoelastic loss and the increase in slope effect play an equally important part in the increase of steady state friction with normal load.

The evolution of maximum friction μ_{max} and in particular the difference between steady-state and maximum friction $\Delta\mu = \mu_{max} - \mu_{dyn}$ is more surprising. This latter parameter is high at low normal loads and decreases steadily. When simulations are run using a surface with only the longer wavelength it does not show the same behaviour, as $\Delta\mu$ remains constant up to 0.4 MPa. Looking closely at the friction curve for the lowest load (Figure 4.12), there is a high but very narrow peak in the friction curve caused by the smaller wavelength, which disappears with the surface only having the longer wavelength.

Loading time also plays a significant role for the maximum friction coefficient μ_{max} . Figure 4.13 shows that for very low loading times, $\mu_{max} = \mu_{dyn}$: the loading time is so low that the contact area increases and mean gap decreases during sliding. As it lengthens, μ_{max} increases until the surface is saturated, that is to say until complete contact occurs during loading. It is another indication showing the strong correlation between the evolution of mean gap and the difference between maximum and steady-state friction.

To ensure the previous results were significant for rough surfaces, a comparison is made between the “wavy” results and the results for a random rough surface having approximately the same characteristics: its higher wavelength and roll-off wavelength are both 500 μm , so that $k_l = k_r = 2\pi/\lambda_1$, its shorter wavelength is λ_2 , so that $k_s = 2\pi/\lambda_2$. The amplitude of the higher wavelength is the same for both surfaces and a Hurst exponent of 0.8 is used, which means the shorter wavelength has a smaller amplitude for the rough surface than for the wavy surface. The friction curves for the rough surface are much smoother because there is no short-length periodicity and the overall friction is lower (Figure 4.14). However, the evolution of maximum and steady-state friction with driving speed and normal load are very similar, including the sharp friction peaks at low load. The steady-state friction evolution with driving speed is slightly shifted towards higher speeds as the shorter wavelength has a smaller amplitude.

The effect of other parameters are also investigated. Using a surface ten times smaller in each direction proves to be almost equivalent to sliding at a ten times higher speed - friction is just a bit higher. The effect of temperature is investigated using a time-

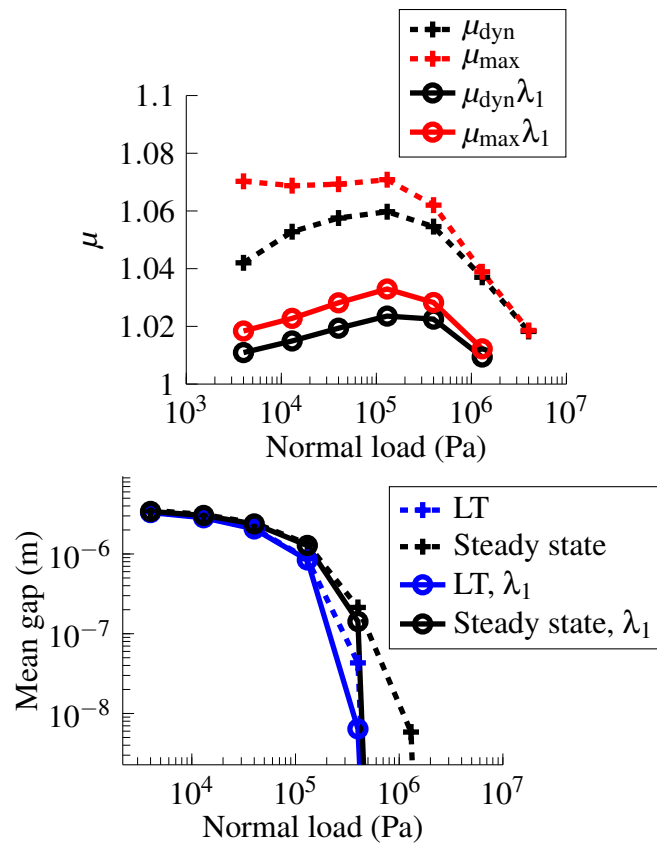


Figure 4.11: Evolution of friction and mean gap with the load, for the default parameters and for a smooth surface with only the larger wavelength.

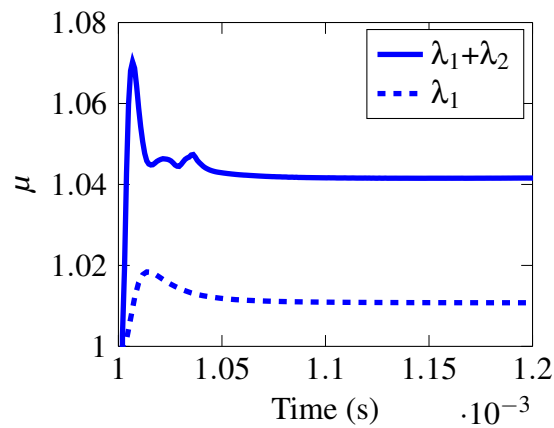


Figure 4.12: Friction curve with a low normal pressure of $P_m = 4 \times 10^{-3}$ MPa, for the default surface ($\lambda_1 + \lambda_2$) and the surface without the smaller wavelength (λ_1).

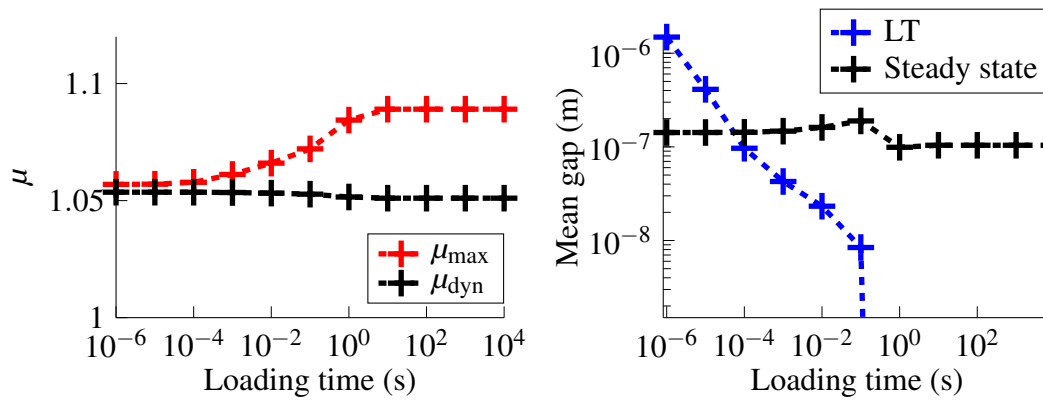


Figure 4.13: Evolution of friction and mean gap with loading time. The steady-state values have a small dependence on the loading time because true steady-state is not reached, but they should be constant.

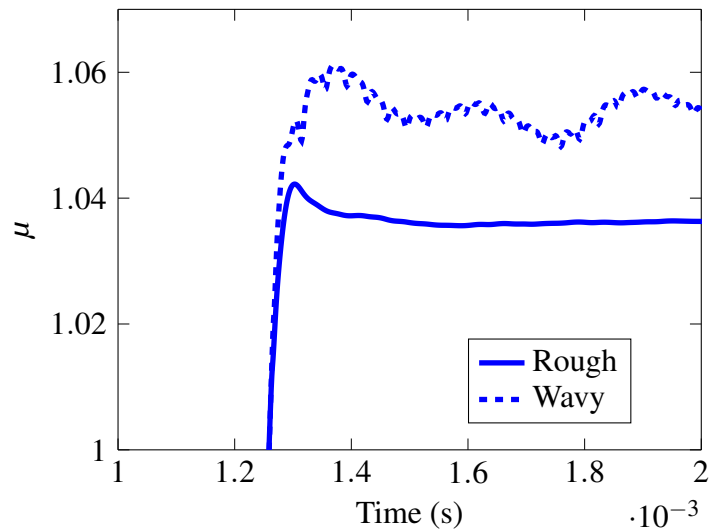


Figure 4.14: Friction curves for a rough and a wavy surface with the default parameters.

temperature equivalence, as described in the famous paper by Williams, Landel and Ferry [77]. The parameters used are those described in [78] for a cross-linked synthetic rubber. According to the time-temperature equivalence, increasing temperature is equivalent to loading during a longer time (which is expected to increase $\Delta\mu$) and to sliding at a lower speed (which is expected to decrease friction and decrease $\Delta\mu$). The results are coherent with the expectations: increasing temperature decreases steady-state friction but keeps $\Delta\mu$ constant. Changing the rubber thickness between 2 and 8 mm did not have any significant impact on friction. During shearing, while the driving speed is applied but the bottom of the block is not sliding yet, the mean gap decreases as rubber continues to relax, so increasing thickness (which increases the shearing time) is expected to increase μ_{max} a bit. But this expected phenomenon is counter-balanced by the fact that the sliding speed at the bottom of the block is also lower. A broader thickness range would have probably impacted the results but the simulations could not be run: a too small thickness induces a coupling between the tangential and normal directions, which is not accounted for in the current model and on the other hand a higher thickness means many more time steps are necessary during shearing, so the computations are longer. Avoiding this problem may have been possible by using longer time steps during the shearing process and ensuring afterwards the local slip remained reasonable between each step, but it was not done.

Overall, all these results tend to validate Persson's approach of viscoelastic contact. All the characteristics of such a contact depend on the different frequencies excited during the loading time or during sliding, the latter being determined with a reasonable precision by the sliding speed multiplied by the wavelength of the surface. The difference of apparent rigidity of rubber between the loading time and sliding is the main reason for the maximum in the friction curve. The study shows that a broad, high maximum in the friction curve can only be caused by large wavelength, large amplitude roughness. In this case, friction at the smaller scales (those which are not discretized in the simulation) can be approximated by a Coulomb friction law and accounting for the local slopes in the contact zone is necessary to avoid underestimating friction. Real life road surfaces, as they are made of aggregates, show very high slopes even at the millimeter scale, which are likely to be in the contact zone should a tire roll on it. These slopes are likely to increase friction in large proportions though these real surfaces cannot be simulated using the present model.

4.5.1 Effect of adhesion on rubber sliding

The effect of adhesion in rough contacts has already been studied analytically by Persson in [79] and numerically by a number of authors [80] [76] [23]. Recently Müser's "*Contact Mechanics Challenge*" [27] had several submissions derived from simulations.

Some authors also worked on viscoelastic, adhesive contacts such as [49] or [81]. There is a strong coupling between adhesion and friction on smooth surfaces, as studied for example in [41]: in the context of continuum mechanics, both phenomena can be modeled as a single crack opening in mode I and II/III respectively. The current model does not take this coupling into account, as normal and tangential directions are decoupled.

Adhesive and friction forces are consequently supposed to be two completely independent phenomena, which surely is a crude approximation for smooth contacts, but might be sufficient for rough contacts at a sufficiently large scale. Even though it may not be true, using the current model still allows to draw some conclusions as to when adhesive forces can be neglected in rough contacts as the coupling makes adhesion less effective when sliding occurs.

Even without a direct coupling, using a Coulomb friction law with adhesive forces is not straightforward, because at the contact edge the pressure is negative so the relation $\|T\| = \mu P$ cannot hold. It is necessary to adapt this friction law by separating pressure into two: the adhesive pressure P_{adh} caused by adhesion defined in Equation 2.21, which is always negative and the remaining pressure P_{surf} which is always positive. It can be interpreted as the pressure that the "hard wall" interaction causes on rubber. Using this pressure for the friction law makes sense, so the friction law turns into $\|T\| = \mu P_{surf}$. The equations governing friction with the slope effect in this case are given in Appendix B.

Two criteria can be used a priori to determine the effect of adhesion on a rough contact. The first is appropriate for low contact ratios and is based on Greenwood and Williamson's approach of a rough contact. We assume rubber lies on the summits of the rough surface which have a certain radius of curvature. Each of these contact patches can be compared to a Hertzian contact with adhesion. According to the JKR theory, adhesion forces can be neglected if the adhesive energy is low enough compared to the normal force - see Equation 4.7 (for lower Tabor numbers, using the DMT theory would yield the same equation with a slightly different prefactor).

$$F_n \gg 3\pi\gamma_0 R_c \quad (4.7)$$

F_n is the normal force, γ_0 the adhesive energy per unit area and R_c the radius of curvature.

The second criterion is based on the elastic energy: if the elastic energy required to deform rubber for a full contact is low compared to the adhesive energy, adhesion will cause a full contact even without any normal load. Inversely, if the adhesive energy is low it will not have a significant impact - see Equation 4.8.

$$E_{elas} \gg \gamma_0 \quad (4.8)$$

E_{elas} is the elastic energy per unit area for a full contact.

These criteria can be easily computed for the wavy model surface used in the current paragraph. Considering there is only one wavelength λ_1 with an amplitude A_1 and the material is incompressible and elastic with a shear modulus G , the radius of curvature of each summit is $R_c = \lambda_1^2 / (6\pi^2 A_1)$, the elastic energy per unit area is $E_{elas} = 3\pi G A_1^2 / (8\lambda_1)$ and the area per summit is $\mathcal{A}_1 = \lambda_1^2 / (2\sqrt{3})$.

Using these expressions and a mean pressure of P_m on the periodic surface yields the criteria given in Equation 4.9: if they are small compared to 1, adhesion may be neglected.

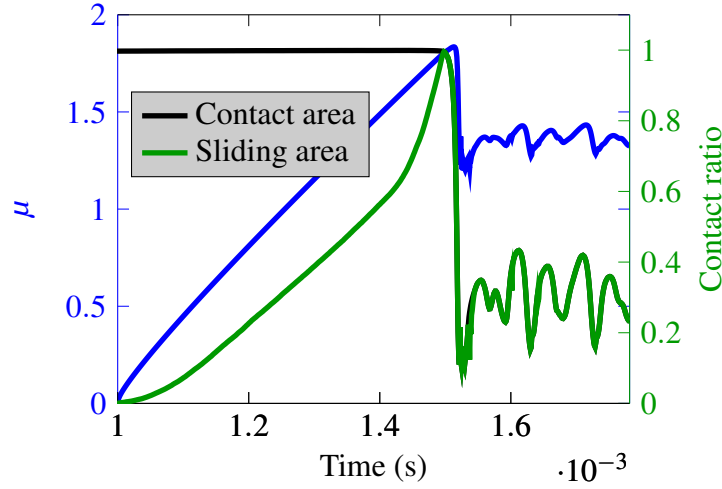


Figure 4.15: Evolution of friction coefficient, contact area and sliding area with time for the default parameters with adhesion.

$$\begin{cases} C_1(\lambda_1, A_1) = \gamma_0 / \left(P_m A_1 \frac{\pi}{\sqrt{3}} \right) \\ C_2(\lambda_1, A_1) = \gamma_0 / \left(A_1^2 \frac{3\pi G}{8\lambda_1} \right) \end{cases} \quad (4.9)$$

The wavy surface under consideration has 2 scales and adhesion should be negligible for both of them in order to be completely neglected. Both these criteria are more constraining for the smaller wavelength as it has a smaller amplitude, so the true criterion indicating if adhesion can be neglected is $C = \min(C_1(\lambda_2, A_2), C_2(\lambda_2, A_2))$.

In the following, simulations are run with an adhesive energy of $\gamma_0 = 20 \text{ mJ m}^{-2}$ and a range of $z_0 = 63.5 \text{ nm}$. The adhesion criterion is calculated using the storage modulus at the frequency of $1/LT$ for the loading time and V/λ_2 for sliding.

The friction curve for the default parameters is given in Figure 4.15. Under these conditions, the criterion is $C_{LT} = 0.9$ for the loading time and $C_V = 0.5$ for sliding. As expected, adhesion has a strong effect: during the loading time, the contact ratio reaches 1 and the extra normal load provided by the adhesive forces increases tremendously both maximum and steady-state friction. Viscoelastic losses are small compared to the effect of adhesion on friction, but viscoelasticity plays nonetheless a significant role as it causes the contact area to shrink during sliding, which reduces the amount of adhesive forces and consequently friction. The variation of contact area is the key factor explaining the maximum in the friction curve. Altogether, this kind of friction curve is in good accordance with what is observed experimentally for a soft, smooth contact, with a sharp transition from ‘static’ to ‘kinetic’ friction (see for example [33]).

In order to decrease the effect of adhesion, the following results are made using a wavy surface with a twice higher amplitude for both length scales ($A_1 = \lambda_1/50$, $A_2 =$

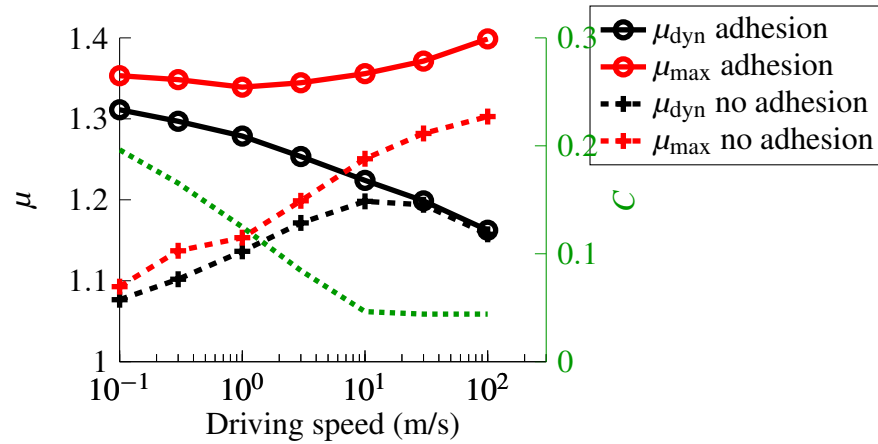


Figure 4.16: Steady state and maximum friction with and without adhesion as a function of the driving velocity for a contact with a high amplitude wavy surface. The dotted green line is the adhesion indicator C .

$\lambda_2/50$). Figure 4.16 shows the evolution of maximum and steady-state friction with the driving speed for such a contact with and without adhesion. It also shows the evolution of the adhesive criterion C_V with speed (the criterion during the loading time is constant, $C_{LT} = 0.22$). As the driving speed increases, adhesion has less and less impact on the steady-state friction. Above 10 m s^{-1} it has almost no impact. Its effect remains the same during the loading time which explains the high values of μ_{max} at all driving speeds.

This paragraph shows that adhesion plays a significant role in the contact of soft material on smooth surfaces. Both the numerical results and the simple adhesion criteria show that surface roughness, apparent material rigidity and high loads can nullify the effect of adhesion on friction, either by reducing the contact surface (which reduces the global adhesive energy) or by making the adhesive forces small compared to the contact forces. These results suggest that for rubber contacts, adhesion is promoted by slow loading and low sliding speeds.

4. Rough contact

Conclusion

The contact between a tire and a road pavement is of crucial importance in modern transportation. The work presented in this thesis aims at simulating this contact from the millimeter scale down to the micrometer scale. Chapter one shows the different aspects of this kind of contact which proves to be difficult to model due to the different physical phenomena that take place. Firstly, the contact problem itself is not trivial. The first analytical solution for the contact of a sphere on an elastic solid was found by Hertz in the late nineteenth century, but a sphere is only a crude approximation of the multi-scale nature of road pavements. Secondly, rubber materials are viscoelastic, which is the main reason why they provide sufficient grip, so this aspect cannot be overlooked. Thirdly, the physical phenomena at the nanometer scale such as van der Waals interactions result, at the micrometer scale, in attractive forces and in friction.

To build an efficient model, the assumption that the rubber tread is very large compared to the roughness size is made. Rubber can consequently be considered as a half-space. After discretizing the surface of this half-space, using Boussinesq's equation allows to compute the normal displacement of this surface as a function of the normal pressure field. This method known as Boundary Element Method. Fast Fourier Transforms allow a fast computation of the displacement. The contact problem is solved using a modified Conjugate gradient iterative procedure, which proves to be robust and fast. Transient viscoelasticity is accounted for with an efficient step-by-step method. The contact solver is adapted to handle adhesive forces and prevents convergence problems. The algorithm with adhesion is robust but considerably slower than without it.

Rubber can be considered as an incompressible material. Along with the half-space hypothesis, it makes the tangential and normal displacements totally decoupled. In spite of this useful property, solving the tangential contact problem remains difficult. The tangential displacements can be computed from the tangential stress with a Fast Fourier Transform in a similar manner as in the normal direction. The friction laws are highly non-linear: at each point either the norm of the tangential stress is small and the point is stuck to the surface, either the point is sliding and in this case the norm of the tangential stress is deduced from the friction law and the normal pressure. Using a Coulomb friction law, taking the local slope into account is necessary to get precise results. A non-linear conjugate gradient procedure able to solve this problem is described. Convergence is steady and as fast as similar algorithms described in the literature.

The last chapter of this thesis shows results for a rough contact. The current model was used to answer to Müser's *Contact Mechanics Challenge*, which involved computing

a rough elastic contact with short-range adhesive forces on a very fine grid. The results were in perfect agreement with the reference solution. The current model is also compared to Persson's theory of rough viscoelastic contact without friction. Both models give very similar results in terms of friction force and contact area. When a viscoelastic solid is sliding in steady state on a rough surface, increasing abruptly the driving speed causes the friction force to increase as well: it goes through a maximum before reaching a new steady state value. When a normal load is first imposed with no sliding and then a driving speed is prescribed at the top of a rubber block, a similar friction curve is obtained. Simulations are run with friction and adhesion under these conditions for a model, 2-scales wavy surface. Results show that large scale roughness is responsible for the maximum in the friction curve. In steady-state sliding, the wavy pattern causes viscoelastic losses that depend on the damping factor $\tan(\delta)$ of the excited frequency. These losses add to the friction losses to increase the global friction force. Adhesion plays a significant role in soft, smooth contact. For high roughness or high sliding speed (which reduces the contact area) its effect is negligible.

On the overall, the present model is a great tool to understand the relative impact of the different phenomena likely to take place in rubber friction. It is, to the knowledge of the author, the first numerical model able to solve a transient contact problem with 2 or 3 length scales of surface roughness and a viscoelastic material, with adhesion and friction at the interface. A quantitative comparison to experimental data still remains out of its reach because of the added complexity of real life contacts. Among the phenomena that are not accounted for in the current model, at least three are known play a significant role. The first is that rubber undergoes large strain. The second is that it heats up during sliding and the temperature is not uniform, so its characteristics are not uniform either. Thirdly the small scale interactions are modeled simply with a friction coefficient, an adhesive energy and a range of interaction, but these parameters are hard to measure experimentally and may not be representative of the reality.

Appendix A

Influence Coefficient matrices in the Fourier space

The goal of this appendix is to find the equations governing the displacements of the surface of a half-space in the Fourier domain. In the following, u, v, w are the displacements in the real space in the x, y and z directions respectively. U, V, W are their Fourier Transforms relatively to the (x, y) plane. ω_x, ω_y are the variables of the Fourier space, $\omega = \sqrt{\omega_x^2 + \omega_y^2}$ is their norm. λ, μ denote the Lamé coefficients (in Equation A.1 they are expressed as a function of the Young modulus and Poisson coefficient).

$$\lambda = \frac{E\nu}{(1+\nu)(1-2\nu)} \tag{A.1}$$
$$\mu = \frac{E}{2(1+\nu)}$$

The Fourier Transforms of components of the stress tensor are $(\tilde{\sigma}_{xx}, \tilde{\sigma}_{yy}, \tilde{\sigma}_{zz}, \tilde{\sigma}_{xy}, \tilde{\sigma}_{xz}, \tilde{\sigma}_{yz})$. Equation A.2 shows how they are related to the displacements. i is the imaginary number.

$$\begin{aligned}
 \tilde{\sigma}_{xx} &= \lambda \left(i\omega_x U + i\omega_y V + \frac{\partial W}{\partial z} \right) + 2\mu i\omega_x U \\
 \tilde{\sigma}_{yy} &= \lambda \left(i\omega_x U + i\omega_y V + \frac{\partial W}{\partial z} \right) + 2\mu i\omega_y V \\
 \tilde{\sigma}_{zz} &= \lambda \left(i\omega_x U + i\omega_y V + \frac{\partial W}{\partial z} \right) + 2\mu \frac{\partial W}{\partial z} \\
 \tilde{\sigma}_{xy} &= \mu(i\omega_y U + i\omega_x V) \\
 \tilde{\sigma}_{xz} &= \mu \left(\frac{\partial U}{\partial z} + i\omega_x W \right) \\
 \tilde{\sigma}_{yz} &= \mu \left(\frac{\partial V}{\partial z} + i\omega_y W \right)
 \end{aligned} \tag{A.2}$$

The equilibrium equations are described in Equation A.3:

$$\begin{aligned}
 \frac{\partial^2(i\omega_x U)}{\partial z^2} - \omega^2(i\omega_x U) - \frac{\mu + \lambda}{\mu} \omega_x^2 \left(i\omega_x U + i\omega_y V + \frac{\partial W}{\partial z} \right) &= 0 \\
 \frac{\partial^2(i\omega_y V)}{\partial z^2} - \omega^2(i\omega_y V) - \frac{\mu + \lambda}{\mu} \omega_y^2 \left(i\omega_x U + i\omega_y V + \frac{\partial W}{\partial z} \right) &= 0 \\
 \frac{\lambda + 2\mu}{\mu + \lambda} \frac{\partial^2 W}{\partial z^2} - \frac{\mu}{\lambda + \mu} \omega^2 W + \frac{\partial}{\partial z} (i\omega_x U + i\omega_y V) &= 0
 \end{aligned} \tag{A.3}$$

Simplifying this equation leads to fourth order differential equations on the displacements given in Equation A.4:

$$\begin{aligned}
 \frac{\partial^4 U}{\omega^4 \partial z^4} - 2 \frac{\partial^2 U}{\omega^2 \partial z^2} + U &= 0 \\
 \frac{\partial^4 V}{\omega^4 \partial z^4} - 2 \frac{\partial^2 V}{\omega^2 \partial z^2} + V &= 0 \\
 \frac{\partial^4 W}{\omega^4 \partial z^4} - 2 \frac{\partial^2 W}{\omega^2 \partial z^2} + W &= 0
 \end{aligned} \tag{A.4}$$

Solutions to these equations have the following form:

$$\begin{aligned}
 U &= (A_U(\omega) + zB_U(\omega)) e^{\omega z} + (C_U(\omega) + zD_U(\omega)) e^{-\omega z} \\
 V &= (A_V(\omega) + zB_V(\omega)) e^{\omega z} + (C_V(\omega) + zD_V(\omega)) e^{-\omega z} \\
 W &= (A_W(\omega) + zB_W(\omega)) e^{\omega z} + (C_W(\omega) + zD_W(\omega)) e^{-\omega z}
 \end{aligned} \tag{A.5}$$

A, B, C, D are functions of ω which have to be deduced using the boundary conditions. In the present case, we will make the hypothesis of semi-infinite, incompressible half-space and solve for a given stress $\tilde{\sigma}^0$ in $z = 0$. We are only interested in the displacements in $z = 0$, which are the displacements of the surface of the half-space, so knowing D is not necessary.

Because of the semi-infinite hypothesis, $A = B = 0$. The other functions are given in Equation A.6.

$$\begin{aligned}
\omega C_U &= -2 \frac{\tilde{\sigma}_{xz}^0}{2\mu} + \frac{\omega_x}{\omega} \left(\frac{\tilde{\sigma}_{xz}^0}{2\mu} \frac{\omega_x}{\omega} + \frac{\tilde{\sigma}_{yz}^0}{2\mu} \frac{\omega_y}{\omega} \right) \\
D_U &= -i \frac{\omega_x}{\omega} D_W \\
\omega C_V &= -2 \frac{\tilde{\sigma}_{yz}^0}{2\mu} + \frac{\omega_y}{\omega} \left(\frac{\tilde{\sigma}_{xz}^0}{2\mu} \frac{\omega_x}{\omega} + \frac{\tilde{\sigma}_{yz}^0}{2\mu} \frac{\omega_y}{\omega} \right) \\
D_V &= -i \frac{\omega_y}{\omega} D_W \\
\omega C_W &= -\frac{\tilde{\sigma}_{zz}^0}{2\mu} \\
D_W &= -\frac{\tilde{\sigma}_{zz}^0}{2\mu} + i \frac{\tilde{\sigma}_{xz}^0}{2\mu} \frac{\omega_x}{\omega} + i \frac{\tilde{\sigma}_{yz}^0}{2\mu} \frac{\omega_y}{\omega}
\end{aligned} \tag{A.6}$$

It should be highlighted that the incompressible hypothesis simplifies these equations and make the tangential and normal directions independent. These equations allow the direct calculation of the Influence coefficient matrices in Fourier space.

Appendix B

Conjugate Gradient modifications to account for the effect of the local slope.

Slope effect with Coulomb friction law

Local normal and tangential forces

Using the notation of Equation 3.3, the local normal and tangential forces can be written as:

$$F_n = (T_x N_x + T_y N_y + P N_z) \begin{pmatrix} N_x \\ N_y \\ N_z \end{pmatrix}$$
$$F_t = \begin{pmatrix} T_x - (T_x N_x^2 + T_y N_y N_x + P N_z N_x) \\ T_y - (T_y N_y^2 + T_x N_x N_y + P N_z N_y) \\ +P - (T_x N_x N_z + T_y N_y N_z + P N_z^2) \end{pmatrix}$$

Elliptic traction bound

Equation 3.4 represents an ellipse in most cases. A rotation of axes using Equation B.1 yields Equation B.2.

$$T_x = \frac{N_x}{\sqrt{1-N_z^2}} X - \frac{N_y}{\sqrt{1-N_z^2}} Y$$
$$T_y = \frac{N_y}{\sqrt{1-N_z^2}} X + \frac{N_x}{\sqrt{1-N_z^2}} Y \quad (\text{B.1})$$

$$a_1 X^2 + c_1 Y^2 + 2d_1 X + 2g_1 Y + f = 0$$

where

$$a_1 = N_z^2(1 + \mu^2) - \mu^2 \quad (\text{B.2})$$

$$c_1 = 1$$

$$d_1 = -P N_z(1 + \mu^2) \sqrt{1 - N_z^2}$$

$$f = P(1 - N_z^2(1 + \mu^2))$$

In these local axes, using the translation $X = X' - \frac{d_1}{a_1}, Y = Y'$ yields Equation B.3

$$\begin{aligned}
 a_1 X'^2 + c_1 Y'^2 + f_1 &= 0 \\
 \text{where} \\
 f_1 &= \frac{P^2 \mu^2}{\mu^2 - (1 + \mu^2) N_z^2}
 \end{aligned} \tag{B.3}$$

Details of Equation 3.12

The variables $K_{\alpha,1}$ and $K_{\alpha,2}$ are equal to zero in the stick zone. In the slip zone they are equal to:

$$\begin{aligned}
 K_{\alpha,1} &= -\frac{C_{12}}{C_0} \left(T_n - P_n * \frac{N}{N_z} \right) \\
 K_{\alpha,2} &= \left(-2 \frac{C_{12}}{C_0} * d_i + \left(2 \frac{C_{12} * C_1}{C_0^2} - 2 \frac{C_{02} * C_{12}^2}{C_0^3} - 2 \frac{C_{22}}{C_0} \right) * \left(T - P * \frac{N}{N_z} \right) \right)
 \end{aligned} \tag{B.4}$$

N is the vector $N = \begin{pmatrix} N_x \\ N_y \end{pmatrix}$.

This equation is the result of a first order expansion of $r_{i+1}^T \cdot \frac{\partial T}{\partial \alpha} = 0$. Substituting Equation 3.10 into Equation 3.4, using $T_{i+1} = T_i + \alpha d_i$, yields Equation B.5

$$C_0 k + C_1 \alpha k + C_{02} k^2 + C_{12} \alpha + C_{22} \alpha^2 = 0 \tag{B.5}$$

Differentiating against α yields :

$$\begin{aligned}
 k &\approx -\alpha \frac{C_{12}}{C_0} \\
 \frac{\partial k}{\partial \alpha} &\approx -\frac{C_{12}}{C_0} + \alpha \left(2 \frac{C_{12} * C_1}{C_0^2} - 2 \frac{C_{02} * C_{12}^2}{C_0^3} - 2 \frac{C_{22}}{C_0} \right)
 \end{aligned}$$

Then

$$\begin{aligned}
 \frac{\partial T}{\partial \alpha} &= d_i - \frac{C_{12}}{C_0} \left(T_i - P_i * \frac{N}{N_z} \right) \\
 &+ \alpha \left(-2 \frac{C_{12}}{C_0} * d_i + \left(2 \frac{C_{12} * C_1}{C_0^2} - 2 \frac{C_{02} * C_{12}^2}{C_0^3} - 2 \frac{C_{22}}{C_0} \right) * \left(T - P * \frac{N}{N_z} \right) \right)
 \end{aligned}$$

and

$$r_{i+1} = r_i - \alpha A \left(d - \frac{C_{12}}{C_0} \left(T_i - P_i * \frac{N}{N_z} \right) \right)$$

In all these equations, the C constants are defined at each point in the slip zone as follow, with $M_x = 1 - N_x^2 * (1 + \mu^2)$. They are equal to zero in the adhesive zone.

$$\begin{aligned}
C_0(T) &= 2M_x T_x^2 + 2M_y T_y^2 - 4T_x T_y N_x N_y (1 + \mu^2) - 2PN_z (1 + \mu^2) (T_x N_x + T_y N_y) \\
&\quad - 2\frac{P}{N_z} (N_x M_x T_x + N_y M_y T_y - (1 + \mu^2) N_x N_y (N_y T_x + N_x T_y)) \\
&\quad + 2P^2 (1 + \mu^2) (1 - N_z^2) \\
C_{12}(d, T) &= 2d_x T_x M_x + 2d_y T_y M_y - 2N_x N_y (1 + \mu^2) (d_x T_y + d_y T_x) \\
&\quad - 2PN_z (1 + \mu^2) (d_x N_x + d_y N_y) \\
C_1(d, T) &= 4d_x T_x M_x + 4d_y T_y M_y - 4N_x N_y (1 + \mu^2) (d_x T_y + d_y T_x) \\
&\quad - 2PN_z (1 + \mu^2) (d_x N_x + d_y N_y) \\
&\quad - 2PM_x \frac{N_x}{N_z} d_x \\
&\quad - 2PM_y \frac{N_y}{N_z} d_y \\
&\quad + 2(1 + \mu^2) P \frac{N_x N_y}{N_z} (N_y d_x + N_x d_y) \\
C_{02}(d, T) &= M_x T_x^2 + M_y T_y^2 - 2(1 + \mu^2) N_x N_y T_x T_y \\
&\quad - 2PM_x \frac{N_x}{N_z} T_x \\
&\quad - 2PM_y \frac{N_y}{N_z} T_y \\
&\quad + \frac{P^2}{N_z^2} (N_x^2 M_x + N_y^2 M_y) \\
&\quad + 2(1 + \mu^2) P \frac{N_x N_y}{N_z} \left(N_y T_x + N_x T_y - P \frac{N_x N_y}{N_z} \right) \\
C_{22}(d, T) &= M_x d_x^2 + M_y d_y^2 - 2N_x N_y (1 + \mu^2) d_x d_y
\end{aligned} \tag{B.6}$$

(In the code the constants are $D_0 = C_0$, $D_{12} = C_{12}$, $D_1 = C_1 - 2\frac{C_{12}}{C_0}C_{02}$, $D_2 = 2C_{22} - \frac{C_{12}}{C_0}C_1$.)

Slope effect for a constant shear stress friction law

The equations are slightly changed when a constant shear stress law is used instead of a Coulomb friction law. Equation 3.4 becomes :

$$\begin{aligned}
&T_x^2 (1 - N_x^2) + T_y^2 (1 - N_y^2) \\
&+ P^2 (1 - N_z^2) - 2T_x T_y N_x N_y = \mu^2 \\
&- 2T_x P N_x N_z - 2T_y P N_y N_z
\end{aligned} \tag{B.7}$$

The traction bound is corrected the same way as before (Equation 3.10), leading to the following equation, which is the same as Equation 3.12 but with different constants.

$$0 = \begin{cases} r_i^T \cdot \left[d_i - \frac{D_{12}}{D_0} * \left(T_i - P_i * \frac{N}{N_z} \right) \right] \\ + \alpha r_i^T \cdot \left[-2 \frac{D_{12}}{D_0} * d + \left(\frac{D_1 * D_{12}}{D_0^2} - \frac{D_2}{D_0} \right) * \left(T_i - P_i * \frac{N}{N_z} \right) \right] \\ - \alpha \left[A \left(d_i - \frac{D_{12}}{D_0} * \left(T_i - P_i * \frac{N}{N_z} \right) \right) \right]^T \cdot \left[d_i - \frac{D_{12}}{D_0} * \left(T_i - P_i * \frac{N}{N_z} \right) \right] \end{cases}$$

In the following equation, $M'_x = 1 - N_x^2$, $M'_y = 1 - N_y^2$ and $M'_z = 1 - N_z^2$.

$$D_0(T) = 2M'_x T_x^2 + 2M'_y T_y^2 - 4T_x T_y N_x N_y - 2PN_z (T_x N_x + T_y N_y) - 2 \frac{P}{N_z} (M'_x T_x + M'_y T_y - N_x N_y (N_y T_x + N_x T_y)) + 2P^2 (1 - N_z^2)$$

$$D_{12}(d, T) = 2d_x T_x M'_x + 2d_y T_y M'_y - 2N_x N_y (d_x T_y + d_y T_x) - 2PN_z (d_x N_x + d_y N_y)$$

$$D_1(d, T) = 4d_x T_x M'_x + 4d_y T_y M'_y - 4N_x N_y (d_x T_y + d_y T_x) - 2PN_z (d_x N_x + d_y N_y) - 2 \frac{D_{12}}{D_0} (M'_x T_x^2 + M'_y T_y^2 - 2N_x N_y T_x T_y) - 2PM'_x \frac{N_x}{N_z} (d_x - 2 \frac{D_{12}}{D_0} T_x) - 2PM'_y \frac{N_y}{N_z} (d_y - 2 \frac{D_{12}}{D_0} T_y) - 2 \frac{P^2}{N_z^2} \frac{D_{12}}{D_0} (N_x^2 M'_x + N_y^2 M'_y) + 2P \frac{N_x N_y}{N_z} \left(N_y d_x + N_x d_y - 2 \frac{D_{12}}{D_0} (N_y T_x + N_x T_y + P \frac{N_x N_y}{N_z}) \right)$$

$$D_2(d, T) = 2M'_x d_x^2 + 2M'_y d_y^2 - 4N_x N_y d_x d_y - \frac{D_{12}}{D_0} (4d_x T_x M'_x + 4d_y T_y M'_y - 4N_x N_y (d_x T_y + d_y T_x)) + 2 \frac{D_{12}}{D_0} PN_z (d_x N_x + d_y N_y) + 2P \frac{D_{12}}{D_0 N_z} (N_x M'_x d_x + N_y M'_y d_y - N_x N_y (N_y d_x + N_x d_y))$$

Coulomb friction and adhesion

Adopting a Coulomb friction law when there are adhesive forces between the surface might seem irrational. Indeed, in such a contact, at the edge of the contact spots the pressure is always negative, which makes the Coulomb law $\|F_t\| = \mu\|F_n\|$ inoperative.

But the pressure in case of adhesion is the sum of two terms: the adhesion pressure and the surface reaction $F_n = F_{adh} + F_+$. It seems appropriate to use the surface reaction alone to compute the friction. The Coulomb law then reads $\|F_t\| = \mu\|F_n - \gamma_0/z_0\|$, as the adhesive force when the two surfaces are in contact is γ_0/z_0 . Equation 3.4 then becomes:

$$\begin{aligned}
 & T_x^2(1 - N_x^2(1 + \mu^2)) + T_y^2(1 - N_y^2(1 + \mu^2)) \\
 & + P^2(1 - N_z^2(1 + \mu^2)) - 2T_x T_y N_x N_y (1 + \mu^2) \\
 & - 2T_x P N_x N_z (1 + \mu^2) - 2T_y P N_y N_z (1 + \mu^2) \\
 & - 2\mu^2 \frac{\gamma_0}{z_0} T_x N_x N_z - 2\mu^2 \frac{\gamma_0}{z_0} T_y N_y N_z \\
 & - 2\mu^2 \frac{\gamma_0}{z_0} P N_z^2 - \mu^2 \frac{\gamma_0^2}{z_0^2} N_z^2 = 0
 \end{aligned}$$

The constants C defined in Appendix B should be changed into C' as follows:

$$\begin{aligned}
 C'_0(T) &= C_0 - 2\mu^2 \frac{\gamma_0}{z_0} N_x N_z (T_x - P \frac{N_x}{N_z}) \\
 &\quad - 2\mu^2 \frac{\gamma_0}{z_0} N_y N_z (T_y - P \frac{N_y}{N_z}) \\
 C'_{12}(d, T) &= C_{12} - 2\mu^2 \frac{\gamma_0}{z_0} N_x N_z d_x \\
 &\quad - 2\mu^2 \frac{\gamma_0}{z_0} N_y N_z d_y \\
 C'_1(d, T) &= C_1 - 2\mu^2 \frac{\gamma_0}{z_0} N_x N_z d_x \\
 &\quad - 2\mu^2 \frac{\gamma_0}{z_0} N_y N_z d_y \\
 C'_{02}(d, T) &= C_{02} \\
 C'_{22}(d, T) &= C_{22}
 \end{aligned} \tag{B.8}$$

If the friction law is a ‘‘Constant shear’’ traction law, no modification is necessary.

B. Conjugate Gradient modifications to account for the effect of the local slope.

Bibliography

- [1] J. A. Greenwood and J. B. P. Williamson. Contact of Nominally Flat Surfaces. *Proceedings of the Royal Society of London A: Mathematical, Physical and Engineering Sciences*, 295(1442):300–319, December 1966.
- [2] A. W. Bush, R. D. Gibson, and T. R. Thomas. The elastic contact of a rough surface. *Wear*, 35(1):87–111, November 1975.
- [3] B. N. J. Persson. Theory of rubber friction and contact mechanics. *The Journal of Chemical Physics*, 115(8):3840–3861, August 2001.
- [4] B. N. J. Persson. Contact mechanics for randomly rough surfaces. *Surface Science Reports*, 61(4):201–227, June 2006.
- [5] Angela A. Pitenis, Duncan Dowson, and W. Gregory Sawyer. Leonardo da Vinci’s Friction Experiments: An Old Story Acknowledged and Repeated. *Tribology Letters*, 56(3):509–515, October 2014.
- [6] Charles Augustin Coulomb. *Théorie des machines simples (Nouv. éd.) / , en ayant égard au frottement de leurs parties et à la roideur des cordages, par C.-A. Coulomb,... Nouvelle édition...* Bachelier (Paris), 1821.
- [7] Vladislav A. Yastrebov. Sliding Without Slipping Under Coulomb Friction: Opening Waves and Inversion of Frictional Force. *Tribology Letters*, 62(1):1, April 2016.
- [8] Danh Toan Nguyen, Pierdomenico Paolino, M. C. Audry, Antoine Chateauminois, Christian Fretigny, Yohan Le Chenadec, M. Portigliatti, and E. Barthel. Surface Pressure and Shear Stress Fields within a Frictional Contact on Rubber. *The Journal of Adhesion*, 87(3):235–250, March 2011.
- [9] J. J. Kalker. *Three-Dimensional Elastic Bodies in Rolling Contact*. Number v. 2 in Solid mechanics and its applications. Kluwer Academic Publishers, Dordrecht ; Boston, 1990.
- [10] H. M. Stanley and T. Kato. An FFT-Based Method for Rough Surface Contact. *Journal of Tribology*, 119(3):481–485, July 1997.

- [11] Shuangbiao Liu, Qian Wang, and Geng Liu. A versatile method of discrete convolution and FFT (DC-FFT) for contact analyses. *Wear*, 243(1–2):101–111, August 2000.
- [12] I. A. Polonsky and L. M. Keer. A numerical method for solving rough contact problems based on the multi-level multi-summation and conjugate gradient techniques. *Wear*, 231(2):206–219, July 1999.
- [13] Koffi Espoir Koumi, Thibaut Chaise, and Daniel Nelias. Rolling contact of a rigid sphere/sliding of a spherical indenter upon a viscoelastic half-space containing an ellipsoidal inhomogeneity. *Journal of the Mechanics and Physics of Solids*, 80:1–25, July 2015.
- [14] I. F. Kozhevnikov, J. Cesbron, D. Duhamel, H. P. Yin, and F. Anfosso-Lédée. A new algorithm for computing the indentation of a rigid body of arbitrary shape on a viscoelastic half-space. *International Journal of Mechanical Sciences*, 50(7):1194–1202, July 2008.
- [15] H. P. Yin, J. Cesbron, and Q. H. Bui. A new formulation for solving 3-D time dependent rolling contact problems of a rigid body on a viscoelastic half-space. *Mechanics Research Communications*, 64:8–14, March 2015.
- [16] X. H. Chen and D. W. Wang. Fractal and spectral analysis of aggregate surface profile in polishing process. *Wear*, 271(11–12):2746–2750, September 2011.
- [17] C. G. Panagiotopoulos, V. Mantic, and T. Roubicek. A simple and efficient BEM implementation of quasistatic linear visco-elasticity. *International Journal of Solids and Structures*, 51(13):2261–2271, June 2014. WOS:000336775400002.
- [18] Giuseppe Carbone and Carmine Putignano. A novel methodology to predict sliding and rolling friction of viscoelastic materials: Theory and experiments. *Journal of the Mechanics and Physics of Solids*, 61(8):1822–1834, August 2013.
- [19] Jing Zhao, Edwin A. H. Vollebregt, and Cornelis W. Oosterlee. A fast nonlinear conjugate gradient based method for 3D concentrated frictional contact problems. *Journal of Computational Physics*, 288:86–100, May 2015.
- [20] C. H. Liu, Yih-Hong Lin, and Po-Hsuan Lin. A numerical analysis of partial slip problems under Hertzian contacts. *Meccanica*, 42(2):197–206, April 2007.
- [21] R. Pohrt and Q. Li. Complete boundary element formulation for normal and tangential contact problems. *Physical Mesomechanics*, 17(4):334–340, November 2014.
- [22] F. Kosior, N. Guyot, and G. Maurice. Analysis of frictional contact problem using boundary element method and domain decomposition method. *International Journal for Numerical Methods in Engineering*, 46(1):65–82, September 1999.

-
- [23] Valentine Rey, Guillaume Anciaux, and Jean-François Molinari. Normal adhesive contact on rough surfaces: Efficient algorithm for FFT-based BEM resolution. *Computational Mechanics*, pages 1–13, March 2017.
- [24] P. Sainsot and A. A. Lubrecht. Efficient solution of the dry contact of rough surfaces: A comparison of fast Fourier transform and multigrid methods. *Proceedings of the Institution of Mechanical Engineers, Part J: Journal of Engineering Tribology*, 225(6):441–448, June 2011.
- [25] J. C. Simo and T. J. R. Hughes. *Computational Inelasticity*. Springer Science & Business Media, May 2006.
- [26] J.R.M Radok. Visco-elastic stress analysis. *Quarterly of Applied Mathematics*, 15(2), 1957.
- [27] Martin H. Müser, Wolf B. Dapp, Romain Bugnicourt, Philippe Sainsot, Nicolas Lesaffre, Ton A. Lubrecht, Bo N. J. Persson, Kathryn Harris, Alexander Bennett, Kyle Schulze, Sean Rohde, Peter Ifju, W. Gregory Sawyer, Thomas Angelini, Hossein Ashtari Esfahani, Mahmoud Kadkhodaei, Saleh Akbarzadeh, Jiunn-Jong Wu, Georg Vorlauffer, András Vernes, Soheil Solhjoo, Antonis I. Vakis, Robert L. Jackson, Yang Xu, Jeffrey Streator, Amir Rostami, Daniele Dini, Simon Medina, Giuseppe Carbone, Francesco Bottiglione, Luciano Afferrante, Joseph Monti, Lars Pastewka, Mark O. Robbins, and James A. Greenwood. Meeting the Contact-Mechanics Challenge. *Tribology Letters*, 65(4):118, December 2017.
- [28] B. N. J. Persson and A. I. Volokitin. Theory of rubber friction: Nonstationary sliding. *Physical Review B*, 65(13):134106, March 2002.
- [29] Martin Müser. The Contact Mechanics Challenge, 2015.
- [30] E. H. Lee and J. R. M. Radok. The Contact Problem for Viscoelastic Bodies. *Journal of Applied Mechanics*, 27(3):438–444, September 1960.
- [31] E. Barthel and G. Haiat. Approximate Model for the Adhesive Contact of Viscoelastic Spheres. *Langmuir*, 18(24):9362–9370, November 2002.
- [32] R. D. MINDLIN. Compliance of Elastic Bodies in Contact. *J. Appl. Mech. Trans. ASME*, 16:259–268, 1949.
- [33] Tristan Baumberger and Christiane Caroli. Solid friction from stick–slip down to pinning and aging. *Advances in Physics*, 55(3-4):279–348, May 2006.
- [34] Joseph Boussinesq. Essai théorique sur l'équilibre des massifs pulvérulents, comparé à celui de massifs solides, et sur la poussée des terres sans cohésion ;. *Lilliad - Université de Lille - Sciences et technologies*, 1876.
-

- [35] Joseph Boussinesq. *Application des potentiels à l'étude de l'équilibre et du mouvement des solides élastiques, principalement au calcul des déformations et des pressions que produisent, dans les solides, des efforts quelconques exercés sur une petite partie de leur surface ou de leur intérieur : mémoire suivi de notes étendues sur divers points de physique mathématique et d'analyse*. Gauthier-Villars, 1885.
- [36] K. L. Johnson. *Contact Mechanics*. Cambridge University Press, Cambridge [Cambridgeshire]; New York, 1987.
- [37] K. L. Johnson, K. Kendall, and A. D. Roberts. Surface Energy and the Contact of Elastic Solids. *Proceedings of the Royal Society of London A: Mathematical, Physical and Engineering Sciences*, 324(1558):301–313, September 1971.
- [38] B. V Derjaguin, V. M Muller, and Yu. P Toporov. Effect of contact deformations on the adhesion of particles. *Journal of Colloid and Interface Science*, 53(2):314–326, November 1975.
- [39] D Tabor. Surface forces and surface interactions. *Journal of Colloid and Interface Science*, 58(1):2–13, January 1977.
- [40] Daniel Maugis. Adhesion of spheres: The JKR-DMT transition using a dugdale model. *Journal of Colloid and Interface Science*, 150(1):243–269, April 1992.
- [41] K. L. Johnson. A Continuum Mechanics Model of Adhesion and Friction in a Single Asperity Contact. In Bharat Bhushan, editor, *Micro/Nanotribology and Its Applications*, number 330 in NATO ASI Series, pages 151–168. Springer Netherlands, 1997.
- [42] M. Deruelle, H. Hervet, G. Jandeau, and L. Léger. Some remarks on JKR experiments. *Journal of Adhesion Science and Technology*, 12(2):225–247, January 1998.
- [43] R. Christensen. *Theory of Viscoelasticity: An Introduction*. Elsevier, October 1982.
- [44] E. H. Lee. Stress analysis in visco-elastic bodies. *Quarterly of Applied Mathematics*, 13(2):183–190, 1955.
- [45] T. C. T. Ting. The Contact Stresses Between a Rigid Indenter and a Viscoelastic Half-Space. *Journal of Applied Mechanics*, 33(4):845–854, December 1966.
- [46] R. A. Schapery. A theory of crack initiation and growth in viscoelastic media. *International Journal of Fracture*, 11(1):141–159, February 1975.
- [47] R. A. Schapery. On the mechanics of crack closing and bonding in linear viscoelastic media. *International Journal of Fracture*, 39(1-3):163–189, March 1989.
- [48] E. Barthel and C. Frétiigny. Adhesive contact of elastomers: Effective adhesion energy and creep function. *Journal of Physics D: Applied Physics*, 42(19):195302, 2009.

-
- [49] G. Haiat, M. C. Phan Huy, and E. Barthel. The adhesive contact of viscoelastic spheres. *Journal of the Mechanics and Physics of Solids*, 51(1):69–99, January 2003.
- [50] Taylor Hobson. Taylor Hobson - History, 2017.
- [51] Tevis D. B. Jacobs, Till Junge, and Lars Pastewka. Quantitative characterization of surface topography using spectral analysis. *Surface Topography: Metrology and Properties*, 5(1):013001, 2017.
- [52] Erkin Sidick. Power spectral density specification and analysis of large optical surfaces. volume 7390, pages 73900L–73900L–12, 2009.
- [53] Vladislav A. Yastrebov, Guillaume Anciaux, and Jean-François Molinari. From infinitesimal to full contact between rough surfaces: Evolution of the contact area. *International Journal of Solids and Structures*, 52:83–102, January 2015.
- [54] P. Ranganath Nayak. Random Process Model of Rough Surfaces. *Journal of Lubrication Technology*, 93(3):398–407, July 1971.
- [55] J. A. Greenwood. A simplified elliptic model of rough surface contact. *Wear*, 261(2):191–200, July 2006.
- [56] G. Carbone and F. Bottiglione. Asperity contact theories: Do they predict linearity between contact area and load? *Journal of the Mechanics and Physics of Solids*, 56(8):2555–2572, August 2008.
- [57] Guillaume Haiat and Etienne Barthel. An Approximate Model for the Adhesive Contact of Rough Viscoelastic Surfaces. *Langmuir*, 23(23):11643–11650, November 2007.
- [58] M. Scaraggi and B. N. J. Persson. Friction and universal contact area law for randomly rough viscoelastic contacts. *Journal of Physics: Condensed Matter*, 27(10):105102, March 2015.
- [59] B. Lorenz, Y. R. Oh, S. K. Nam, S. H. Jeon, and B. N. J. Persson. Rubber friction on road surfaces: Experiment and theory for low sliding speeds. *The Journal of Chemical Physics*, 142(19):194701, May 2015.
- [60] B. N. J. Persson. Rubber friction: Role of the flash temperature. *Journal of Physics: Condensed Matter*, 18(32):7789, August 2006.
- [61] C. H. Venner and A. A. Lubrecht. *Multilevel Methods in Lubrication*. Number 37 in Tribology series. Elsevier, Amsterdam ; New York, 1st ed edition, 2000.
- [62] A. E. H. Love. The Stress Produced in a Semi-Infinite Solid by Pressure on Part of the Boundary. *Philosophical Transactions of the Royal Society of London. Series A, Containing Papers of a Mathematical or Physical Character*, 228:377–420, 1929.
-

- [63] A. Brandt and A. A. Lubrecht. Multilevel Matrix Multiplication and Fast Solution of Integral Equations. *J. Comput. Phys.*, 90(2):348–370, September 1990.
- [64] C. Putignano, L. Afferrante, G. Carbone, and G. Demelio. A new efficient numerical method for contact mechanics of rough surfaces. *International Journal of Solids and Structures*, 49(2):338–343, January 2012.
- [65] Julian Allwood. Survey and Performance Assessment of Solution Methods for Elastic Rough Contact Problems. *Journal of Tribology*, 127(1):10–23, February 2005.
- [66] Carlos Campañá and Martin H. Müser. Practical Green’s function approach to the simulation of elastic semi-infinite solids. *Physical Review B*, 74(7):075420, August 2006.
- [67] Martin H. Müser. Single-asperity contact mechanics with positive and negative work of adhesion: Influence of finite-range interactions and a continuum description for the squeeze-out of wetting fluids. *Beilstein Journal of Nanotechnology*, 5(1):419–437, April 2014.
- [68] Severino P. C. Marques and Guillermo J. Creus. *Computational Viscoelasticity*. SpringerBriefs in Applied Sciences and Technology. Springer Berlin Heidelberg, Berlin, Heidelberg, 2012.
- [69] Eric W. Weisstein. Gauss’s Circle Problem.
- [70] Romain Bugnicourt, Philippe Sainsot, Catherine Gauthier, and A. A. Lubrecht. FFT-based methods for solving a rough adhesive contact: Description and convergence study. *Tribology Letters*, To be published.
- [71] J. A. Greenwood and K. L. Johnson. An alternative to the Maugis model of adhesion between elastic spheres. *Journal of Physics D: Applied Physics*, 31(22):3279, 1998.
- [72] William W. Hager and Hongchao Zhang. Algorithm 851: CG_DESCENT, a Conjugate Gradient Method with Guaranteed Descent. *ACM Trans. Math. Softw.*, 32(1):113–137, March 2006.
- [73] Hao Liu, Haijun Wang, and Qin Ni. On Hager and Zhang’s conjugate gradient method with guaranteed descent. *Applied Mathematics and Computation*, 236:400–407, June 2014.
- [74] B. N. J. Persson. Rolling friction for hard cylinder and sphere on viscoelastic solid. *The European Physical Journal E*, 33(4):327–333, November 2010.
- [75] Y. Z. Hu and K. Tonder. Simulation of 3-D random rough surface by 2-D digital filter and fourier analysis. *International Journal of Machine Tools and Manufacture*, 32(1–2):83–90, February 1992.

- [76] A. Almqvist, C. Campañá, N. Prodanov, and B. N. J. Persson. Interfacial separation between elastic solids with randomly rough surfaces: Comparison between theory and numerical techniques. *Journal of the Mechanics and Physics of Solids*, 59(11):2355–2369, November 2011.
- [77] Malcolm L. Williams, Landel, Robert F, Ferry, and John D. The temperature dependence of relaxation mechanisms in amorphous polymers and other glass-forming liquids. *American Chemical Society. Journal*, 77:3701–3707, July 1955.
- [78] Ralph G. Mancke and John D. Ferry. Dynamic Mechanical Properties of Cross-Linked Rubbers. IV. Dicumyl Peroxide Vulcanizates of Styrene-Butadiene Rubber. *Transactions of the Society of Rheology*, 12(2):335–350, July 1968.
- [79] B. N. J. Persson. Adhesion between an elastic body and a randomly rough hard surface. *The European Physical Journal E*, 8(4):385–401, 2002.
- [80] G. Carbone, M. Scaraggi, and U. Tartaglino. Adhesive contact of rough surfaces: Comparison between numerical calculations and analytical theories. *The European Physical Journal E*, 30(1):65–74, September 2009.
- [81] J. A. Greenwood and K. L. Johnson. Oscillatory loading of a viscoelastic adhesive contact. *Journal of Colloid and Interface Science*, 296(1):284–291, April 2006.

FOLIO ADMINISTRATIF

THÈSE SOUTENUE DEVANT L'INSTITUT NATIONAL DES SCIENCES APPLIQUÉES DE LYON

NOM: BUGNICOURT
2017

DATE de SOUTENANCE : 28 novembre

Prénom: Romain

TITRE: Simulation of the contact between a rough surface and a viscoelastic material with friction.

NATURE: Doctorat

Numéro d'ordre: 2017-ISAL-117

École doctorale: MEGA

Spécialité: Mécanique

RÉSUMÉ:

Les pneus sont un organe déterminant dans la tenue de route des véhicules. Cette thèse porte sur la modélisation du contact entre la bande de roulement d'un pneumatique et une route sèche, afin de comprendre les différents phénomènes physiques mis en jeu ainsi que leurs rôles relatifs dans le frottement.

La rugosité multi échelle des sols routiers les rendent difficiles à modéliser avec une simulation par éléments finis standard. En utilisant l'hypothèse que la gomme de la bande de roulement est très grande devant la taille des rugosités, elle peut être considérée comme un massif semi-infini. Il est alors possible de résoudre efficacement le problème de contact en ne discrétisant que la surface du massif de gomme. Cette résolution est faite à l'aide d'un algorithme de Gradient Conjugué, au cours duquel les calculs matriciels sont effectués par Transformée de Fourier Rapide (FFT). La viscoélasticité de la gomme est prise en compte en régime transitoire. Les interactions à l'interface entre la gomme et le sol sont modélisés par une loi de frottement ainsi que par une énergie d'adhésion.

Les résultats montrent le rôle primordial de la viscoélasticité qui, couplée à la rugosité multi-échelle du sol, modifie la surface du contact au cours des différents étapes de mise en glissement d'un pneumatique, faisant ainsi varier le frottement.

MOTS-CLÉS : Contact, Viscoélasticité, Elements de Frontière, Frottement, Adhésion

Laboratoire(s) de recherche: Laboratoire de Mécanique des Contacts et des Structures
UMR CNRS 5259 - INSA de Lyon
Bâtiment Sophie Germain
Avenue Jean Capelle
69621 Villeurbanne Cedex FRANCE

Directeur de thèse: Monsieur le Professeur Antonius LUBRECHT

Président du jury: le président

Composition du jury: Chateauminois, Antoine
Lubrecht, Ton
Molinari, Jean-François
Gauthier, Catherine
Sainsot, Philippe
Müser, Martin